Contour-crossing calculations quantify decadal changes in the pCO_2 impacts of inorganic chemical weathering in the North American Arctic

Preston Cosslett Kemeny[a*]

[a] Department of Marine Chemistry and Geochemistry, Woods Hole Oceanographic Institution, Woods Hole, MA, USA

[*]**Corresponding author**: Preston Cosslett Kemeny
Woods Hole Oceanographic Institution, 266 Woods Hole Road, Woods Hole, MA 02543
(preston.kemeny@whoi.edu, preston.kemeny@gmail.com)
ORCID: https://orcid.org/0000-0003-1693-4142

This manuscript is a preprint submitted to EarthArXiv. The paper has also been submitted to *Global Biogeochemical Cycles*, where is has undergone one round of peer review but not yet been accepted for publication. Subsequent versions of this manuscript may have slightly different content. Please contact Preston Cosslett Kemeny with any questions or comments on this work.

Keywords

- Permafrost, weathering, sulfide oxidation, river, carbon cycle, geochemistry

Key points

- Thaw-driven sulfide oxidation is increasing SO_4^{2-}/Σ^+ ratios and decreasing $\Delta(ALK)/\Delta(FIC)$ ratios in Arctic rivers draining permafrost
- Decadal carbonate and silicate weathering increases have partially (Yukon) or fully (Mackenzie) offset pCO_2 changes from sulfide oxidation
- It will be increasingly difficult for weathering to compensate for further declines in the $\Delta(ALK)/\Delta(FIC)$ ratio

Abstract: Degradation of Arctic permafrost is altering biogeochemical dynamics by exposing previously frozen sediment to water, acids, and oxidants. While thaw-driven enhancement of carbonate and silicate mineral weathering results in drawdown of atmospheric carbon dioxide (pCO_2), acting as a negative feedback on modern climate change, enhancement of sulfide mineral oxidation increases pCO_2 and acts as a positive feedback. The net balance of these chemical weathering reactions sets the sign of the permafrost mineral weathering feedback and partially underlies predictions for the impacts of Arctic landscape change on pCO_2 over decadal timescales. This work inverts historical river observations using the MEANDIR model (v1.4) and interprets those results with a new polar conceptual framework to demonstrate that increases in carbonate weathering and silicate weathering since 1980 have fully compensated for increases in sulfide oxidation within the Mackenzie River catchment (sampled upstream of its confluence with the Arctic Red River). Despite declines in the ratio of weathering-derived alkalinity to weathering-derived carbon, permafrost degradation has not yet significantly modified the impact of inorganic chemical weathering on pCO_2 within this major Arctic catchment. Within smaller and steeper sedimentary systems, such as the Peel River, enhanced sulfide oxidation has reduced CO_2 drawdown. Likewise, increases in carbonate weathering and silicate weathering within the Yukon River have not been sufficient to compensate for increases in sulfide mineral oxidation through time. The relative importance of thaw-driven mineral exposure, couplings among weathering reactions, and changes in the length of flow paths collectively determine how each weathering system responds to decadal permafrost thaw; such processes are expected to vary across geomorphic setting and ecosystem structure. Non-linearity in the magnitude of chemical weathering required to compensate for changes in the ratio of weathering-derived alkalinity to weathering-derived carbon suggests that it will be increasingly difficult to avoid further reductions in CO_2 drawdown over the coming decades.

Plain language summary: Thawing of high-latitude permafrost is modifying the delivery of acids and oxidants to subsurface chemical weathering reactors. While enhanced weathering of some minerals removes atmospheric carbon dioxide, mitigating the effects of modern climate change, oxidation of other minerals increases atmospheric carbon dioxide and fuels further landscape degradation. This work employs historical data to quantify mineral weathering within Arctic catchments. Despite changes in dissolved chemistry, the impact of mineral weathering on atmospheric carbon dioxide within the Mackenzie River catchment has been invariant over the last 40 years. In contrast, reductions in the drawdown of atmospheric carbon dioxide have occurred within the Yukon River catchment and Peel River catchment. Inorganic mineral weathering in the Mackenzie River and Yukon River remains a net sink of carbon dioxide but is trending towards becoming a net source.

1. Introduction

Thawing of Arctic permafrost due to anthropogenic climate change is destabilizing landscapes and modifying biogeochemical fluxes through the exposure and reaction of organic and inorganic sediment (Hinzman et al., 2005; Kokelj et al., 2013; Biskaborn et al., 2019; Tank et al., 2023). Across the Arctic's distinct geomorphic and climatic settings, such exposure can occur through decadal deepening in the depth of seasonal thaw, thermokarst activity, or wholesale reduction in permafrost extent (Hinkel and Nelson, 2003; Frey and McClelland, 2009). While much prior research has focused on the response of the organic carbon cycle to permafrost thaw (Koven et al., 2011; Schuur et al., 2015; Myers-Smith et al., 2020; Miner et al., 2022; Vonk et al., 2025), substantially less is known regarding the impacts of high-latitude landscape change on inorganic mineral weathering reactions (Beaulieu et al., 2011, 2012; Zolkos et al., 2018; Walsh et al., 2024). Addressing this knowledge gap is important because mineral dissolution reactions can act as either positive or negative feedbacks on modern climate change and the relative importance of chemical weathering reactions is shifting with ongoing modifications to the thermal and hydrologic regimes of permafrost landscapes (Walvoord and Striegl, 2007; Walvoord and Kurylyk, 2016; Lafrenière and Lamoureux, 2019).

The impact of chemical weathering on the partial pressure of atmospheric carbon dioxide (pCO_2) is ultimately modulated by the production and consumption of alkalinity (ALK) and the movement of carbon atoms from and between the geosphere, hydrosphere, and atmosphere. Whereas weathering of silicate and carbonate minerals acts to reduce pCO_2, the oxidation of sulfide minerals generally acts to increase pCO_2 (Spence and Telmer, 2005; Torres et al., 2014). Currently, a lack of understanding regarding how these distinct weathering reactions may change in response to permafrost thaw reflects a major uncertainty in predicting the impacts of Arctic

landscape change on pCO_2 over the coming decades. If enhancements in silicate and carbonate weathering due to modern thaw exceed the enhancement in sulfide oxidation, the inorganic weathering response would be a negative feedback on rising pCO_2 values (Beaulieu et al., 2012). Conversely, if thaw enhances sulfide oxidation relative to other forms of chemical weathering, the change in Arctic inorganic chemical weathering dynamics would be a positive feedback on global climate change (Zolkos et al., 2018; Walsh et al., 2024). While weathering fluxes are small relative to anthropogenic emissions, increases in carbonate or silicate weathering fluxes could still offset possible reductions in CO_2 drawdown resulting from sulfide oxidation.

Rivers are valuable tools for quantifying the relative magnitudes of chemical weathering fluxes because, by integrating across scale and process, they average through small-scale landscape heterogeneity to reveal net, catchment-scale carbon dynamics. Indeed, prior studies have observed shifts in the dissolved chemistry of Arctic rivers consistent with changes in the relative importance of chemical weathering reactions over prior decades (Fig. 1; Drake et al., 2018; Tank et al., 2023). Within the Yukon River Basin, Toohey et al. (2016) demonstrated increasing sulfate (SO_4^{2-}) fluxes at Pilot Station and Kemeny et al. (2023) identified increasing sulfide oxidation in the Koyukuk River. In the Mackenzie River, Tank et al. (2016) identified increases in fluvial ALK and SO_4^{2-} fluxes. In turn, Walsh et al. (2024) built on those results and those of Calmels et al. (2007) to attribute increased Mackenzie River SO_4^{2-} fluxes to enhanced sulfide oxidation. Consistent with Kokelj et al. (2013) and Zolkos et al. (2018), Walsh et al. (2024) also identified increasing sulfide oxidation in the Peel River, which is a northern tributary to the Mackenzie River. In addition, several other recent works have identified elevated SO_4^{2-} and metal fluxes in Alaskan streams and rivers, as well as streambed discoloration, attributed to thaw-driven sulfide oxidation and iron mobilization (O'Donnell et al., 2024; Sullivan et al., 2025; Dial et al., 2026; Evinger et

al., 2026; Skierszkan et al., 2026). Inspired by such prior studies, this work seeks to place findings of enhanced Arctic sulfide oxidation within a broader framework evaluating how all the thaw-driven shifts in inorganic weathering reactions collectively modify pCO_2.

Although prior work has provided evidence that permafrost thaw is enhancing sulfide oxidation within the Arctic landscapes of Northwestern North America, changes in sulfide oxidation alone are not sufficient to evaluate the directionality of the permafrost mineral weathering feedback. Rather, relating thaw-driven sulfide oxidation to reductions in the capacity for high-latitude weathering to reduce pCO_2 requires accounting for simultaneous shifts in carbonate mineral weathering and silicate mineral weathering (Kemeny et al., 2023; Zhang et al., 2026). This research demonstrates, by allocating the dissolved ion budgets of the Mackenzie River (sampled upstream of its confluence with the Arctic Red River) among lithologic and meteoric sources, that changes in carbonate and silicate weathering have been sufficient to compensate for increases in sulfide oxidation since 1980. Overall, inorganic chemical weathering reactions in the Mackenzie River have exerted a statistically unchanging influence on pCO_2 over the last 40 years. In contrast, within steeper catchments containing sedimentary rocks, such as the Peel River and certain subcatchments of the Mackenzie River, changes in sulfide oxidation have outpaced changes in other inorganic mineral weathering reactions to result in reduced CO_2 drawdown. Likewise, changes in carbonate and silicate mineral weathering within the Yukon River basin have been insufficient to compensate for increases in sulfide oxidation through time. While a more complete chemical weathering budget would also account for changes in the oxidation of petrogenic organic carbon, the lack of long-term rhenium measurements or radiocarbon observations limits considerations here to the inorganic weathering reactions (Hilton et al., 2014; Hilton and West, 2020; Zondervan et al., 2023; Dean et al., 2025; Grant et al., 2025; Zhang et al., 2026).

2. Theory and calculation: polar perspectives on polar problems

2.1. Inorganic mineral weathering reactions for the combined ocean-atmosphere system

A traditional approach to quantifying CO_2 fluxes associated with chemical weathering is to assume that each charge-equivalent mole of silicate weathering converts 1 mole of atmospheric CO_2 to fluvial bicarbonate (HCO_3^-; eq. 1, with α as a compositional coefficient), that each charge-equivalent mole of carbonate weathering converts half a mole of atmospheric CO_2 to fluvial HCO_3^- (eq. 2, with β as a compositional coefficient), and that each charge-equivalent mole of sulfide oxidation converts 1 mole of fluvial HCO_3^- to atmospheric CO_2 (eq. 3). In this framework, CO_2 drawdown due to chemical weathering is estimated as the sum of silicate-derived charge and half of carbonate-derived charge less sulfide-derived charge. In detail, studies disagree on when and how carbonate weathering and silicate-derived Na^+ or K^+ should be included in such CO_2 drawdown calculations (Gaillardet et al., 1999; Galy and France-Lanord, 1999). Despite the ubiquity of eqs. 1-3, these weathering reactions are not truly generic because HCO_3^- is not conservative in river water (Zeebe and Wolf-Gladrow, 2001). That is, because aqueous carbon speciates among CO_2, HCO_3^-, and carbonate ion (CO_3^{2-}), fluvial HCO_3^- does not necessarily increase and decrease with ALK in the 1:1 fashion suggested by the given reactions. For example, consider that in acid mine drainage with very low pH, each additional unit of sulfide oxidation could not convert a charge-equivalent quantity of HCO_3^- to CO_2 if the river had already degassed all of its dissolved carbon. At the high-pH end of the acidity spectrum, the addition of weathering-derived ALK could be accommodated through conversion of HCO_3^- to CO_3^{2-} without a charge-equivalent conversion of atmospheric CO_2 to fluvial HCO_3^-. While the classical equations may describe the chemical mechanism underlying certain types of weathering reactions, their built-in assumption regarding the relationship between landscape-scale ALK production or loss and the

conversion between CO_2 and HCO_3^- adds substantial complexity and imprecision to the tabulation of weathering-associated carbon fluxes.

$$CO_2 + \frac{1}{2}Ca_\alpha Na_{2(1-\alpha)}SiO_3 + \frac{1}{2}H_2O \rightarrow HCO_3^- + \frac{\alpha}{2}Ca^{2+} + (1-\alpha)Na^+ + \frac{1}{2}SiO_2 \quad \text{(eq. 1)}$$

$$\frac{1}{2}CO_2 + \frac{1}{2}H_2O + \frac{1}{2}Ca_\beta Mg_{1-\beta}CO_3 \rightarrow HCO_3^- + \frac{\beta}{2}Ca^{2+} + \frac{(1-\beta)}{2}Mg^{2+} \quad \text{(eq. 2)}$$

$$HCO_3^- + \frac{1}{4}FeS_2 + \frac{15}{16}O_2 \rightarrow CO_2 + \frac{1}{2}H_2O + \frac{1}{2}SO_4^{2-} + \frac{1}{8}Fe_2O_3 \quad \text{(eq. 3)}$$

The problem of non-conservative aqueous carbon dynamics can be mitigated by quantifying the release of carbon into the total ocean-atmosphere system, initially without concern for its distribution between ocean and atmosphere (Torres et al., 2016). In practice, removing the functional linkage between atmospheric CO_2 and fluvial HCO_3^- from the weathering reactions is accomplished by writing each chemical species in the form it would occupy at the carbonic acid equivalence point, such that the final stoichiometric factors on H^+ and CO_2 or H_2CO_3 refer to the change in ALK and inorganic carbon inventory of the combined ocean-atmosphere system (eqs. 4 - 7; Zeebe and Wolf-Gladrow, 2001). The latter quantity has recently been dubbed fluid inorganic carbon (FIC) and is equal to the sum of dissolved inorganic carbon (DIC) and atmospheric CO_2 (Kemeny et al., 2024). The variable FIC has previously been called inorganic carbon (IC; Kemeny et al., 2023) and, confusingly, was also previously referenced simply as DIC (Torres et al., 2016; Kemeny et al., 2021; Kemeny and Torres, 2021). For this work, FIC will refer to the total inorganic carbon content of the ocean-atmosphere system and DIC will refer to the dissolved inorganic carbon content of a particular parcel of water.

$$H^+ + \frac{1}{2}Ca_\alpha Na_{2(1-\alpha)}SiO_3 \rightarrow \frac{\alpha}{2}Ca^{2+} + (1-\alpha)Na^+ + \frac{1}{2}SiO_2 + \frac{1}{2}H_2O \quad \text{(eq. 4)}$$

$$H^+ + \frac{1}{2}Ca_\beta Mg_{1-\beta}CO_3 \rightarrow \frac{\beta}{2}Ca^{2+} + \frac{(1-\beta)}{2}Mg^{2+} + \frac{1}{2}H_2O + \frac{1}{2}CO_2 \quad \text{(eq. 5)}$$

$$\frac{1}{4}FeS_2 + \frac{15}{16}O_2 + \frac{1}{2}H_2O \rightarrow H^+ + \frac{1}{2}SO_4^{2-} + \frac{1}{8}Fe_2O_3 \quad \text{(eq. 6)}$$

$$CH_2O + O_2 \rightarrow H_2O + CO_2 \quad \text{(eq. 7)}$$

The dissolution of silicate minerals adds ALK to the ocean-atmosphere system without modifying FIC (eq. 4). Where the ALK produced by silicate weathering was previously implied to convert CO_2 to HCO_3^- (eq. 1), the reaction now simply increases total ocean-atmosphere ALK. Carbonate mineral weathering adds ALK and FIC to the ocean-atmosphere system in a 2:1 ratio (eq. 5). In contrast, the production of sulfuric acid through oxidation of minerals such as pyrite (FeS_2) removes ALK without modifying FIC (eq. 6; Spence and Telmer, 2005). Note that this claim does not mean that sulfide oxidation does not ever modify the HCO_3^- content of a specific water parcel, but instead that the total quantity of inorganic carbon in the ocean-atmosphere system is not directly modified by sulfide oxidation acting in isolation. The updated carbonate weathering and silicate weathering reactions are agnostic as to whether the H^+ consumed during weathering is sourced from carbonic acid or sulfuric acid, which is acceptable because the ALK ramifications from sulfuric acid generation are treated independently (eq. 6). Furthermore, given that the definition of ALK is relative to the modern carbon system, formation of carbonic acid does not modify the total ALK of the ocean-atmosphere system (Zeebe and Wolf-Gladrow, 2001). Lastly, aerobic oxidation of organic carbon adds FIC to the ocean-atmosphere system without modifying ALK, ignoring any role of organic nitrogen, phosphorus, or sulfur (eq. 7). The net changes in ocean-atmosphere ALK and FIC due to a system of weathering reactions are respectively indicated as Δ(ALK) and Δ(FIC). Again, note that Δ(FIC) is different from the in-situ DIC content of a water

sample. While a river without any chemical weathering in its catchment would still have nonzero DIC due to gas exchange with the atmosphere, nonzero Δ(FIC) requires biogeochemical processes that change the inorganic carbon content of Earth's ocean-atmosphere system.

The change in pCO_2 due to Δ(ALK) and Δ(FIC) fluxes from a chemical weathering system reflects the repartitioning of carbon between the atmosphere and hydrosphere in response to the updated quantities of ALK and FIC in the ocean-atmosphere system. In that such a framework considers the response of atmospheric pCO_2 to changes in ocean-atmosphere conditions, any calculated change in pCO_2 following shifts in chemical weathering reactions would only be realized over durations longer than the decadal timescales required for air-sea gas exchange. This perspective is conceptually distinct from conventional approaches that quantify a near-instantaneous relationship between production of fluvial HCO_3^- from atmospheric CO_2 during chemical weathering. Over timescales longer than gas exchange, the framework built around Δ(ALK) and Δ(FIC) provides an improved model for calculating the impact of chemical weathering on pCO_2 because it quantifies the impacts of weathering on the distribution of carbon rather than assuming a fixed relationship between production or loss of HCO_3^- based on production or loss of ALK. On timescales longer than carbonate compensation, sedimentary outputs from the ocean will adjust to inputs of ALK and FIC such that changes in pCO_2 become more complex than simply accounting for air-sea gas exchange. Overall, the calculations described here are thus only relevant on timescales longer than air-sea gas exchange but shorter than carbonate compensation; this is essentially the intermediate timescale over which the surface ocean and atmosphere communicate regarding disequilibria in aqueous carbon chemistry. This intermediate timescale has particular relevance to humanity and can be studied without resolving the full Earth-system

response to chemical weathering. Tabulating CO_2 fluxes on timescales shorter than gas exchange or timescales longer than carbonate compensation is beyond the scope of this analysis.

Calculation with CO2SYS indicates that $\Delta(ALK)/\Delta(FIC) = 1.09$ is the key ratio for evaluating how modern chemical weathering impacts pCO_2 over timescales longer than the decades required for gas exchange but shorter than the 5-10 kyr required for carbonate compensation (Archer et al., 1997; Lewis and Wallace, 1998; Fig. 2). Over this intermediate timescale, a weathering system with $\Delta(ALK)/\Delta(FIC) > 1.09$ will result in lower pCO_2 and a weathering system with $\Delta(ALK)/\Delta(FIC) < 1.09$ will result in elevated pCO_2 (Torres et al., 2016). The $\Delta(ALK)/\Delta(FIC)$ threshold of 1.09 is equivalent to $\Delta(FIC)/\Delta(ALK) = 0.92$, or a slope of 0.92 on a plot of $\Delta(FIC)$ against $\Delta(ALK)$, which means that pCO_2 contours lie at an angle of approximately 42.5° relative to the positive $\Delta(ALK)$ axis.

2.2. Polar perspective

The $\Delta(ALK)$ and $\Delta(FIC)$ fluxes of a weathering system define a vector that impacts the global carbon cycle by causing the ocean-atmosphere system to cross contours of atmospheric pCO_2 (Fig. 3; Table 1). To simplify calculations for the number of pCO_2 contours crossed due to chemical denudation, the net weathering vector can be recast in polar coordinates as an angle relative to the positive $\Delta(ALK)$ axis ($\phi = \tan^{-1}(\Delta(FIC)/\Delta(ALK))$, ranging from 0° to 360°), a magnitude ($R=\mathrm{sqrt}(\Delta(ALK)^2+ \Delta(FIC)^2)$, with $0 < R < \infty$), and a normalized magnitude ($r = R/R_{initial}$, where $R_{initial}$ is a nonzero initial or reference value) (Fig. 3B). The magnitude of the weathering vector is a function of $\Delta(ALK)$ and $\Delta(FIC)$ rather than the absolute ion fluxes moving through river water; it is possible to add Ca^{2+} and SO_4^{2-} to river water, such as through gypsum dissolution or equal amounts of sulfide oxidation and silicate weathering, that would increase

fluvial mass flux but not modify the magnitude of the chemical weathering vector. Within this framework, $\Delta(FIC) = R*\sin(\phi)$ and $\Delta(ALK) = R*\cos(\phi)$, and $\Delta(FIC)_{norm} = r*\sin(\phi)$ and $\Delta(ALK)_{norm} = r*\cos(\phi)$, with the subscript norm indicating that the ALK or FIC flux has been normalized (Fig. 3B). The utility of the polar transformation lies in its ability to derive changes in the number of crossed pCO_2 contours due to shifts in chemical weathering by simultaneously accounting for changes in both the $\Delta(ALK)/\Delta(FIC)$ ratio, which manifest as shifts in ϕ, and changes in the magnitude of the weathering vector, which manifest as shifts in r.

This analysis assumes that pCO_2 contours are parallel and linearly spaced (Fig. 3B). In that pCO_2 contours can then be packed at arbitrary density, the change in crossed pCO_2 contours due to chemical weathering processes is defined relative to the maximum number of contours that could be crossed on the normalized unit circle (r = 1). The normalized number of crossed pCO_2 contours is indicated as γ. Negative values of γ lie below the pCO_2 contour of the initial state and indicate that chemical processes move the ocean-atmosphere system to lower pCO_2 values, while positive values of γ lie above the pCO_2 contour of the initial state and indicate that chemical processes move the ocean-atmosphere system to higher pCO_2 values. The maximum contour-crossing vector occurs when moving along a line orthogonal to pCO_2 contours. This convention establishes that γ ranges between -1 and 1 on the unit circle, with the maximum γ value at 132.5° (90° anticlockwise from 42.5°, for the largest increase in atmospheric pCO_2), the minimum γ value at 312.5° (270° anticlockwise from 42.5°, for the largest decline in atmospheric pCO_2), and with γ equal to zero at 42.5° and 222.5° (the latter being 180° offset from 42.5°, for no change in atmospheric pCO_2) at modern ocean-atmosphere conditions. The selection of sparser or denser contour spacing would modify absolute values of γ but would not impact calculations of when trends in γ are significant or the value of fractional changes in γ. Overall, the main innovation of

the present work is quantifying Arctic weathering systems in terms of changes in γ values rather than in terms of absolute ion fluxes or $\Delta(ALK)/\Delta(FIC)$ ratios alone.

Within the polar framework, silicate weathering lies along the positive x-axis with $\phi = 0°$ and $\gamma = -0.68$ for $r = 1$ (eq. 4, Figs. 3A and B). Sulfide oxidation has the opposite nature as silicate weathering, with $\phi = 180°$ and $\gamma = 0.68$ for $r = 1$ (eq. 6). Carbonate weathering, with $\Delta(ALK)/\Delta(FIC) = 2$, lies at an angle $\phi = \tan^{-1}(1/2) = 26.6°$ and has $\gamma = -0.27$ for $r = 1$ (eq. 5). Weathering vectors with $\phi > 26.6°$ can be reached by combining carbonate weathering, silicate weathering, and sulfide oxidation; for example, a weathering system with 2 moles of ALK production through carbonate weathering, 1 mole of ALK production through silicate weathering, and 2.5 moles of ALK removal through sulfide oxidation would have $\Delta(ALK) = 0.5$ moles, $\Delta(FIC) = 1$ mol, and $\phi = \tan^{-1}(1/0.5) = 63.4°$. Because weathering systems tend to operate as short-term pCO_2 sinks, meaning that they have $\Delta(ALK)/\Delta(FIC) > 1.09$, ϕ values will often lie between 0° and 42.5° (Fig. 3, yellow shading).

For a change in the magnitude or angle of the chemical weathering vector, the fractional change in crossed pCO_2 contours is the fractional change in γ, indicated as λ ($\gamma/\gamma_{initial}$-1, reported in %; Table 1). Because most γ values considered in this work are negative, positive values of λ in this article generally indicate that changes in weathering move the ocean-atmosphere system towards a lower pCO_2 contour and negative values of λ generally indicate that changes in weathering move the ocean-atmosphere system towards a higher pCO_2 contour.

Given an increase in the normalized weathering magnitude r, there exists a range of ϕ values above the initial ϕ value that can result in positive λ, meaning enhanced CO_2 drawdown, despite the lower $\Delta(ALK)/\Delta(FIC)$ ratio (Fig. 3B, green shading). Moreover, larger increases in r allow for larger increases in ϕ without reducing the number of pCO_2 contours crossed by the

weathering vector (Fig. 3C, green shading). Rotations of the weathering vector can thus be offset by changes in weathering magnitude to result in a constant impact of weathering on pCO_2 over timescales longer than air-sea gas exchange. Colloquially, increases in the magnitude of chemical weathering can compensate for reductions in the efficiency of chemical weathering. When increases in r are insufficient to compensate for increases in ϕ (Fig. 3B and 3C, purple shading), changes in weathering would act to reduce CO_2 drawdown following expectations based only on the reduced $\Delta(\mathrm{ALK})/\Delta(\mathrm{FIC})$ ratio.

To understand the coordinate system more fully, consider a weathering system with a vector whose end-point lies on a pCO_2 contour corresponding to reduced pCO_2 relative to the pCO_2 contour of the initial condition ($\gamma_{\mathrm{initial}} < 0$). If additional chemical weathering reactions increased the $\Delta(\mathrm{FIC})$ of the weathering system without altering $\Delta(\mathrm{ALK})$, such as charge-equivalent quantities of sulfide oxidation and carbonate mineral weathering (eqs. 5 and 6), the updated chemical weathering vector would have a lower $\Delta(\mathrm{ALK})/\Delta(\mathrm{FIC})$ ratio with higher values for both ϕ and r. The net chemical weathering vector would also then necessarily lie on a higher pCO_2 contour than the initial condition ($\gamma_{\mathrm{updated}} > \gamma_{\mathrm{initial}}$), although this updated pCO_2 contour need not be higher than a situation without any weathering ($\gamma_{\mathrm{updated}}$ does not need to be > 0). If $\gamma_{\mathrm{updated}}$ remains < 0 following the change in weathering fluxes, meaning that the weathering system still operates as a sink for atmospheric CO_2, increasing the overall magnitude of weathering could then restore $\gamma_{\mathrm{updated}}$ to $\gamma_{\mathrm{initial}}$.

The required change in weathering magnitude to compensate for increases in ϕ is non-linear (Fig. 3D). When the weathering vector angle initially has a low value, such as that characterizing silicate weathering, changes in ϕ can be accommodated by modest changes in r. For example, at an initial ϕ value of 7.5°, moving to a ϕ value of 12.5° requires that r increase by only

316 15% to remain on the same pCO_2 contour (Fig. 3D). In contrast, remaining on the same pCO_2
317 contour for a 5° increase from an initial ϕ value of 27.5° requires that r change by approximately
318 49%. This non-linearity reflects the relative geometry of the weathering vector and pCO_2 contours,
319 with the two becoming increasingly close to parallel as the weathering vector approaches $\phi = 42.5°$.
320 Changes in r cannot compensate for changes in ϕ beyond this critical angle as the sign of the impact
321 of weathering on pCO_2 switches from a CO_2 sink to a CO_2 source. The non-linearity means that
322 increases in weathering magnitude can more readily compensate for $\Delta(ALK)/\Delta(FIC)$ declines at
323 low ϕ values. This non-linearity also means that accounting for the influence of weathering
324 magnitude on CO_2 drawdown becomes relatively less important as the weathering vector
325 approaches ϕ=42.5°. At exactly this angle, no magnitude of weathering results in changes to pCO_2
326 because weathering simply moves the ocean-atmosphere system along the initial pCO_2 contour. In
327 detail, this claim breaks down when sufficient ALK and FIC have been added to the ocean-
328 atmosphere system that the slope of the pCO_2 contours is modified from the initial value (Fig. 2).
329
330 **2.3. Polar calculations**
331 Any combination of ϕ and r is associated with a specific pCO_2 contour with slope $m_{contour}$
332 (eq. 8; Fig. 4, grey dotted lines). For modern conditions, pCO_2 contours occur at $\phi = 42.5°$ in the
333 space of $\Delta(FIC)_{norm}$ against $\Delta(ALK)_{norm}$, corresponding to $m_{contour} = 0.92$ (Fig. 2). Knowing this
334 slope, the y-intercept of the pCO_2 contour associated with a given normalized weathering vector
335 ($\Delta(FIC)_{norm}^{intercept}$) can be calculated without knowing the absolute pCO_2 value of that contour (eq.
336 9). The value of r required to stay on a given pCO_2 contour as a function of ϕ is then simply the
337 ratio of the contour intercept to the difference between $\sin(\phi)$ and $m_{contour}*\cos(\phi)$ at the updated ϕ
338 value (eq. 9; Fig. 3D). The reverse case, of calculating the ϕ value required to be on a pCO_2 contour

at a given r, is solved by substituting the equation of the pCO_2 contour (eq. 8) into the equation of a circle with radius r (eq. 10) and rearranging to reach a quadratic expression in $\Delta(ALK)_{norm}$ (eq. 11). Once solved, ϕ can be calculated as $\phi = \cos^{-1}(\Delta(ALK)_{norm}/r)$.

$$\Delta(FIC)_{norm} = m_{contour} * \Delta(ALK)_{norm} + \Delta(FIC)_{norm}^{intercept} \quad \text{(eq. 8)}$$

$$\Delta(FIC)_{norm}^{intercept} = r * (\sin(\phi) - m_{contour} * \cos(\phi)) \quad \text{(eq. 9)}$$

$$r^2 = \Delta(ALK)_{norm}^2 + \Delta(FIC)_{norm}^2 = \Delta(ALK)_{norm}^2 + \left(m_{contour} * \Delta(ALK)_{norm} + \Delta(FIC)_{norm}^{intercept}\right)^2 \quad \text{(eq. 10)}$$

$$(1 + m_{contour}^2)\Delta(ALK)_{norm}^2 + 2m_{contour}\Delta(FIC)_{norm}^{intercept}\Delta(ALK)_{norm} + \left(\left(\Delta(FIC)_{norm}^{intercept}\right)^2 - r^2\right) = 0 \quad \text{(eq. 11)}$$

When calculating γ, normalization to the maximum contour-crossing vector on the unit circle is necessary as the assumption of parallel and linearly spaced pCO_2 contours enables arbitrarily fine contour divisions. The maximum contour-crossing vector is orthogonal to the parallel pCO_2 contours and is defined by the equation $\Delta(FIC)_{norm} = -\Delta(ALK)_{norm}/m_{contour}$ (Fig. 4A, thick black line); note that this line has the negative inverse slope of the pCO_2 contours, -1.09, and forms an angle of 132.5° with the positive $\Delta(ALK)_{norm}$ axis when pCO_2 contours have an angle of 42.5°. For a given weathering system, the number of crossed pCO_2 contours normalized to the unit circle maximum is equal to the magnitude of a vector starting at the origin and ending at the intersection between the pCO_2 contour of the normalized weathering vector and the line orthogonal to the pCO_2 contours (eqs. 12 - 14). The value of γ simplifies to the intercept of the pCO_2 contour of the normalized weathering vector divided by the square root of one plus the square of the contour slope, which is ultimately a straightforward function of r, ϕ, and $m_{contour}$ (eq. 15).

$$\Delta(\mathrm{FIC})_{\mathrm{norm}}^{\mathrm{intersection}} = -\frac{\Delta(\mathrm{ALK})_{\mathrm{norm}}^{\mathrm{intersection}}}{m_{\mathrm{contour}}} = m_{\mathrm{contour}}\Delta(\mathrm{ALK})_{\mathrm{norm}}^{\mathrm{intersection}} + \Delta(\mathrm{FIC})_{\mathrm{norm}}^{\mathrm{intercept}} \quad \text{(eq. 12)}$$

$$\Delta(\mathrm{ALK})_{\mathrm{norm}}^{\mathrm{intersection}} = \frac{-m_{\mathrm{contour}} * \Delta(\mathrm{FIC})_{\mathrm{norm}}^{\mathrm{intercept}}}{1+m_{\mathrm{contour}}^2} \quad \text{(eq. 13)}$$

$$\Delta(\mathrm{FIC})_{\mathrm{norm}}^{\mathrm{intersection}} = \frac{\Delta(\mathrm{FIC})_{\mathrm{norm}}^{\mathrm{intercept}}}{1+m_{\mathrm{contour}}^2} \quad \text{(eq. 14)}$$

$$\gamma = \sqrt{\left(\Delta(\mathrm{ALK})_{\mathrm{norm}}^{\mathrm{intersection}}\right)^2 + \left(\Delta(\mathrm{FIC})_{\mathrm{norm}}^{\mathrm{intersection}}\right)^2} = \frac{\Delta(\mathrm{FIC})_{\mathrm{norm}}^{\mathrm{intercept}}}{\sqrt{1+m_{\mathrm{contour}}^2}} = \frac{r*(\sin(\phi)-m_{\mathrm{contour}}*\cos(\phi))}{\sqrt{1+m_{\mathrm{contour}}^2}} \quad \text{(eq. 15)}$$

This polar framework finds that the capacity of weathering to modify pCO_2 is proportional to the difference between $\sin(\phi)$ and $m_{contour}*\cos(\phi)$ (eq. 15), which is equivalent to being proportional to the difference between $\Delta(FIC)/m_{contour}$ and $\Delta(ALK)$. Recalling that $\Delta(ALK)$ reflects the charge-equivalent contribution from silicate and carbonate weathering plus the negative contribution from sulfide oxidation and $\Delta(FIC)$ reflects the mole-equivalent contribution from carbonate weathering, the equation for γ can be understood as a proportionality in terms of the charge released during weathering reactions (eq. 16 where "silicate", "carbonate", and "sulfide" refer to the charge released through the corresponding reactions). This result differs from existing conventions for tabulating CO_2 drawdown, where the change in CO_2 due to chemical weathering reflects the same terms but without the scaling for $m_{contour}$ (eq. 17). The two frameworks would converge where $m_{contour} = 1$.

$$\gamma \propto (\sin(\phi) - m_{\mathrm{contour}} * \cos(\phi)) \propto \left(\Delta(\mathrm{ALK}) - \frac{\Delta(\mathrm{FIC})}{m_{\mathrm{contour}}}\right) = (\mathrm{silicate} + \mathrm{carbonate} - \mathrm{sulfide}) - \left(\frac{\mathrm{carbonate}}{2*m_{\mathrm{contour}}}\right) = \mathrm{silicate} + \left(1 - \frac{1}{2*m_{\mathrm{contour}}}\right)\mathrm{carbonate} - \mathrm{sulfide} \quad \text{(eq. 16)}$$

$$\text{Conventional } CO_2 \text{ drawdown} \propto \mathrm{silicate} + \frac{1}{2}\mathrm{carbonate} - \mathrm{sulfide} \quad \text{(eq. 17)}$$

2.4. The pCO_2 impacts of changes in weathering depend on the balance among reactions

Recent research has suggested that an appreciable fraction of fluvial sodium (Na^+) in global rivers may derive from sediment-associated exchange reservoirs rather than from the weathering of primary silicate minerals (Tipper et al., 2021). If such sediment-water cation exchange is extensive, the dominant chemical weathering processes altering Δ(ALK) and Δ(FIC) through time within Arctic catchments may be sulfide oxidation and carbonate weathering (evaporite dissolution has Δ(ALK)=Δ(FIC)=0). It is notable, then, that changes in carbonate weathering and sulfide oxidation do not necessarily modify pCO_2 over timescales longer than air-sea gas exchange and shorter than carbonate compensation. This claim can be understood by considering the relationship between changes in weathering-derived Δ(FIC) and Δ(ALK) through time, indicated as δ(FIC) and δ(ALK). When the ratio of δ(FIC) and δ(ALK) is equal to the slope of the pCO_2 contours at current ocean-atmosphere conditions, shifts in weathering reactions move the net weathering vector along the initial pCO_2 contour in the space of Δ(FIC) against Δ(ALK) without removing the weathering vector from that contour (Fig. 4B; eqs. 18 and 19).

$$m_{contour} = \frac{\delta(FIC)}{\delta(ALK)} = \frac{\frac{1}{2}*\delta(ALK)_{carbonate\ weathering}}{\delta(ALK)_{carbonate\ weathering}+\delta(ALK)_{sulfide\ oxidation}} \quad \text{(eq. 18)}$$

$$\delta(ALK)_{sulfide\ oxidation} = \frac{(1-2*m_{contour})}{2*m_{contour}} * \delta(ALK)_{carbonate\ weathering} \quad \text{(eq. 19)}$$

If $m_{contour} = 1$, changes in chemical weathering would keep the net weathering vector on the original pCO_2 contour when twice as much change in carbonate weathering occurs as change in sulfide oxidation. For example, if $\delta(ALK)_{sulfide\ oxidation} = -1$, $\delta(FIC)/\delta(ALK) = m_{contour} = 1$ is attained when $\delta(ALK)_{carbonate\ weathering} = 2$. An increase in carbonate-derived ALK that exceeds twice the absolute magnitude of the increase in ALK removed through sulfide oxidation

406 would result in movement to a lower pCO_2 contour, whereas an increase in carbonate weathering
407 that is less than twice the increase in sulfide oxidation would result in movement towards a higher
408 pCO_2 contour. For modern conditions with $m_{contour} = \tan(42.5°) = 0.92$, each mole of ALK
409 removed through increases in sulfide oxidation would actually have to be offset by 2.2 additional
410 moles of ALK produced through carbonate weathering for the net weathering vector to remain on
411 the initial pCO_2 contour. For example, if chemical weathering produced an additional 2.2 moles
412 of ALK through enhanced carbonate weathering and removed an additional mole of ALK through
413 enhanced sulfide oxidation, the net balance would be $\delta(\mathrm{FIC})/\delta(\mathrm{ALK}) = 1.1/1.2 = 0.92$ and the
414 net weathering vector would rotate along the initial pCO_2 contour. These examples demonstrate
415 that shifts in sulfide oxidation and carbonate weathering through time do not always increase pCO_2
416 over intermediate timescales. Rather, if environmental conditions promote joint changes in sulfide
417 oxidation and carbonate weathering, the magnitude of those changes relative to the slope of pCO_2
418 contours will determine whether the change in chemical weathering acts to increase or reduce
419 weathering-associated CO_2 drawdown (Fig. 4B).

420 As a motivating calculation, it is helpful to consider whether major ion data from the Yukon
421 River suggest, in a first-order fashion, that increases in carbonate mineral weathering through time
422 may have partially or even fully compensated for increases in sulfide oxidation. Theil-Sen fits to
423 the Yukon River data reported in Toohey et al. (2016) indicate that the annual flux of SO_4^{2-} in the
424 Yukon River increased by 1.61 Geq/yr from the mid-1980s to the mid-2010s while the
425 corresponding fluxes of calcium (Ca^{2+}), magnesium (Mg^{2+}), and Na^+ increased by 1.51 Geq/yr,
426 1.01 Geq/yr, and 0.16 Geq/yr, for a total change in Σ^+ of 2.68 Geq/yr ($\Sigma^+ = Ca^{2+} + Mg^{2+} + Na^+$, in
427 units of charge equivalents). If the increase in SO_4^{2-} flux derived fully from sulfide oxidation and
428 the increase in cation fluxes derived fully from carbonate weathering (allowing that fluvial Na^+

429 may record charge released from carbonate dissolution as proposed in Tipper et al. (2021)), the
430 ratio of the increase in carbonate-derived ALK to the increase in the absolute value of sulfide-
431 derived ALK would be 1.67, with a δ(FIC)/δ(ALK) ratio of 1.25. Although the δ(FIC)/δ(ALK)
432 slope exceeds 0.92, meaning that the increase in carbonate weathering would have been
433 insufficient to fully compensate for the increase in sulfide oxidation, it is clear that elevated
434 carbonate weathering through time would still have offset a sizable fraction of the pCO_2 impacts
435 from elevated sulfide oxidation. Overall, if an increase in sulfide oxidation through time has
436 reduced the capacity of chemical weathering to draw down CO_2, that effect is manifest through
437 only a portion of the total change in SO_4^{2-} flux within the Yukon River.

438 Modest contributions from silicate weathering and evaporite dissolution to the observed
439 changes in Σ^+ and SO_4^{2-} fluxes can further reduce the pCO_2 impacts from apparent increases in
440 sulfide oxidation. In the case of silicate mineral weathering, only 1 additional mole of ALK
441 production is required to compensate each additional mole of ALK consumption through sulfide
442 oxidation. Such 1:1 balancing reflects that weathering of silicate minerals does not modify FIC
443 and contrasts markedly with the 2.2:1 ALK flux ratio required for increases in carbonate
444 weathering to nullify the pCO_2 impacts of increases in sulfide oxidation. This difference between
445 carbonate and silicate weathering means that each charge-equivalent mole of the increase in Ca^{2+},
446 Mg^{2+}, or Na^+ attributed to silicate weathering decreases the enhancement in carbonate weathering
447 required to remain on the initial pCO_2 contour by 2.2 moles of ALK production. For the Yukon
448 River observations, the δ(FIC)/δ(ALK) ratio decreases from 1.25 to 1.06 when even 15% of the
449 change in Ca^{2+}, Mg^{2+}, and Na^+ fluxes is ascribed to silicate weathering.

450 Accounting for changes in evaporite dissolution has a similar functional effect as
451 accounting for changes in silicate weathering. While potentially counterintuitive, this similarity

occurs because attributing increases in fluvial SO_4^{2-} to gypsum or epsomite dissolution means that SO_4^{2-} which would otherwise be attributed to sulfide oxidation is instead compensated by a charge-equivalent quantity of cations. Because this 1:1 compensation ratio for sulfate salt dissolution is again lower than the 2.2:1 ratio required for carbonate weathering to compensate for sulfide oxidation, each charge-equivalent mole of SO_4^{2-} increase attributed to evaporite dissolution also decreases the enhancement in carbonate weathering required to stay on an initial pCO_2 contour by 2.2 moles of ALK production. For the Yukon River observations, the δ(FIC)/δ(ALK) ratio decreases from 1.25 to 1.10 when 20% of the increase in SO_4^{2-} flux is attributed to evaporite dissolution rather than sulfide oxidation (with a corresponding quantity of cations attributed to evaporite dissolution rather than carbonate weathering).

Combining the two scenarios, the Yukon River δ(FIC)/δ(ALK) ratio, evaluated over the prior decades, decreases from 1.25 to 0.91 when 20% of the increase in SO_4^{2-} flux is ascribed to evaporite dissolution rather than sulfide oxidation and 15% of the increases in Ca^{2+}, Mg^{2+}, and Na^{+} are ascribed to silicate weathering rather than carbonate weathering. Under such conditions, the observed changes in Yukon River chemistry would indicate that chemical weathering became marginally more effective, rather than less effective, at lowering pCO_2 during the observation period. These results indicate that accounting for secondary contributions (~10-20%) from silicate weathering and evaporite dissolution to the observed changes in fluvial dissolved load is essential for accurately quantifying the impacts of thaw-driven weathering on pCO_2. This level of sensitivity is, unfortunately, at or beyond the resolving power of most inversion calculations and highlights a need for substantial further improvements in both the mathematical frameworks used for such calculations and in the diversity and quality of geochemical data that they rely upon. Additionally, these results highlight that converting increases in SO_4^{2-} fluxes directly into CO_2 fluxes without

475 accounting for corresponding increases in the flux of other ions can result in overestimates for the
476 impact of changing sulfide oxidation on pCO_2.
477
478 **3. Methods**
479 **3.1. River dissolved solute compilation**
480 This analysis focused on the Yukon River sampled at Pilot Station and the Mackenzie River
481 sampled upstream of its confluence with the Arctic Red River, as well as the Peel River sampled
482 above Fort McPherson and twelve subcatchments of the Mackenzie River (Fig. 1; Table 2). These
483 river systems were selected due to their potential influence on biogeochemical cycles and the
484 existence of publicly available dissolved chemistry measurements spanning multiple decades.
485 Whereas the vast Yukon River and Mackenzie River catchments integrate across many lithologic,
486 geomorphic, and permafrost regimes (Brabets et al., 2000; Millot et al., 2002, 2003), the smaller
487 and steeper Peel River mostly drains sedimentary rocks and is underlain by continuous and
488 discontinuous permafrost (Obu et al., 2019).
489 Discharge data for the Yukon River were downloaded from the U.S. Geological Survey
490 (Table 2). Discharge data for the Mackenzie River catchments were downloaded from the Canada
491 Historical Hydrometric Data Search, the Real-Time Hydrometric data search, and the Water
492 Survey of Canada index (Table 2). Although discharge data from the Real-Time Hydrometric
493 search are subject to revision in the future, including these data in the present work allowed the
494 analysis to be extended by several years towards the present. Data from the Water Survey of
495 Canada index with a preliminary approval level were included in the discharge compilation while
496 observations with a grade of -2 were removed from consideration. Complete daily discharge
497 records were available for 43 years for the Peel River, 49 years for the Mackenzie River, and 44

498 years for the Yukon River. Years in which > 30% of daily discharge observations were missing
499 were removed from the analysis (2 years each for the Peel River, Mackenzie River, and Yukon
500 River, with one year near the start of each record and the other year being 2026). Missing data in
501 years where ≥ 70% of days had discharge measurements were approximated as the average
502 discharge observations from the same month within three years of the missing date. For the data
503 employed in the analysis, 213,247 daily observations were used as reported and 2,255 daily values
504 were estimated (~1%). The estimated points were mostly in winter months (November, December,
505 January) rather than during the summer and spring months. Discharge since the late 1970s has,
506 while variable, increased significantly in the Yukon River and Peel River (a few percent per
507 decade) but not in the Mackenzie River or most of its subcatchments (Fig. S17).

508 Water quality data for the Yukon River were downloaded from the U.S. Geological Survey
509 (Table 2). Chemical data for the Peel River and the Mackenzie River, as well as the Mackenzie
510 subcatchments, were either downloaded from the Environment and Climate Change Canada
511 website or supplied from the agency upon request. Flagged chemical observations were removed
512 from the compilation, and measurements on samples collected at the same location on the same
513 day were averaged together. Chemical observations for the Yukon River and Mackenzie River
514 were also downloaded from the Arctic Great Rivers Observatory (Arctic Great Rivers Observatory,
515 2026). Flagged chemical observations were again removed from the compilation. The chemical
516 ranges of the Arctic Great Rivers Observatory data were consistent with those of the USGS and
517 ECCC datasets and, in cases where multiple sources report river chemistry on the same day, the
518 data streams were commonly in strong agreement.

519 Due to substantial noise in chemical observations during the early parts of many records,
520 as well as the potential for changes through time in the analytical methods used to determine fluvial

chemistry (Mast, 2013), samples collected before 1975 were removed from the analysis. Furthermore, because many of the aggregated data streams contained anomalously high and low values, points more than 4 standard deviations above or below the mean of the log-normalized observations were removed from the analysis. The aggregated major ion compilation and discharge data are provided in the supplementary materials.

3.2. Weighted Regression on Time, Discharge, and Season (WRTDS)

The compiled chemical observations were scattered throughout each river's hydrograph and were, in isolation, insufficient for calculating annual fluxes. By combining the sporadic observations with daily discharge measurements and a Weighted Regression on Time, Discharge, and Season (WRTDS), daily concentrations of Ca^{2+}, Mg^{2+}, Na^{+}, SO_4^{2-}, chloride (Cl^{-}), and silicon (Si) could be estimated over the shared duration of the chemistry and discharge records (Hirsch et al., 2010; Walsh et al., 2024). The WRTDS approach assigned each observation point a distinct weighting based on its proximity to each estimation point, where proximity reflects the combination of three distance metrics: the difference between the year of the observation and the estimation point, the difference between the season of the observation and the estimation point, and the difference between the discharge of the observation and the estimation point. Because the WRTDS defines a distinct set of weightings for each estimation point, it is particularly useful for calculating daily chemistry in situations where the relationship between concentration and discharge may have changed over the course of the collected data. Following Hirsch et al. (2010), this work used the tricube weighting function with a year half-window width of 10, a seasonal half-window width of 0.5, and a discharge half-window width of 2 natural log units (Tukey, 1977).

543 The standard WRTDS regression of Hirsch et al. (2010) includes multiple fitting
544 parameters and was found to produce artifactual structure in the regression results not supported
545 by the original data. This shortcoming likely reflected an insufficient number of observation points
546 relative to the number of tunable parameters. To avoid this problem, the regression model was
547 instead limited to a weighted version of a classic concentration-discharge relationship in which the
548 logarithm of chemical concentration was set equal to a constant value plus the scaled logarithm of
549 discharge (eqs. 20 and 21). For the i^{th} estimation point with discharge Q_i, parameters k_i and b_i
550 specific to that estimation point were obtained by weighted fitting in MATLAB. The estimated
551 concentration C_i was then obtained by correcting $k_i(Q_i)^{b_i}$ for retransformation bias (Ferguson,
552 1986) using a weighted smearing correction (Duan, 1983; Hirsch et al., 2010; eqs. 22 and 23). The
553 correction factor α_i was calculated separately for each estimation point as the weighted mean of
554 exponentiated residuals for the observations used to constrain k_i and b_i at that point (indexed by j
555 in eq. 23). This approach did not require the assumption that residuals were normally distributed.
556
557 $$C = kQ^b \quad \text{(eq. 20)}$$
558 $$\ln(C) = \ln(k) + b * \ln(Q) \quad \text{(eq. 21)}$$
559 $$C_i = \alpha_i * \exp[\ln(k_i) + b_i * \ln(Q_i)] = \alpha_i k_i (Q_i)^{b_i} \quad \text{(eq. 22)}$$
560 $$\alpha_i = \frac{\Sigma_j^n (w_j * \exp(\varepsilon_j))}{\Sigma_j^n (w_j)}, \text{ where } \varepsilon_j = \ln(C_j) - [\ln(k_i) + b_i * \ln(Q_j)] \quad \text{(eq. 23)}$$
561
562 The regression was only conducted for estimation points that were preceded and followed
563 by at least two chemical observations, thereby restricting estimates to the period bounded by
564 sample collection, and if at least three observations had nonzero weights. Following the
565 regressions, years were excluded from subsequent analysis if fewer than 90% of daily estimation

points within that year were successfully regressed. For retained years, an extremely small number of points (< 0.02%) from January, March, and April needed to be approximated by the mean concentration of successful regression results from the same month within three years of the estimation point. The regression yielded daily estimates of Ca^{2+}, Mg^{2+}, Na^{+}, SO_4^{2-}, Cl^{-}, and Si concentrations broadly consistent with observations (Figs. S3 - S5). Integration of daily regression results also yielded annual SO_4^{2-}, Ca^{2+}, and Mg^{2+} flux estimates in close agreement with prior studies of the same rivers (Fig. S6; Tank et al., 2016; Toohey et al., 2016; Zolkos et al., 2018). Uncertainty in regression results was quantified for each ion at each site as the standard deviation of the distribution of the ratio between observed and regression-estimated dissolved concentrations (Table S1), and this uncertainty was then incorporated in the inversion calculations.

3.3. MEANDIR inversions

Converting daily WRTDS-derived solute estimates into information regarding the timescale-dependent impact of chemical weathering on pCO_2 required quantitatively allocating fluvial dissolved load among end-member solute sources (Négrel et al., 1993; Gaillardet et al., 1999). However, fluvial inversion calculations were recently made more complex by the findings of Tipper et al. (2021), which demonstrated that a substantial fraction of fluvial Na^{+} can derive from sediment-associated exchange of weathering-derived Ca^{2+} and Mg^{2+} rather than from the primary weathering of silicate minerals (Cerling et al., 1989). Accounting for such Na^{+}-Ca^{2+}/Mg^{2+} exchange is potentially important for inversion calculations as the concentration of Na^{+}, after correcting for inputs from meteoric precipitation and evaporite dissolution, is commonly used to constrain inputs from silicate weathering. Indeed, Tipper et al. (2021) found that Na^{+}-Ca^{2+}/Mg^{2+} exchange has potentially resulted in overestimation for the quantity of silicate weathering within

589 the Yukon River and Mackenzie River specifically; as shown above, calculations of weathering-
590 driven CO_2 fluxes can be very sensitive to such changes in the inferred magnitude of silicate
591 weathering. Tipper et al. (2021) proposed a direct correction for Na^+-Ca^{2+}/Mg^{2+} exchange that uses
592 estimates of fluvial suspended sediment load, sediment cation exchange capacity (which can be
593 approximated by the aluminum/Si ratio), and the fraction of Na^+ within the exchange pool. Under
594 this approach, the Na^+ remaining in solution after correction for Na^+-Ca^{2+}/Mg^{2+} exchange can be
595 attributed to silicate weathering. Given the lack of suspended sediment data for the Yukon and
596 Mackenzie, as well as large uncertainties in the other parameters, the magnitude of silicate
597 weathering in this work was instead constrained by including Si observations directly in the
598 inversion calculations. In turn, the quantity of silicate weathering constrained the magnitude of
599 Na^+-Ca^{2+}/Mg^{2+} exchange required to match observed river chemistry.

600 The solute budget of each river water sample was deconvolved into contributions from
601 seven end-members: carbonate mineral weathering, silicate mineral weathering, evaporite
602 dissolution, meteoric precipitation, sulfide oxidation, the addition of Na^+ to river water through
603 exchange, and the loss of Ca^{2+} and Mg^{2+} from river water through exchange, with the final two
604 end-members constrained to have equal charge-equivalent fluxes. For the exchange end-member
605 that removed ions from solution, the relative rate of Ca^{2+} and Mg^{2+} removal was set to equal the
606 relative abundance of Ca^{2+} and Mg^{2+} in each river water sample. For most end-members and
607 chemical ratios, the initial sum-normalized chemical distributions were approximated from the
608 Na^+-normalized ratios of Burke et al. (2018) (Table 3). Special consideration was warranted
609 regarding the $Si/\Sigma^{\pm}$ ratio of the silicate end-member, though, as it regulated both the magnitude of
610 silicate weathering and Na^+-Ca^{2+}/Mg^{2+} exchange ($\Sigma^{\pm} = Ca^{2+} + Mg^{2+} + Na^+ + SO_4^{2-}$, in units of
611 charge equivalents).

612 $Si/\Sigma^{\pm}$ is 0.25 in olivine, 0.5 in diopside, 1.0 in anorthite, and 3.0 in orthoclase. In natural
613 systems, dissolved river chemistry can differ from such mineral ratios as Si released during
614 primary mineral dissolution is commonly taken up into vegetation or incorporated into secondary
615 mineral phases (Alexandre et al., 1997; Cornelis et al., 2011; Frings et al., 2016). While Si isotope
616 ratios can help to diagnose secondary processes (Douthitt, 1982; De La Rocha et al., 2000; Ding
617 et al., 2004; Georg et al., 2006, 2007) and the abundance of Si relative to germanium and its stable
618 isotope ratios can help to distinguish the effects of vegetation from those of secondary phase
619 formation (Baronas et al., 2018), such isotopic information was not available for the Arctic samples
620 that formed the basis of this analysis. Moreover, even for landscapes at steady-state where Si is
621 not retained in the weathering system, the export of Si as phytoliths within river suspended load
622 can decouple dissolved $Si/\Sigma^{\pm}$ ratios from end-member $Si/\Sigma^{\pm}$ ratios.
623 Given that biotic uptake of Si and secondary phase formation were not included in the
624 inversion model, the $Si/\Sigma^{\pm}$ ratio for the silicate end-member reflected the net quantity of Si per unit
625 of charge remaining in the dissolved load following uptake or precipitation. In that this ratio is
626 both unknown and may itself change with time, inversion results were considered where the
627 silicate end-member $Si/\Sigma^{\pm}$ distribution was equal to 0.5 ± 0.25, 1.0 ± 0.5, 1.5 ± 0.5, or 2.0 ± 0.5. It
628 was observed that higher $Si/\Sigma^{\pm}$ end-member ratios required a larger fraction of fluvial Na^+ to have
629 been derived from exchange with Ca^{2+} and Mg^{2+}. This trade-off existed because, as the silicate
630 $Si/\Sigma^{\pm}$ ratio increased, the Si in a water sample was associated with a decreasing quantity of silicate-
631 derived Na^+ and an increased requirement for Na^+ to be sourced through Na^+-Ca^{2+}/Mg^{2+} exchange.
632 While silicate $Si/\Sigma^{\pm}$ was equal to 0.5 ± 0.25 in the preferred model results, the different silicate
633 $Si/\Sigma^{\pm}$ distributions did not alter whether the major trends reported in this work were significant.

Three different types of inversion calculations were performed. In the first type, the compiled dissolved solute observations were inverted with the four different silicate end-member $Si/\Sigma^{\pm}$ distributions. These results were then compared with the results of a second type of inversion where observations were inverted without Si or exchange end-members included but where 0% to 95% of measured Na^+ was manually converted into Ca^{2+} and Mg^{2+} prior to the inversion calculations (Figs. S12 - S14). The purpose of this comparison was to consider how changes in the $Si/\Sigma^{\pm}$ ratio of the silicate end-member relate to changes in the absolute fraction of Na^+ exchanged for Ca^{2+} and Mg^{2+}. One notable shortcoming of this second type of inversion was that elevated fractions of manual Na^+-Ca^{2+}/Mg^{2+} exchange rendered certain samples unphysical as the ratio of Na^+ remaining in the sample to the measured Cl^- concentration fell below the Na^+/Cl^- ratio of the evaporite or meteoric precipitation end-members. Satisfying the Cl^- budget in this case would generally result in excess Na^+ relative to exchange-corrected observations, meaning that the sample was no longer viable within the inversion model. For this reason, it is recommended that inversions seeking to represent Na^+-Ca^{2+}/Mg^{2+} exchange include end-members representing Na^+ release and Ca^{2+}/Mg^{2+} uptake directly rather than performing offline corrections. In the third and final set of inversions, each daily set of chemical observations calculated through the WRTDS regression was inverted using the full set of seven end-members. All 15 rivers were inverted with silicate $Si/\Sigma^{\pm} = 0.5 \pm 0.25$ and 1.0 ± 0.5. The Mackenzie River, Peel River, and Yukon River were also inverted with silicate $Si/\Sigma^{\pm} = 1.5 \pm 0.5$ and 2.0 ± 0.5.

Inversion calculations were conducted using the MEANDIR v1.4 inversion model (Table 3, Figs. S8 - S10; Kemeny and Torres, 2021; Kemeny, 2026). This version of MEANDIR differs from prior editions through the implementation of an updated end-member sampling algorithm for multivariate Gaussian distributions that better aligns the variance of end-member chemical priors

with user-specified values. For all inversions, both sample observations and end-members were normalized to the charge-equivalent sum of Ca^{2+}, Mg^{2+}, Na^{+}, and SO_4^{2-}. Individual inversion attempts were accepted as successful if they recreated between 95% and 105% of all observed values, and the calculations accepted the first 400 successes while attempting up to $1.6*10^6$ simulations for each sample. The inversion of the ~600,000 sample points was completed using the Hydra cluster at the Woods Hole Oceanographic Institution.

Weathering Δ(ALK) was calculated from inversion results as the charge-equivalent Ca^{2+}, Mg^{2+}, and Na^{+} contributions from silicate weathering and carbonate weathering less the charge-equivalent SO_4^{2-} contribution from sulfide oxidation (eqs. 4 - 6). Weathering Δ(FIC) was calculated as the mole-equivalent contribution from carbonate weathering (eq. 5). Daily chemical fluxes were summed to reach annual fluxes. A reference point for evaluating annual change in ϕ and R at each site was calculated as the value, for the first year in which data exist, of a Theil-Sen fit through the medians of annual data. The non-parametric Mann-Kendall test was used to assess the existence of trends in all derived parameters following correction for significant lag-1 autocorrelation (Yue et al., 2002) and the threshold for trend significance was $p = 0.05$. Correction for autocorrelation changed significance in λ only at site LR-18, where an insignificant ($p = 0.19$) trend became significant ($p = 0.03$). The magnitude of significant trends was then quantified as Theil-Sen slopes on annual medians without correction for lag-1 autocorrelation.

4. Results

The dissolved solute compilation, daily WRTDS regression results, summed annual chemical fluxes, and calculated polar parameters are provided in the supplementary materials. Figs. S15 and S16 present summaries of calculated parameters for the Peel River, Mackenzie

River, and Yukon River. Additional supplementary figures show, for the 15 sites in the analysis (Table 2), annual discharge (Fig. S17), Ca^{2+} flux (Fig. S18), Mg^{2+} flux (Fig. S19), Na^{+} flux (Fig. S20), SO_4^{2-} flux (Fig. S21), Cl^{-} flux (Fig. S22), Si flux (Fig. S23), Ca^{2+}/Σ^{+} flux ratio (Fig. S24), Mg^{2+}/Σ^{+} flux ratio (Fig. S25), Na^{+}/Σ^{+} flux ratio (Fig. S26), SO_4^{2-}/Σ^{+} flux ratio (Fig. S27), Cl^{-}/Σ^{+} flux ratio (Fig. S28), Si/Σ^{+} flux ratio (Fig. S29), carbonate weathering flux (Fig. S30), silicate weathering flux (Fig. S31), sulfide oxidation flux (Fig. S32), the fraction of carbonate and silicate weathering Δ(ALK) derived from carbonate weathering (Fig. S33), the fraction of carbonate and silicate weathering Δ(ALK) offset by sulfide oxidation (Fig. S34), discharge-weighted Δ(ALK) (Fig. S35), discharge-weighted Δ(FIC) (Fig. S36), ϕ (Fig. S37), R (Fig. S38), r (Fig. S39), γ (Fig. S40), λ (Fig. S41), and normalized annual weathering vectors (Fig. S42).

4.1. Annual fluxes of SO_4^{2-} and Σ^{+} have increased in the Peel, Mackenzie, and Yukon

Observations from the Peel River above Fort McPherson, the Mackenzie River above the Arctic Red River, and the Yukon River at Pilot Station all show increasing SO_4^{2-}/Σ^{+} ratios through time with seasonal oscillations superimposed on multidecadal trends (Figs. 5A - C). As previously identified in the Yukon River, the Peel River and the Mackenzie River attain their highest SO_4^{2-}/Σ^{+} values at the end of summer, when the active layer is deepest, and their lowest SO_4^{2-}/Σ^{+} values during the late winter and early spring (Kemeny et al., 2023). Regression of the annual flux estimates derived from the WRTDS calculations indicates that, over the observational record, the flux of SO_4^{2-} has increased by approximately 6.4 Geq/decade in the Peel River, 25.2 Geq/decade in the Mackenzie River, and 23.7 Geq/decade in the Yukon River (Fig. S21; note that the given increase in Yukon River SO_4^{2-} flux exceeds the value cited above based on Toohey et al. (2016) as it includes ~10 years of additional data). In concert, the SO_4^{2-}/Σ^{+} ratio has increased by

703 ~0.040/decade in the Peel River, ~0.015/decade in the Mackenzie River, and ~0.029/decade in the
704 Yukon River (Fig. S27). Such increases in both the absolute and relative importance of SO_4^{2-} are
705 consistent with emerging understanding that ongoing permafrost thaw is increasing SO_4^{2-} fluxes
706 within major Arctic river systems (Toohey et al., 2016; Zolkos et al., 2018; Tank et al., 2023).
707 Despite the increasing SO_4^{2-}/Σ^+ ratios, the absolute increase in the flux of cations through
708 time has substantially exceeded the increase in SO_4^{2-} flux across all three river systems (Fig. S7).
709 Fitting Theil-Sen slopes to the annual flux estimates derived from the WRTDS regressions, the
710 change in SO_4^{2-} flux for a given change in Σ^+ is 0.59 for the Peel River, 0.34 for the Mackenzie
711 River, and 0.54 for the Yukon River. These values indicate that, for each charge-equivalent mole
712 of SO_4^{2-} increase, the charge-equivalent flux of cations has increased by approximately 1.7 - 3.0
713 moles. Although SO_4^{2-} is increasing in both absolute flux and relative abundance, the set of
714 chemical weathering reactions sourcing Σ^+ to river water are increasing at a faster collective rate
715 than the set of reactions sourcing SO_4^{2-} to river water. Recalling that increases in carbonate
716 weathering can compensate for the ALK impacts of increases in sulfide oxidation when the change
717 in carbonate-derived Σ^+ matches the change in sulfide-derived SO_4^{2-} in a 2.2:1 ratio, the results of
718 the regression calculations strongly suggest that carbonate and silicate weathering reactions can
719 partially or even fully offset ALK loss associated with sulfide oxidation within certain Arctic
720 weathering systems. Indeed, it is HCO_3^-, rather than SO_4^{2-}, that remains the dominant dissolved
721 anion across nearly all of the river water samples (Fig. S1).
722
723 **4.2. The Δ(ALK)/Δ(FIC) ratio of inorganic chemical weathering is decreasing**
724 MEANDIR inversion results demonstrate that carbonate weathering was the primary
725 source of cations to the Peel River, Mackenzie River, and Yukon River (Figs. S2 and S11; Brabets

et al., 2000; Tank et al., 2012), and that many sites showed increases through time in the chemical fluxes from carbonate weathering, silicate weathering, and sulfide oxidation (Figs. S16 and S30 - S32; Zolkos et al., 2018; Walsh et al., 2024). Overall, 13/15 sites were found to have experienced significant increases in the fraction of carbonate and silicate $\Delta(\mathrm{ALK})$ offset through sulfide oxidation (the parameter Z of Torres et al. (2016)) (Fig. S34). Over both seasonal and decadal timescales, the shifting importance of sulfide oxidation likely reflects both active layer deepening into sulfide-rich regions that were previously frozen and changes in the contributions of short and long flow paths to the active channel (Striegl et al., 2005; Tipper et al., 2006; Keller et al., 2007, 2010; Lehn et al., 2017).

7/15 sites showed significant increases in the fraction of carbonate and silicate $\Delta(\mathrm{ALK})$ derived from carbonate mineral weathering (the parameter R of Torres et al. (2016), which is different from the magnitude of the chemical weathering vector R introduced in this work) and 5/15 sites were found to have experienced significant decreases in the same fraction (Fig. S33). However, such changes were much smaller than those observed in the sulfide oxidation fraction. The inclusion of Si and cation exchange end-members in the inversions generated similar values for the carbonate mineral weathering fraction as exchanging approximately 40-65% of Na^+ observed in the Peel River, approximately 15-30% of Na^+ observed in the Mackenzie River, and approximately 10-60% of Na^+ observed in the Yukon River (Fig. 6). The same calculations demonstrated that, as the fraction of Na^+ exchanged for Ca^{2+} and Mg^{2+} increased, the site-averaged sulfide oxidation weathering fraction tended to increase and the fraction of samples that could be inverted decreased. The increase in sulfide oxidation weathering fraction with increased Na^+-Ca^{2+}/Mg^{2+} exchange reflected that, as Na^+ was removed, the falling Na^+/Cl^- ratio reduced the

quantity of SO_4^{2-} that could be attributed to inputs from evaporite dissolution and meteoric precipitation.

Inversion-constrained median Δ(ALK)/Δ(FIC) ratios mostly fell between 1.09 and 2 for the three primary sites (Figs. 5D - F, S11). This range corresponds to chemical weathering that acts as a sink for pCO_2 over timescales shorter than that required for carbonate compensation (5-10 kyr; Archer et al., 1997) but as a source of pCO_2 over geological timescales (> 5-10 kyr and < 10 Myr, the latter value reflecting the residence time of modern marine SO_4^{2-}) (Torres et al., 2016; Kemeny et al., 2021). This intermediate weathering regime reflects a relatively high degree of sulfide oxidation more commonly associated with mountainous environments than with floodplains (Lupker et al., 2012; Bufe et al., 2021), although a similar range has previously been observed in the Koyukuk River (Kemeny et al., 2023). Overall, inorganic chemical weathering in the Peel River, Mackenzie River, and Yukon River has mostly acted as a short-term CO_2 sink over the observational record.

Temporally, inversion-constrained Δ(ALK)/Δ(FIC) ratios have oscillated seasonally with changes in SO_4^{2-}/Σ^+ but have generally been falling in the Peel, Mackenzie, and Yukon catchments as sulfide oxidation has increased in fractional importance (Figs. 5D - F). The Δ(ALK)/Δ(FIC) decline has been most pronounced in the Peel River and the Yukon River, with a more muted reduction in the Mackenzie River. Simple linear extrapolation of the inversion results shows that typical summertime Δ(ALK)/Δ(FIC) ratios crossed 1.09 in the early 2020s for the Peel River and predicts that wintertime weathering in the Peel River and summertime weathering in the Yukon River will cross the same threshold in the mid-2040s to mid-2050s, altering each system from a short-timescale CO_2 sink to a short-timescale CO_2 source. Indeed, many individual summertime Peel River samples already reflect weathering systems that act as net sources of CO_2 on short

771 timescales, and several samples collected from the Yukon River in August and September are close
772 to the threshold (Figs. 5D and F). As chemical weathering systems approach
773 $\Delta(ALK)/\Delta(FIC)=1.09$, it is important to evaluate whether increases in weathering magnitude have
774 offset declines in the $\Delta(ALK)/\Delta(FIC)$ ratio to preserve the impact of chemical weathering on pCO_2.
775

776 **4.3. The impact of chemical weathering on pCO_2 has been variable across sites**

777 The existence of a tradeoff between the magnitude and angle of the chemical weathering
778 vector was evaluated by considering the changing relationships among ϕ, r, γ, and λ in the historical
779 observations (Table 1). The analysis identified changes in both the angle ϕ and magnitude r of
780 annual weathering vectors across sites, where changes in r reflect the combined influences of both
781 changes in discharge and solute chemistry (Figs. 7A - C and S37 - S39). For the Peel River and the
782 Yukon River, the annual chemical weathering vectors were found to rotate to higher ϕ values
783 (lower $\Delta(ALK)/\Delta(FIC)$) and attain elevated r values (longer arrows) when moving from the 1980s
784 towards the present day (Figs. 7A and C). As expected from the inversion-constrained
785 $\Delta(ALK)/\Delta(FIC)$ ratios (Fig. 5D-F), the rotation of the weathering vector was muted in the
786 Mackenzie River (Fig. 7B). While ϕ has increased by approximately 1.8°/decade in the Peel River
787 and 1.1°/decade in the Yukon River, ϕ in the Mackenzie River has increased by only ~0.6°/decade
788 since 1980 (Fig. S15). Concurrently, while r has increased by 0.12/decade in the Peel River and
789 0.08/decade in the Yukon River, r has increased by only 0.05/decade in the Mackenzie River.
790 The inversion results indicate that λ has decreased significantly in the Peel River system
791 (Fig. 7D) and in the Yukon River system (Fig. 7F) over the duration of the records. In contrast, the
792 analysis did not find that λ has changed significantly within the Mackenzie River sampled above
793 the Arctic Red River ($p = 0.24$, Fig. 7E). The Peel, Mackenzie, and Yukon catchments thus

794 demonstrate two different evolutions of chemical weathering systems through time: weathering in
795 the Mackenzie River showed a relatively small increase in ϕ due to minimal change in
796 $\Delta(ALK)/\Delta(FIC)$ that was compensated by a modest increase in r, while weathering in the Yukon
797 River and Peel River showed increases in ϕ that were too large to be compensated by the observed
798 increases in weathering magnitude.

799 When only considering changes in the $\Delta(ALK)/\Delta(FIC)$ ratio (variable ϕ, constant r), the
800 analysis calculated statistically significant decreases in λ for the Peel River, Mackenzie River, and
801 Yukon River, corresponding to underestimates of weathering-driven CO_2 drawdown (Figs. 7D-F,
802 purple curves). In contrast, when considering only changes in weathering magnitude (constant ϕ,
803 variable r), all three sites were found to have statistically significant increases in λ, corresponding
804 to overestimates of weathering-driven CO_2 drawdown (Figs. 7D-F, blue curves). These opposing
805 results demonstrate the necessity of accounting for the competing influence of changes in both ϕ
806 and r when evaluating the impacts of chemical weathering on pCO_2.

807 Despite enhanced sulfide oxidation through time within the Mackenzie River, the net
808 impact of inorganic chemical weathering on pCO_2 has not changed significantly over the past 40
809 years. In contrast, weathering in the Yukon River and Peel River systems is now significantly less
810 effective at removing CO_2 from the atmosphere. Weathering in the Yukon River system is ~15%
811 less effective at crossing pCO_2 contours than the reference condition and weathering in the Peel
812 River is ~80% less effective at crossing pCO_2 contours than the reference condition, albeit with
813 substantial year-to-year variability. While the exact magnitude of CO_2 drawdown varied across
814 inversions with different silicate $Si/\Sigma^{\pm}$ values, such changes to the inversion model did not alter
815 whether any given λ trend was significant or not (Fig. 7G-I). Overall, this work supports the
816 widespread contention that thaw-driven enhancements in sulfide oxidation can reduce the capacity

817 of high-latitude weathering systems to remove CO_2 and demonstrates that the mechanism is
818 operational within the Peel River and Yukon River catchments, but that it has not yet manifested
819 within existing observations for the Mackenzie River catchment.

820 Analysis of twelve subcatchments in the Mackenzie River Basin with varying permafrost
821 extents further demonstrates that rising SO_4^{2-}/Σ^+ ratios can be offset by increases through time in
822 the total magnitude of inorganic chemical weathering (Fig. 8). Overall, while 10/12 of the
823 investigated subcatchments had significant increases in SO_4^{2-}/Σ^+ through time, only 5/12
824 subcatchments showed significant negative trends in λ (Fig. 8C). Inversion of chemical
825 observations from the South Nahanni River, the Flat River, the Liard River, and the Athabasca
826 River revealed significant shifts toward chemical weathering that was less effective at reducing
827 pCO_2. Unsurprisingly, these are some of the sites that Walsh et al. (2024) previously identified as
828 having experienced the largest changes in sulfide oxidation with increasing temperatures. In
829 contrast, weathering in the Great Bear River catchment has become increasingly effective at
830 reducing pCO_2 through time (Fig. 8C). Much of the positive λ trend for the Great Bear River is
831 driven by an increase in weathering magnitude due to a substantial increase in discharge rather
832 than due to changes in dissolved chemistry (Figs. S17, S37, S38). It is also notable that changes in
833 λ through time are nearly statistically significant for the Mackenzie River sampled at Norman
834 Wells ($p = 0.07$), and that changes in λ through time are significant at this site ($p = 0.04$) for
835 inversions conducted with silicate $Si/\Sigma^{\pm} = 1.0 \pm 0.5$ rather than 0.5 ± 0.25 (Fig. S43). Overall,
836 while some Mackenzie River subcatchments do show significant trends, the impact of weathering
837 on pCO_2 appears not to have changed significantly at the scale of the entire basin (Fig. 7E).
838
839

5. Discussion: chemical weathering reflects shared forcings and mechanistic linkages

Compensating changes in r and ϕ within thawing landscapes are possible but not inevitable; whether they occur may depend on the extent to which underlying weathering reactions respond to shared forcings or are mechanistically coupled (Fig. 9). As a first approach, changes in r and ϕ through time can be understood as arising from thaw-driven exposure of mineral phases and independent enhancements in the relative magnitude of sulfide oxidation, silicate weathering, and carbonate weathering (Fig. 9B, grey arrows supplying H^+ and O_2). Under this view, the observed changes in chemical weathering fluxes would principally reflect the relative abundance of minerals in thawing sediment as modified by mineral-specific reactivities and shifts in the supply of acids and oxidants from the environment. In this case, compensating changes in ϕ and r could arise from simultaneous increases in weathering reactions. While it is reasonable to be skeptical of arguments that require fortuitous flux balancing to prevent changes in pCO_2, it is not the case that all of the weathering systems are found to be in balance. For example, the inversion results indicated that weathering in the South Nahanni River and Flat River has become less efficient at removing CO_2 from the atmosphere through time (Fig. 8C). This finding is consistent with the mountainous topography and sedimentary lithologies of the western Mackenzie River basin, given that areas underlain by sedimentary materials are expected to have higher sulfide abundances than those underlain by crystalline rocks and that erosive regions with steep topography are poised for high rates of sulfide oxidation. Similarly, observations from the Peel River are consistent with exposure of sulfide through formation of thermokarst (Fig. 8C; Zolkos et al., 2018; Zolkos and Tank, 2020). In contrast, sulfide oxidation may be more supply-limited in the interior of the Mackenzie River basin, resulting in relatively less thaw-driven sulfide oxidation and a weathering system that retains its effectiveness in reducing pCO_2 despite thaw. Furthermore, thaw-associated changes in the

length of hydrologic flow paths could alter the time available for weathering reactions to occur, while increases in temperature may alleviate kinetic limitations.

Complicating the preceding view of independent weathering reactions, sulfuric acid produced through sulfide oxidation may itself enhance carbonate mineral weathering by decreasing pH and increasing mineral solubility (Fig. 9B; Bufe et al., 2021). Understanding the potential for such coupling between sulfide oxidation and carbonate mineral weathering is important because, if increases in carbonate mineral weathering naturally emerge from increases in oxidative weathering, the potential for thaw-driven sulfide oxidation to act as a positive feedback on modern climate change may be exaggerated (Zolkos et al., 2018; Walsh et al., 2024). In detail, regenerating the ALK removed by sulfide oxidation through carbonate weathering in a 1:1 fashion would generate positive Δ(FIC) and constant Δ(ALK), resulting in reduced CO_2 drawdown. However, a combination of exposure-driven carbonate weathering and sulfide-associated carbonate weathering could potentially produce the 2.2:1 ratio of carbonate weathering to sulfide oxidation required for the pCO_2 implications of carbonate dissolution to counteract those of sulfide oxidation. Although the hypothesized coupling between sulfide oxidation and carbonate weathering is consistent with observations from some catchments and certainly does occur to varying extents throughout the Arctic, insufficient data currently exist to distinguish the enhancements in carbonate weathering due to sulfide oxidation from those due to thaw-driven changes in exposure. Future measurements of subsurface pCO_2 and pH may help to resolve the relative influences of mineral availability and sulfide oxidation on carbonate weathering fluxes by constraining the degree of system openness, as the degree of chemical communication between the weathering system and the atmosphere partially regulates how oxidative reactions modify the composition of subsurface weathering fluids.

886 Thaw-driven oxidation of petrogenic organic matter and changes in the rates of modern
887 photosynthesis and respiration likely also impact the rates of carbonate and silicate weathering.
888 Particularly outside of mountainous settings, ongoing shrubification and shifts in the structure of
889 wetlands, forests, and grassland systems may modify the short-term carbon cycle and be partially
890 responsible for carbonate and silicate weathering enhancements that offset the impacts of sulfide
891 oxidation on pCO_2 (Myers-Smith et al., 2020). Again, additional geochemical measurements will
892 be required to quantify the role of modern and ancient organic carbon oxidation in driving
893 enhanced weathering fluxes.

894 It is also important to recognize, when considering temporal trends in river water
895 chemistry, that the products of chemical weathering reactions were stored transiently in the
896 subsurface before being exported to and sampled in the active channel (Benettin et al., 2015; Torres
897 and Baronas, 2021). Because changes in system hydrology may be responsible for a component of
898 the observed changes in solute fluxes, year-to-year changes in permafrost chemical weathering
899 fluxes as diagnosed from river water samples do not strictly require synchronous changes in the
900 magnitudes of chemical weathering reactions (Calmels et al., 2011). Rather, observed trends in
901 river solute fluxes reflect changes in the expression of those chemical reactions and the burden
902 that weathering-derived Δ(ALK) and Δ(FIC) fluxes impose on the ocean-atmosphere system. The
903 distinction between chemical and hydrological influences on fluvial chemistry, while key when
904 diagnosing controls on weathering reactions, does not impact calculations of weathering-driven
905 changes in pCO_2 and has diminishing importance over timescales longer than the residence time
906 of groundwater solutes.

907 Overall, changes in chemical weathering reactions within the Peel River, Mackenzie River,
908 and Yukon River likely reflect the availability of weatherable minerals and the time available for

weathering reactions, both of which are linked to geomorphic setting, as well as the degree of coupling among chemical reactions and influences on that coupling from changing ecosystem dynamics. While disentangling these competing mechanisms will require additional measurements in waters collected from active river channels and subsurface fluids, the relative importance and interactions of Arctic weathering processes certainly warrant additional study.

6. Conclusions

Permafrost thaw is altering the delivery of acids and oxidants to subsurface weathering reactors, exerting a feedback of unknown sign on pCO_2 by modifying mineral dissolution and oxidation reactions. This work presented a new polar conceptual framework for quantifying the impacts of chemical weathering systems on atmospheric pCO_2 over timescales longer than ocean-atmosphere gas exchange and shorter than carbonate compensation. The new framework quantifies the effect of chemical weathering on pCO_2 by evaluating the impacts of Δ(ALK) and Δ(FIC) fluxes on the crossing of pCO_2 contours. This approach provides a quantitative framework for determining when changes in the total magnitude of chemical weathering can offset the effects on CO_2 drawdown from shifts in the Δ(ALK)/Δ(FIC) ratio of the weathering system.

Combining the new framework with fluvial inversion calculations demonstrated that increases in the magnitude of carbonate and silicate weathering have, so far, offset the reduction in CO_2 drawdown associated with enhanced sulfide oxidation within the Mackenzie River. Despite increases in SO_4^{2-}/Σ^+ and declines in the weathering Δ(ALK)/Δ(FIC) ratio, the impact of inorganic chemical weathering on pCO_2 has not changed significantly within the Mackenzie River sampled above the Arctic Red River over the past ~40 years. These results do not suggest that chemical weathering in the catchment does not exert an influence on pCO_2; rather, the results argue that

changes in chemical weathering have not yet modified the magnitude of that influence. In contrast, within the Yukon River catchment, changes in sulfide oxidation have been sufficient to reduce CO_2 drawdown even as the overall weathering system still acts to reduce atmospheric pCO_2. Within the Peel River catchment, weathering is essentially poised on the boundary between acting as a short-term CO_2 sink and acting as a short-term CO_2 source. While these results could be consistent with independent thaw-driven exposure of sulfide minerals, silicate minerals, and carbonate minerals to weathering agents, partially compensating variations among the weathering reactions hint at linkages and broader ecosystem effects. Even in systems where the effects of increased sulfide oxidation on pCO_2 are fully offset by changes in carbonate and silicate weathering, enhanced sulfide oxidation can still degrade local ecosystems through the release and downstream transport of sulfide-associated metals (Sullivan et al., 2025; Evinger et al., 2026).

A notable shortcoming of this work is that the calculations do not account for the oxidation of petrogenic organic carbon, which also modulates the chemical burden that thawing Arctic landscapes impose on the ocean-atmosphere system. The analysis also did not have access to isotopic observations of fluvial SO_4^{2-}. If available in the future, SO_4^{2-} $^{18}O/^{16}O$ and SO_4^{2-} $^{34}S/^{32}S$ measurements would improve the ability of the inversion model to distinguish among solutes derived from evaporite dissolution, meteoric inputs, and sulfide oxidation. In addition, the MEANDIR inversions merely explored a range of possible silicate $Si/\Sigma^{\pm}$ ratios rather than resolving clay formation or Si uptake into vegetation as independent end-members, and did not include K^+ in the calculations. Future research using Si or lithium isotope ratios may further constrain the nature of silicate weathering inputs and the quantity of Na^+-Ca^{2+}/Mg^{2+} exchange within Arctic catchments. Finally, the Mackenzie River results contain substantial noise (Fig. 7) due to interannual changes in discharge, meaning that the existence of a long-term trend may

become identifiable simply through additional observations. These limitations represent important sources of systematic uncertainty in the results, which are likely to change in the future as additional types of data or observations from future years are incorporated into the calculations.

Although the hypothesized positive feedback between permafrost thaw and inorganic mineral weathering seemingly has yet to materialize at the spatial scale of the Mackenzie River and the temporal scale of 40 years, at least as expressed within water samples collected from active river channels, it was seen in the Yukon River and Peel River. Furthermore, based on current $\Delta(ALK)/\Delta(FIC)$ trends, the inorganic chemical weathering system of the Yukon River is on track to transition from a net sink of CO_2 to a net source of CO_2 near the middle of the 21st century. While compensating increases in weathering magnitude before that transition are theoretically possible, the enhancements required to maintain constant impacts on pCO_2 will become increasingly large as $\Delta(ALK)/\Delta(FIC)$ ratios continue to decline.

7. Acknowledgements

This research was supported by the Endless Frontier Program at the Woods Hole Oceanographic Institution. Y. Hou provided helpful comments on an early draft of the manuscript, which was further improved by comments from two anonymous reviewers. Researchers at the U.S. Geological Survey and Environment and Climate Change Canada collected and analyzed the river water samples that underlie this work.

8. Author contributions

PCK: Conceptualization; Data curation; Formal analysis; Methodology; Software; Visualization; Writing - original draft; Writing - review and editing

9. Open research

No new measurements were collected for this study. Yukon River chemical observations were downloaded from the USGS Water Data for the Nation portal (https://waterdata.usgs.gov/download-samples/#dataProfile=site), and Yukon River discharge data were downloaded from the USGS National Water Information System portal (https://waterdata.usgs.gov/nwis/inventory/). Mackenzie River chemistry data were downloaded from ECCC Data Catalogue (https://data-donnees.az.ec.gc.ca/data/substances/monitor?lang=en) under the labels "National Long-term Water Quality Monitoring Data" and "Surface Water Quality, Oil Sands Region". Additional historical chemical observations were provided through direct email requests to the ECCC Water Quality Monitoring and Surveillance Division. Discharge data for the Mackenzie River sites were downloaded through the Canada Historical Hydrometric Data Search (https://wateroffice.ec.gc.ca/search/historical_e.html), the Real-Time Hydrometric Data Search (https://wateroffice.ec.gc.ca/search/real_time_e.html), and the Water Survey of Canada Unit Value index (https://collaboration.cmc.ec.gc.ca/cmc/hydrometrics/www/UnitValueData/). Additional chemical observations for the Yukon River and Mackenzie River were downloaded from the Arctic Great Rivers Observatory (https://arcticgreatrivers.org/water_data/). The MEANDIR model (v1.4) is archived with Zenodo (Kemeny, 2026; https://doi.org/10.5281/zenodo.22257975) and also available through GitHub (https://github.com/PrestonCosslettKemeny/MEANDIR). The major element data compilation, regression results, and derived geochemical fluxes are provided in the supplementary materials and, upon article acceptance, will be archived with Zenodo.

10. Conflict of interest statement

The author has no conflicts of interest to declare.

11. References

Alexandre, A., Meunier, J.D., Colin, F. and Koud, J.M., 1997. Plant impact on the biogeochemical cycle of silicon and related weathering processes. *Geochimica et cosmochimica acta*, 61(3), pp.677-682.

Archer, D., Kheshgi, H. and Maier-Reimer, E., 1997. Multiple timescales for neutralization of fossil fuel CO_2. *Geophysical Research Letters*, 24(4), pp.405-408.

Baronas, J.J., Torres, M.A., West, A.J., Rouxel, O., Georg, B., Bouchez, J., Gaillardet, J. and Hammond, D.E., 2018. Ge and Si isotope signatures in rivers: A quantitative multi-proxy approach. *Earth and Planetary Science Letters*, 503, pp.194-215.

Beaulieu, E., Goddéris, Y., Labat, D., Roelandt, C., Calmels, D. and Gaillardet, J., 2011. Modeling of water-rock interaction in the Mackenzie basin: Competition between sulfuric and carbonic acids. *Chemical Geology*, 289(1-2), pp.114-123.

Beaulieu, E., Goddéris, Y., Donnadieu, Y., Labat, D. and Roelandt, C., 2012. High sensitivity of the continental-weathering carbon dioxide sink to future climate change. *Nature Climate Change*, 2(5), pp.346-349.

Benettin, P., Bailey, S.W., Campbell, J.L., Green, M.B., Rinaldo, A., Likens, G.E., McGuire, K.J. and Botter, G., 2015. Linking water age and solute dynamics in streamflow at the Hubbard Brook Experimental Forest, NH, USA. *Water Resources Research*, 51(11), pp.9256-9272.

Biskaborn, B.K., Smith, S.L., Noetzli, J., Matthes, H., Vieira, G., Streletskiy, D.A., Schoeneich, P., Romanovsky, V.E., Lewkowicz, A.G., Abramov, A. and Allard, M., 2019. Permafrost is warming at a global scale. *Nature communications*, 10(1), p.264.

Brabets, T.P., Wang, B. and Meade, R.H., 2000. Environmental and hydrologic overview of the Yukon River Basin, Alaska and Canada. *Water-Resources Investigations Report*, 99, p.4204.

Bufe, A., Hovius, N., Emberson, R., Rugenstein, J.K., Galy, A., Hassenruck-Gudipati, H.J. and Chang, J.M., 2021. Co-variation of silicate, carbonate and sulfide weathering drives CO2 release with erosion. *Nature Geoscience*, 14(4), pp.211-216.

Burke, A., Present, T.M., Paris, G., Rae, E.C., Sandilands, B.H., Gaillardet, J., Peucker-Ehrenbrink, B., Fischer, W.W., McClelland, J.W., Spencer, R.G. and Voss, B.M., 2018. Sulfur isotopes in rivers: Insights into global weathering budgets, pyrite oxidation, and the modern sulfur cycle. *Earth and Planetary Science Letters*, 496, pp.168-177.

Calmels, D., Gaillardet, J., Brenot, A. and France-Lanord, C., 2007. Sustained sulfide oxidation by physical erosion processes in the Mackenzie River basin: Climatic perspectives. *Geology*, 35(11), pp.1003-1006.

Calmels, D., Galy, A., Hovius, N., Bickle, M., West, A.J., Chen, M.C. and Chapman, H., 2011. Contribution of deep groundwater to the weathering budget in a rapidly eroding mountain belt, Taiwan. *Earth and Planetary Science Letters*, 303(1-2), pp.48-58.

Cerling, T.E., Pederson, B.L. and Von Damm, K.L., 1989. Sodium-calcium ion exchange in the weathering of shales: Implications for global weathering budgets. *Geology*, 17(6), pp.552-554.

Cornelis, J.T., Delvaux, B., Georg, R.B., Lucas, Y., Ranger, J. and Opfergelt, S., 2011. Tracing the origin of dissolved silicon transferred from various soil-plant systems towards rivers: a review. *Biogeosciences*, 8(1), pp.89-112.

De La Rocha, C., Brzezinski, M.A. and DeNiro, M.J., 2000. A first look at the distribution of the stable isotopes of silicon in natural waters. *Geochimica et Cosmochimica Acta*, 64(14), pp.2467-2477.

Dean, J.F., Coxon, G., Zheng, Y., Bishop, J., Garnett, M.H., Bastviken, D., Galy, V., Spencer, R.G., Tank, S.E., Tipper, E.T. and Vonk, J.E., 2025. Old carbon routed from land to the atmosphere by global river systems. *Nature*, 642(8066), pp.105-111.

Dial, R.J., Hanna, C.T., Sullivan, P.F., Cooper, D.J., Tino, C.J., Gregory, D.D., Diamond, C., Rieser, M., Nicolsky, D.J., Hill, K. and Iwahana, G., 2026. Permafrost thaw controls iron flux from wetlands and sulfide-bearing rocks to Arctic rivers and streams. *Communications Earth & Environment*.

Ding, T., Wan, D., Wang, C. and Zhang, F., 2004. Silicon isotope compositions of dissolved silicon and suspended matter in the Yangtze River, China. *Geochimica et Cosmochimica Acta*

Douthitt, C.B., 1982. The geochemistry of the stable isotopes of silicon. *Geochimica et Cosmochimica Acta*, 46(8), pp.1449-1458.

Drake, T.W., Tank, S.E., Zhulidov, A.V., Holmes, R.M., Gurtovaya, T. and Spencer, R.G., 2018. Increasing alkalinity export from large Russian Arctic rivers. *Environmental science & technology*, 52(15), pp.8302-8308.

Duan, N., 1983. Smearing estimate: a nonparametric retransformation method. *Journal of the American Statistical Association*, 78(383), pp.605-610.

Evinger, T.G., O'Donnell, J.A., Carey, M.P., Koch, J.C., Baughman, C.A., Hill, K.R., Frei, R.J. and Poulin, B.A., 2026. Abrupt onset and persistent downstream effects of acid rock drainage on rivers across northwest Arctic Alaska. *AGU Advances*, 7(6), p.e2026AV002407.

Ferguson, R.I., 1986. River loads underestimated by rating curves. *Water resources research*, 22(1), pp.74-76.

Frey, K.E. and McClelland, J.W., 2009. Impacts of permafrost degradation on arctic river biogeochemistry. *Hydrological Processes: An International Journal*, 23(1), pp.169-182.

Frings, P.J., Clymans, W., Fontorbe, G., De La Rocha, C.L. and Conley, D.J., 2016. The continental Si cycle and its impact on the ocean Si isotope budget. *Chemical Geology*, 425, pp.12-36.

Gaillardet, J.D.B.L., Dupré, B., Louvat, P. and Allegre, C.J., 1999. Global silicate weathering and CO_2 consumption rates deduced from the chemistry of large rivers. *Chemical geology*, 159(1-4), pp.3-30.

Galy, A. and France-Lanord, C., 1999. Weathering processes in the Ganges–Brahmaputra basin and the riverine alkalinity budget. *Chemical Geology*, 159(1-4), pp.31-60.

Georg, R.B., Reynolds, B.C., Frank, M. and Halliday, A.N., 2006. Mechanisms controlling the silicon isotopic compositions of river waters. *Earth and Planetary Science Letters*, 249(3-4), pp.290-306.

Georg, R.B., Reynolds, B.C., West, A.J., Burton, K.W. and Halliday, A.N., 2007. Silicon isotope variations accompanying basalt weathering in Iceland. *Earth and Planetary Science Letters*, 261(3-4), pp.476-490.

Grant, K.E., Dellinger, M., Dickson, A.J., Ogric, M., Horan, K., Petsch, S. and Hilton, R.G., 2025. Validating the rhenium proxy for rock organic carbon oxidation using weathering profiles. *Chemical Geology*, 671, p.122464.

Hilton, R.G., Gaillardet, J., Calmels, D. and Birck, J.L., 2014. Geological respiration of a mountain belt revealed by the trace element rhenium. *Earth and Planetary Science Letters*, 403, pp.27-36.

Hilton, R.G. and West, A.J., 2020. Mountains, erosion and the carbon cycle. *Nature Reviews Earth & Environment*, 1(6), pp.284-299.

Hinkel, K.M. and Nelson, F.E., 2003. Spatial and temporal patterns of active layer thickness at Circumpolar Active Layer Monitoring (CALM) sites in northern Alaska, 1995–2000. *Journal of Geophysical Research: Atmospheres*, 108(D2).

Hirsch, R.M., Moyer, D.L. and Archfield, S.A., 2010. Weighted regressions on time, discharge, and season (WRTDS), with an application to Chesapeake Bay river inputs. JAWRA *Journal of the American Water Resources Association*, 46(5), pp.857-880.

Hinzman, L.D., Bettez, N.D., Bolton, W.R., Chapin, F.S., Dyurgerov, M.B., Fastie, C.L., Griffith, B., Hollister, R.D., Hope, A., Huntington, H.P. and Jensen, A.M., 2005. Evidence and implications of recent climate change in northern Alaska and other arctic regions. *Climatic Change*, 72(3), pp.251-298.

Keller, K., Blum, J.D. and Kling, G.W., 2007. Geochemistry of soils and streams on surfaces of varying ages in arctic Alaska. *Arctic, Antarctic, and Alpine Research*, 39(1), pp.84-98.

Keller, K., Blum, J.D. and Kling, G.W., 2010. Stream geochemistry as an indicator of increasing permafrost thaw depth in an arctic watershed. *Chemical Geology*, 273(1-2), pp.76-81.

Kemeny, P.C., Lopez, G.I., Dalleska, N.F., Torres, M., Burke, A., Bhatt, M.P., West, A.J., Hartmann, J. and Adkins, J.F., 2021. Sulfate sulfur isotopes and major ion chemistry reveal that pyrite oxidation counteracts CO_2 drawdown from silicate weathering in the Langtang-Trisuli-Narayani River system, Nepal Himalaya. *Geochimica et Cosmochimica Acta*, 294, pp.43-69.

Kemeny, P.C. and Torres, M.A., 2021. Presentation and applications of mixing elements and dissolved isotopes in rivers (MEANDIR), a customizable MATLAB model for Monte Carlo inversion of dissolved river chemistry. *American Journal of Science*, 321(5), pp.579-642.

Kemeny, P.C., Li, G.K., Douglas, M., Berelson, W., Chadwick, A.J., Dalleska, N.F., Lamb, M.P., Larsen, W., Magyar, J.S., Rollins, N.E. and Rowland, J., 2023. Arctic permafrost thawing enhances sulfide oxidation. *Global Biogeochemical Cycles*, 37(11), p.e2022GB007644.

Kemeny, P.C., Torres, M.A., Fischer, W.W. and Blättler, C.L., 2024. Balance and imbalance in biogeochemical cycles reflect the operation of closed, exchange, and open sets. *Proceedings of the National Academy of Sciences*, 121(12), p.e2316535121.

Kemeny, P.C. (2026) "MEANDIR v1.4". Zenodo. https://doi.org/10.5281/zenodo.22257975.

Kokelj, S.V., Lacelle, D., Lantz, T.C., Tunnicliffe, J., Malone, L., Clark, I.D. and Chin, K.S., 2013. Thawing of massive ground ice in mega slumps drives increases in stream sediment and solute flux across a range of watershed scales. *Journal of Geophysical Research: Earth Surface*, 118(2), pp.681-692.

Koven, C.D., Ringeval, B., Friedlingstein, P., Ciais, P., Cadule, P., Khvorostyanov, D., Krinner, G. and Tarnocai, C., 2011. Permafrost carbon-climate feedbacks accelerate global warming. *Proceedings of the National Academy of Sciences*, 108(36), pp.14769-14774.

Lafrenière, M.J. and Lamoureux, S.F., 2019. Effects of changing permafrost conditions on hydrological processes and fluvial fluxes. *Earth-science reviews*, 191, pp.212-223.

Lehn, G.O., Jacobson, A.D., Douglas, T.A., McClelland, J.W., Barker, A.J. and Khosh, M.S., 2017. Constraining seasonal active layer dynamics and chemical weathering reactions occurring in North Slope Alaskan watersheds with major ion and isotope ($\delta^{34}S_{SO4}$, $\delta^{13}C_{DIC}$, $^{87}Sr/^{86}Sr$, $\delta^{44/40}Ca$, and $\delta^{44/42}Ca$) measurements. *Geochimica et Cosmochimica Acta*, 217, pp.399-420.

Lewis, E.R. and Wallace, D.W.R., 1998. Program developed for CO_2 system calculations (No. cdiac: CDIAC-105). Environmental System Science Data Infrastructure for a Virtual Ecosystem (ESS-DIVE)(United States).

Lupker, M., France-Lanord, C., Galy, V., Lavé, J., Gaillardet, J., Gajurel, A.P., Guilmette, C., Rahman, M., Singh, S.K. and Sinha, R., 2012. Predominant floodplain over mountain weathering of Himalayan sediments (Ganga basin). *Geochimica et Cosmochimica Acta*, 84, pp.410-432.

Mast, M.A., 2013. Evaluation of stream chemistry trends in US Geological Survey reference watersheds, 1970–2010. *Environmental monitoring and assessmen*t, 185, pp.9343-9359.

Millot, R., Gaillardet, J., Dupré, B. and Allègre, C.J., 2002. The global control of silicate weathering rates and the coupling with physical erosion: new insights from rivers of the Canadian Shield. *Earth and Planetary Science Letters*, 196(1-2), pp.83-98.

Millot, R., Gaillardet, J., Dupré, B. and Allègre, C.J., 2003. Northern latitude chemical weathering rates: clues from the Mackenzie River Basin, Canada. *Geochimica et Cosmochimica Acta*, 67(7), pp.1305-1329.

Miner, K.R., Turetsky, M.R., Malina, E., Bartsch, A., Tamminen, J., McGuire, A.D., Fix, A., Sweeney, C., Elder, C.D. and Miller, C.E., 2022. Permafrost carbon emissions in a changing Arctic. *Nature Reviews Earth & Environment*, 3(1), pp.55-67.

Myers-Smith, I.H., Kerby, J.T., Phoenix, G.K., Bjerke, J.W., Epstein, H.E., Assmann, J.J., John, C., Andreu-Hayles, L., Angers-Blondin, S., Beck, P.S. and Berner, L.T., 2020. Complexity revealed in the greening of the Arctic. *Nature Climate Change*, 10(2), pp.106-117.

Négrel, P., Allègre, C.J., Dupré, B. and Lewin, E., 1993. Erosion sources determined by inversion of major and trace element ratios and strontium isotopic ratios in river water: the Congo Basin case. *Earth and Planetary Science Letters*, 120(1-2), pp.59-76.

Obu, J., Westermann, S., Bartsch, A., Berdnikov, N., Christiansen, H.H., Dashtseren, A., Delaloye, R., Elberling, B., Etzelmüller, B., Kholodov, A. and Khomutov, A., 2019. Northern Hemisphere permafrost map based on TTOP modelling for 2000–2016 at 1 km2 scale. *Earth-Science Reviews*, 193, pp.299-316.

O'Donnell, J.A., Carey, M.P., Koch, J.C., Baughman, C., Hill, K., Zimmerman, C.E., Sullivan, P.F., Dial, R., Lyons, T., Cooper, D.J. and Poulin, B.A., 2024. Metal mobilization from thawing permafrost to aquatic ecosystems is driving rusting of Arctic streams. *Communications Earth & Environment*, 5(1), p.268.

Sarmiento, J.L., 2013. Ocean biogeochemical dynamics. In *Ocean biogeochemical dynamics*. Princeton university press.

Schuur, E.A., McGuire, A.D., Schädel, C., Grosse, G., Harden, J.W., Hayes, D.J., Hugelius, G., Koven, C.D., Kuhry, P., Lawrence, D.M. and Natali, S.M., 2015. Climate change and the permafrost carbon feedback. *Nature*, 520(7546), pp.171-179.

Skierszkan, E.K., Szeitz, A.J., Lindsay, M.B. and Carey, S.K., 2026. Abrupt stream acidification and metal mobilization from permafrost degradation. *Science*, 392(6800), pp.863-867.

Spence, J. and Telmer, K., 2005. The role of sulfur in chemical weathering and atmospheric CO_2 fluxes: evidence from major ions, $\delta^{13}C_{DIC}$, and $\delta^{34}S_{SO4}$ in rivers of the Canadian Cordillera. *Geochimica et Cosmochimica Acta*, 69(23), pp.5441-5458.

Striegl, R.G., Aiken, G.R., Dornblaser, M.M., Raymond, P.A. and Wickland, K.P., 2005. A decrease in discharge-normalized DOC export by the Yukon River during summer through autumn. *Geophysical Research Letters*, 32(21).

Sullivan, P.F., Dial, R.J., Cooper, D.J., Diamond, C., Tino, C.J., Gregory, D.D., Wong, R.E. and Lyons, T.W., 2025. Wild, scenic, and toxic: Recent degradation of an iconic Arctic watershed with permafrost thaw. *Proceedings of the National Academy of Sciences*, 122(37), p.e2425644122.

Tank, S.E., Raymond, P.A., Striegl, R.G., McClelland, J.W., Holmes, R.M., Fiske, G.J. and Peterson, B.J., 2012. A land-to-ocean perspective on the magnitude, source and implication of DIC flux from major Arctic rivers to the Arctic Ocean. *Global Biogeochemical Cycles*, 26(4).

Tank, S.E., Striegl, R.G., McClelland, J.W. and Kokelj, S.V., 2016. Multi-decadal increases in dissolved organic carbon and alkalinity flux from the Mackenzie drainage basin to the Arctic Ocean. *Environmental Research Letters*, 11(5), p.054015.

Tank, S.E., McClelland, J.W., Spencer, R.G., Shiklomanov, A.I., Suslova, A., Moatar, F., Amon, R.M., Cooper, L.W., Elias, G., Gordeev, V.V. and Guay, C., 2023. Recent trends in the chemistry of major northern rivers signal widespread Arctic change. *Nature Geoscience*, 16(9), pp.789-796.

Tipper, E.T., Bickle, M.J., Galy, A., West, A.J., Pomiès, C. and Chapman, H.J., 2006. The short term climatic sensitivity of carbonate and silicate weathering fluxes: insight from seasonal variations in river chemistry. *Geochimica et Cosmochimica Acta*, 70(11), pp.2737-2754.

Tipper, E.T., Stevenson, E.I., Alcock, V., Knight, A.C., Baronas, J.J., Hilton, R.G., Bickle, M.J., Larkin, C.S., Feng, L., Relph, K.E. and Hughes, G., 2021. Global silicate weathering flux overestimated because of sediment–water cation exchange. *Proceedings of the National Academy of Sciences*, 118(1), p.e2016430118.

Arctic Great Rivers Observatory. 2026. Water Quality Dataset, Version 20260601. https://www.arcticgreatrivers.org/data.

Torres, M.A., West, A.J. and Li, G., 2014. Sulphide oxidation and carbonate dissolution as a source of CO_2 over geological timescales. *Nature*, 507(7492), pp.346-349.

Torres, M.A., West, A.J., Clark, K.E., Paris, G., Bouchez, J., Ponton, C., Feakins, S.J., Galy, V. and Adkins, J.F., 2016. The acid and alkalinity budgets of weathering in the Andes–Amazon system: Insights into the erosional control of global biogeochemical cycles. *Earth and Planetary Science Letters*, 450, pp.381-391.

Torres, M.A. and Baronas, J.J., 2021. Modulation of riverine concentration-discharge relationships by changes in the shape of the water transit time distribution. *Global Biogeochemical Cycles*, 35(1), p.e2020GB006694.

Toohey, R.C., Herman-Mercer, N.M., Schuster, P.F., Mutter, E.A. and Koch, J.C., 2016. Multidecadal increases in the Yukon River Basin of chemical fluxes as indicators of changing flowpaths, groundwater, and permafrost. *Geophysical Research Letters*, 43(23), pp.12-120.

Tukey, J.W., 1977. Exploratory data analysis (Vol. 2, pp. 131-160). Reading, MA: Addison-wesley.

Vonk, J.E., Fritz, M., Speetjens, N.J., Babin, M., Bartsch, A., Basso, L.S., Bröder, L., Göckede, M., Gustafsson, Ö., Hugelius, G. and Irrgang, A.M., 2025. The land–ocean Arctic carbon cycle. *Nature Reviews Earth & Environment*, 6(2), pp.86-105.

Walsh, E.V., Hilton, R.G., Tank, S.E. and Amos, E., 2024. Temperature sensitivity of the mineral permafrost feedback at the continental scale. *Science Advances*, 10(41), p.eadq4893.

Walvoord, M.A. and Striegl, R.G., 2007. Increased groundwater to stream discharge from permafrost thawing in the Yukon River basin: Potential impacts on lateral export of carbon and nitrogen. *Geophysical Research Letters*, 34(12).

Walvoord, M.A. and Kurylyk, B.L., 2016. Hydrologic impacts of thawing permafrost—A review. *Vadose Zone Journal*, 15(6), pp.vzj2016-01.

Yue, S., Pilon, P., Phinney, B. and Cavadias, G., 2002. The influence of autocorrelation on the ability to detect trend in hydrological series. *Hydrological processes*, 16(9), pp.1807-1829.

Zeebe, R.E. and Wolf-Gladrow, D., 2001. CO_2 in seawater: equilibrium, kinetics, isotopes (Vol. 65). Gulf Professional Publishing.

Zhang, L., Bufe, A., Dean, J.F., Rocher-Ros, G., Sponseller, R.A., Stanley, E.H., Karlsson, J., Butman, D.E., Liu, R., Hou, L. and Ding, J., 2026. Rock weathering can counteract river CO_2 emissions induced by permafrost thaw. *Nature*, 655(8121), pp.125-132.

Zolkos, S., Tank, S.E. and Kokelj, S.V., 2018. Mineral weathering and the permafrost carbon-climate feedback. *Geophysical Research Letters*, 45(18), pp.9623-9632.

Zolkos, S. and Tank, S.E., 2020. Experimental evidence that permafrost thaw history and mineral composition shape abiotic carbon cycling in thermokarst-affected stream networks. *Frontiers in Earth Science*, 8, p.152.

Zondervan, J.R., Hilton, R.G., Dellinger, M., Clubb, F.J., Roylands, T. and Ogrič, M., 2023. Rock organic carbon oxidation CO_2 release offsets silicate weathering sink. *Nature*, 623(7986), pp.329-333.

12. Tables and figures

Table 1: Variables used throughout the text.

Variable	Description
ALK	Alkalinity in the global ocean
$\Delta(ALK)$	The change in ocean alkalinity due to a chemical weathering system
$\Delta(ALK)_{norm}$	$\Delta(ALK)$ normalized to a specific initial condition
$\delta(ALK)$	The change in $\Delta(ALK)$ due to change in a chemical weathering system
FIC	Fluid Inorganic Carbon in the ocean-atmosphere system (ocean DIC inventory plus atmospheric CO_2 inventory) Neither silicate weathering nor sulfide oxidation directly modifies FIC
$\Delta(FIC)$	The change in FIC due to a chemical weathering system.
$\Delta(FIC)_{norm}$	$\Delta(FIC)$ normalized to a specific initial condition
$\Delta(FIC)_{norm}^{intercept}$	y-intercept of the pCO_2 contour associated with a normalized vector
$\delta(FIC)$	The change in $\Delta(FIC)$ due to change in a chemical weathering system
R	Magnitude of the chemical weathering vector: $R^2 = \Delta(ALK)^2 + \Delta(FIC)^2$
r	R normalized to a specific initial condition: $r = R/R_{inital}$
ϕ	The angle of the chemical weathering vector: $\phi = \tan^{-1}(\Delta(FIC)/\Delta(ALK))$
$m_{contour}$	The slope of pCO_2 contours in the space of $\Delta(FIC)$ against $\Delta(ALK)$
γ	The number of pCO_2 contours crossed by a chemical weathering vector. The convention in this work is that γ ranges from -1 to 1 on the unit circle $\gamma > 0$: chemical weathering acts to increase pCO_2 $\gamma < 0$: chemical weathering acts to decrease pCO_2
λ	The fractional change in the number of pCO_2 contours crossed by a chemical weathering vector: $\lambda = \gamma/\gamma_{initial}-1$ $\lambda > 0$: The weathering system has enhanced the initial sense of change. Because most γ are < 0 in this article, $\lambda > 0$ generally means that weathering has increased CO_2 drawdown relative to the initial condition. $\lambda < 0$: The weathering system has reduced the initial sense of change. Because most γ are < 0 in this article, $\lambda < 0$ generally means that weathering has reduced CO_2 drawdown relative to the initial condition.

Table 2: Site names, codes, and station identifiers for chemistry and discharge observations.

Site name	Code	Chemistry site	Discharge site
Yukon River at Pilot Station	YP-01	15565447	15565447
Peel River above Fort McPherson	PL-01	NW10MC0001	10MC002
Mackenzie River above Arctic Red River	MR-02	NW10LA0003	10LC014
Mackenzie River at Norman Wells	MR-03	NW10KA0001	10KA001
Mackenzie River at Strong Point	MR-04	NW10FB0006	10FB006
Great Bear River at lake outlet	GR-05	NW10JC0001	10JC003
Lockhart River at Artillery Lake outlet	LR-06	NW07RD0001	07RD001
South Nahanni above Virginia Falls	SN-12	NW10EB0016	10EB001
Flat River near mouth	FR-15	NW10EA0004	10EA003
Liard River at Fort Liard	LR-17	NW10ED0001	10ED001
Liard River near mouth	LR-18	NW10ED0002	10ED002
Hay River near Alberta/NWT border	HR-19	NW07OB0002	07OB001
Slave River at Fitzgerald	SR-20	AL07NB0001	07NB001
Peace River at Peace Point	PR-21	AL07KC0001	07KC001
Athabasca River at highway #16	AR-23	AL07AA0023	07AA002

Table 3: End-member chemical ratios used in the MEANDIR inversions. Ratios are normalized by the charge-equivalent sum of Ca^{2+}, Mg^{2+}, Na^{+}, and SO_4^{2-} and are given as normal distributions (mean ± one standard deviation). The evaporite end-member was constrained to be a stoichiometric combination of gypsum/epsomite and halite (Kemeny and Torres, 2021). End-member uncertainty was included in the inversion calculations. The Ca^{2+} and Mg^{2+} ratios of the Ca^{2+}/Mg^{2+} exchange end-member were set to match the relative abundance of Ca^{2+} and Mg^{2+} within each sample. The updated sampling algorithm implemented in MEANDIR v1.4 removed the need for one chemical ratio within each end-member to be calculated from the other ratios.

End-member chemical distributions used in MEANDIR inversions			
End-members	$Ca^{2+}/\Sigma^{\pm}$	$Mg^{2+}/\Sigma^{\pm}$	$Na^{+}/\Sigma^{\pm}$
Carbonate weathering	0.660 ± 0.084	0.340 ± 0.084	0 ± 0
Silicate weathering	0.312 ± 0.085	0.224 ± 0.075	0.464 ± 0.070
Evaporite dissolution	0.278 ± 0.072	0.063 ± 0.030	0.318 ± 0.104
Meteoric precipitation	0.033 ± 0.007	0.159 ± 0.006	0.721 ± 0.009
Sulfide oxidation	0 ± 0	0 ± 0	0 ± 0
Na^{+} exchange	0 ± 0	0 ± 0	1 ± 0
Ca^{2+}/Mg^{2+} exchange	calculated	calculated	0 ± 0
End-members	$SO_4^{2-}/\Sigma^{\pm}$	$Cl^{-}/\Sigma^{\pm}$	$Si/\Sigma^{\pm}$
Carbonate weathering	0 ± 0	0 ± 0	0 ± 0
Silicate weathering	0 ± 0	0 ± 0	variable (see text)
Evaporite dissolution	0.341 ± 0.052	0.318 ± 0.104	0 ± 0
Meteoric precipitation	0.087 ± 0.007	0.830 ± 0.038	0 ± 0
Sulfide oxidation	1 ± 0	0 ± 0	0 ± 0
Na^{+} exchange	0 ± 0	0 ± 0	0 ± 0
Ca^{2+}/Mg^{2+} exchange	0 ± 0	0 ± 0	0 ± 0

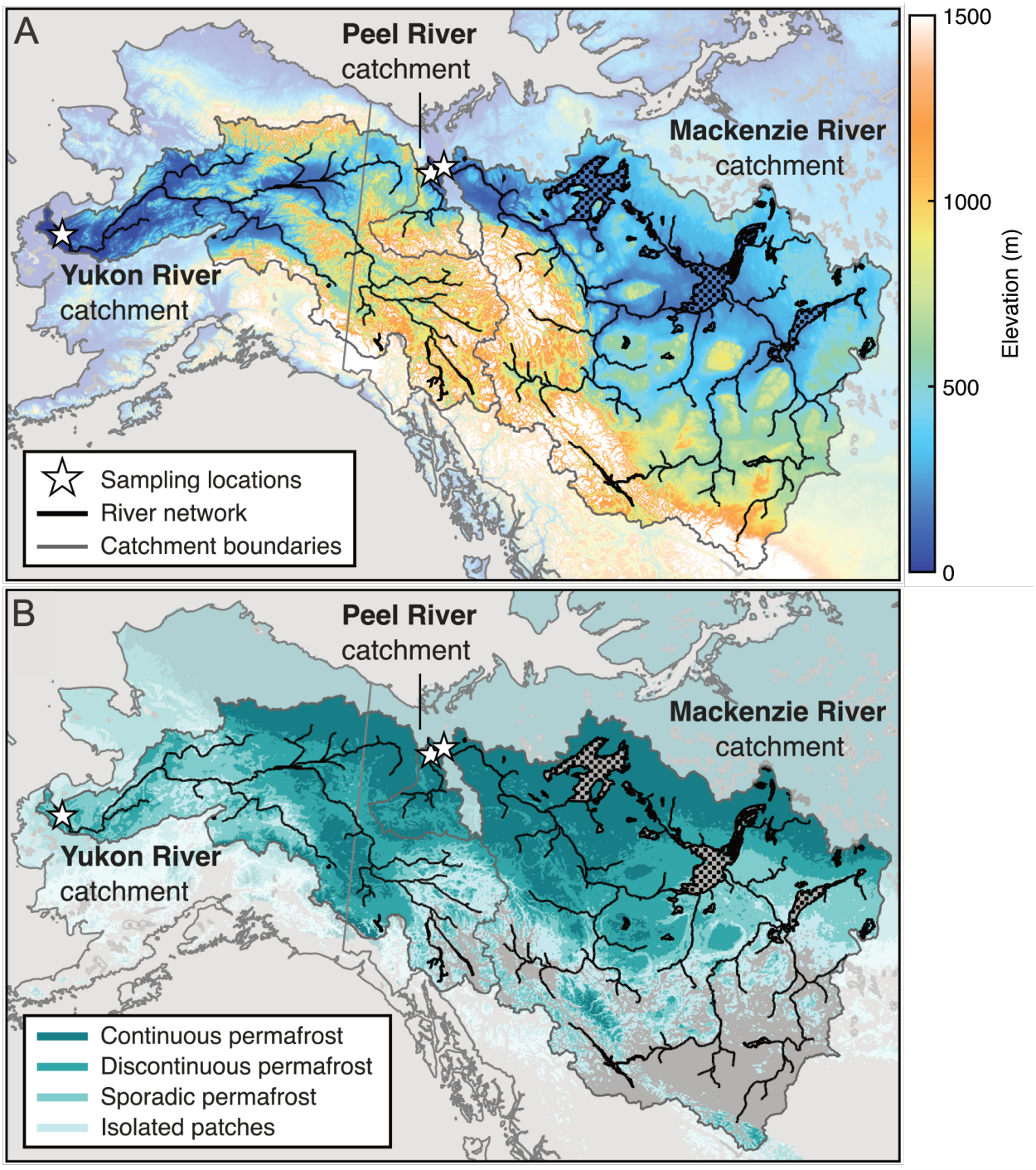


Fig. 1: River networks (black lines), catchment boundaries (grey lines), lakes (stippling), and sampling locations (stars) for the Yukon River at Pilot Station, Peel River above Fort McPherson, and Mackenzie River above the Arctic Red River in Alaska and Canada. The three catchments span a wide range of (**A**) elevations and have (**B**) permafrost abundances from continuous to absent. Elevation data are GTOPO30, permafrost zones are from Obu et al. (2019), and the maps are projected in EPSG:3413.

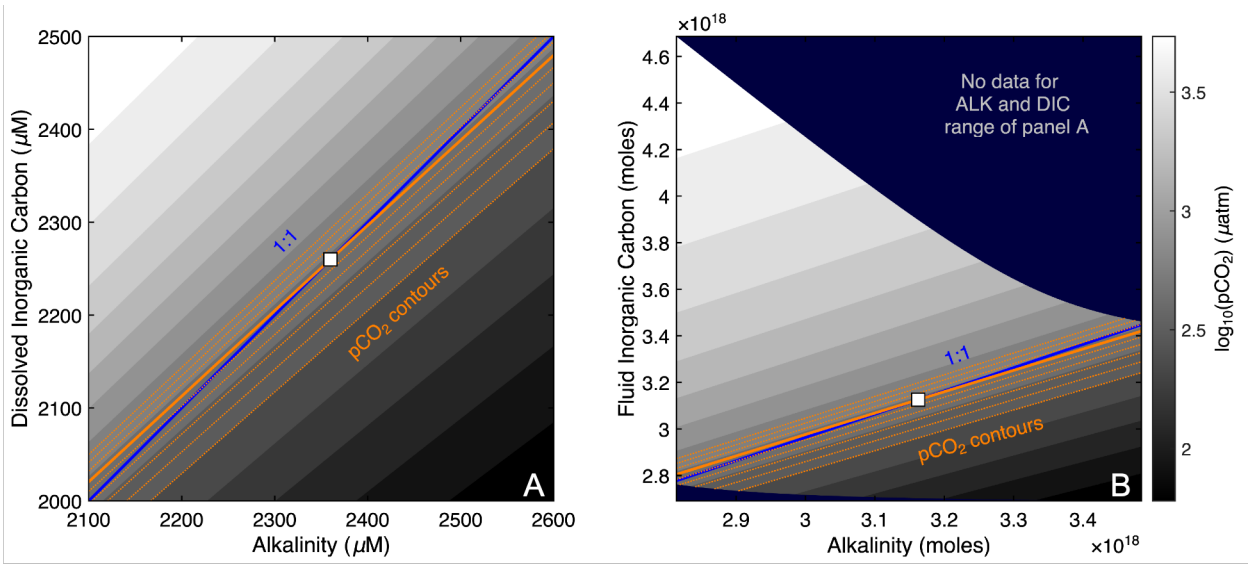


Fig. 2: Partial pressure of atmospheric carbon dioxide (pCO_2) as a function of (**A**) marine ALK and DIC concentrations or (**B**) ocean-atmosphere inventories of ALK and Fluid Inorganic Carbon (FIC), the latter being equal to the sum of DIC and atmospheric CO_2. Near modern conditions (white squares), pCO_2 contours between 300 µatm and 700 µatm (dotted orange lines) have slope values ranging from 0.87 to 0.93; these values are the same when calculated using ALK and DIC or when calculated using ALK and FIC. This work approximated pCO_2 contours near modern conditions as being parallel, with a slope of 0.92, corresponding to the contour that passes through modern conditions (solid orange line). A 1:1 line is plotted for reference (solid blue line). Calculations were performed in CO2SYS (Lewis and Wallace, 1998) and the calculation of ocean-atmosphere FIC from marine DIC and pCO_2 employed the ocean volume and number of moles in the atmosphere from Sarmiento (2013).

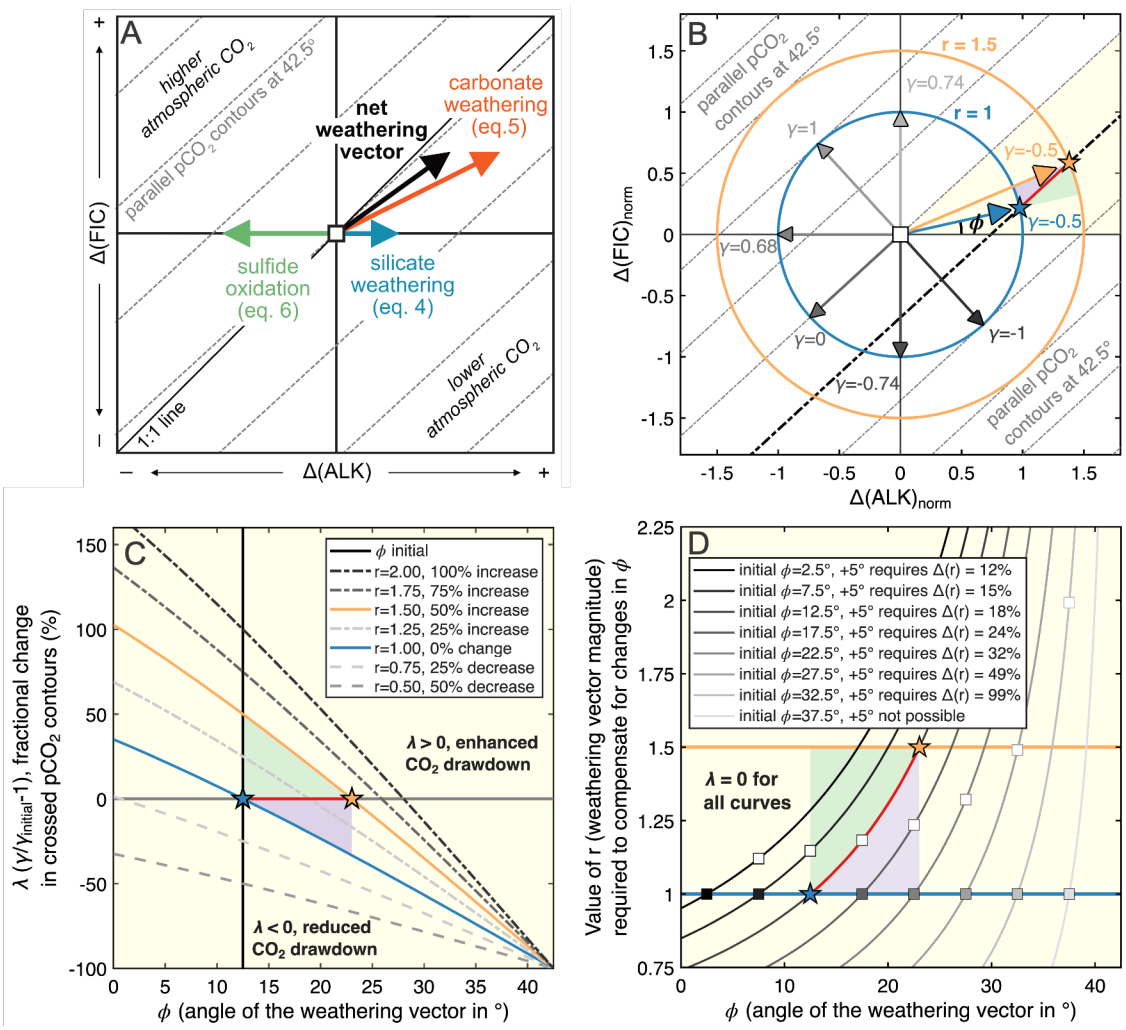


Fig. 3: Polar framework for quantifying the impact of changing weathering reactions on pCO_2. (**A**) Δ(ALK) and Δ(FIC) fluxes resulting from silicate weathering, carbonate weathering, and sulfide oxidation. The net weathering vector is the sum of the individual weathering vectors (Fig. S16). The lengths of the plotted arrows are for visual clarity only and are not scaled to observations. (**B**) The Δ(ALK) and Δ(FIC) fluxes resulting from weathering reactions can be recast as a normalized vector with magnitude r and angle ϕ relative to the positive $\Delta(ALK)_{norm}$ axis. This normalized weathering vector crosses γ contours, where γ is defined to equal 1 at r = 1 and ϕ = 132.5° (for the modern ocean-atmosphere system with $m_{contour}$ = 0.92). Most chemical weathering systems have ϕ values between 0° and 42.5° (yellow shading), corresponding to weathering that decreases pCO_2. An example of weathering system evolution is given for the change from an initial condition (blue) to a final state (orange) characterized by 50% higher weathering magnitude and lower Δ(ALK)/Δ(FIC) ratio but no change in the impact of weathering on pCO_2. For a given increase in r, ϕ values exist that are greater than the initial angle but result in enhanced CO_2 drawdown (green shading). In contrast, smaller increases in r with increases in ϕ can result in reductions to CO_2 drawdown (purple shading). (**C**) λ, the fractional change in γ values, against ϕ for an initial condition with ϕ = 12.5° and r = 1. Values of ϕ can become larger as r increases without resulting in λ < 0 and reduced CO_2 drawdown. (**D**) The change in r required to accommodate a given change in ϕ (+5°, in this case) is larger at higher initial ϕ, indicating that weathering magnitude has a diminishing ability to prevent changes to pCO_2 at lower values of Δ(ALK)/Δ(FIC).

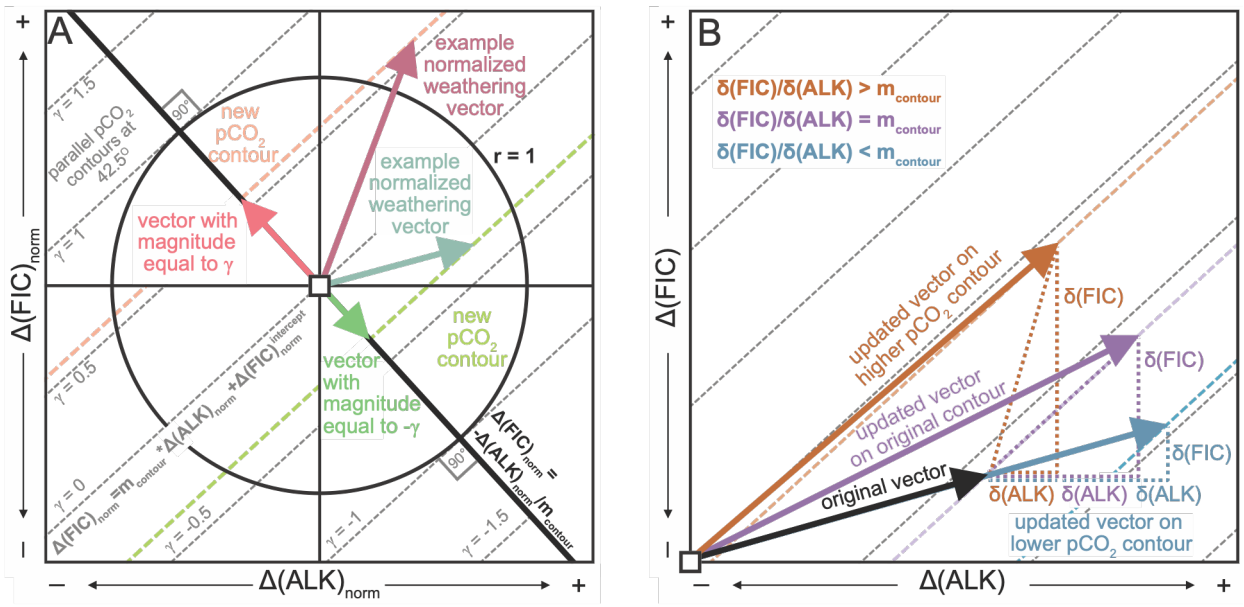


Fig. 4: Schematic of calculations in the polar coordinate space. (**A**) Example of calculating γ for two weathering vectors (magenta and teal). The absolute value of γ for each weathering system is the magnitude of the vector (coral pink and light green) that begins at the origin and ends at the intersection of the line $\Delta(FIC)_{norm} = -\Delta(ALK)_{norm}/m_{contour}$ (thick black line) with the pCO_2 contour passing through the tip of the normalized weathering vector (orange and lime green dashed lines). (**B**) δ(ALK) and δ(FIC) quantify the change in Δ(ALK) and Δ(FIC) through time. The ratio δ(FIC)/δ(ALK) relative to the slope of pCO_2 contours determines whether a shift in chemical weathering moves the weathering system to a pCO_2 contour that is higher (orange), the same (purple), or lower (blue) than the initial condition.

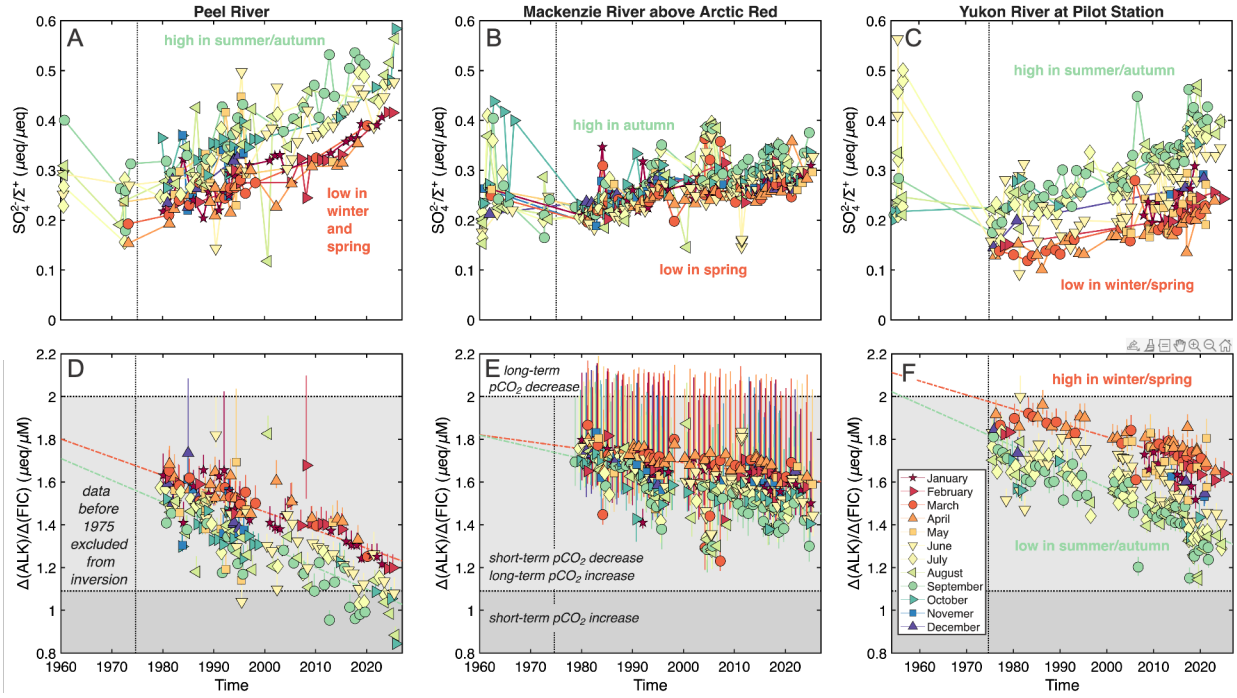


Fig. 5: Chemical observations and inversion results. (**A-C**) The ratio of SO_4^{2-} to the sum of cations ($\Sigma^+ = Ca^{2+} + Mg^{2+} + Na^+$, in units of charge equivalents) has been increasing in the Peel River, Mackenzie River, and the Yukon River since approximately 1975-1980. Furthermore, all sites show seasonality in the observed ratio. Increases in the absolute flux of Σ^+ through time have exceeded increases in the absolute flux of SO_4^{2-}. (**D-F**) MEANDIR results demonstrate that weathering Δ(ALK)/Δ(FIC) generally falls between 1.09 and 2, corresponding to short-term pCO_2 decline. The ratio varies seasonally but has been decreasing over the observational record. For the Peel River, recent summertime samples represent weathering systems that act as short-term CO_2 sources. Samples collected before 1975 are included in panels (**A-C**) but were excluded from the inversion analysis due to substantial noise in the early portions of the records and the potential for changes through time in the underlying analytical methods (Mast, 2013). Plotted results in (**D-F**) are the medians and 5^{th}-95^{th} percentiles of successful simulations for an inversion with silicate $Si/\Sigma^{\pm}$ equal to 0.5 ± 0.25. Higher values of silicate $Si/\Sigma^{\pm}$ would generally result in elevated values for the fraction of carbonate mineral weathering and lower weathering Δ(ALK)/Δ(FIC) ratios.

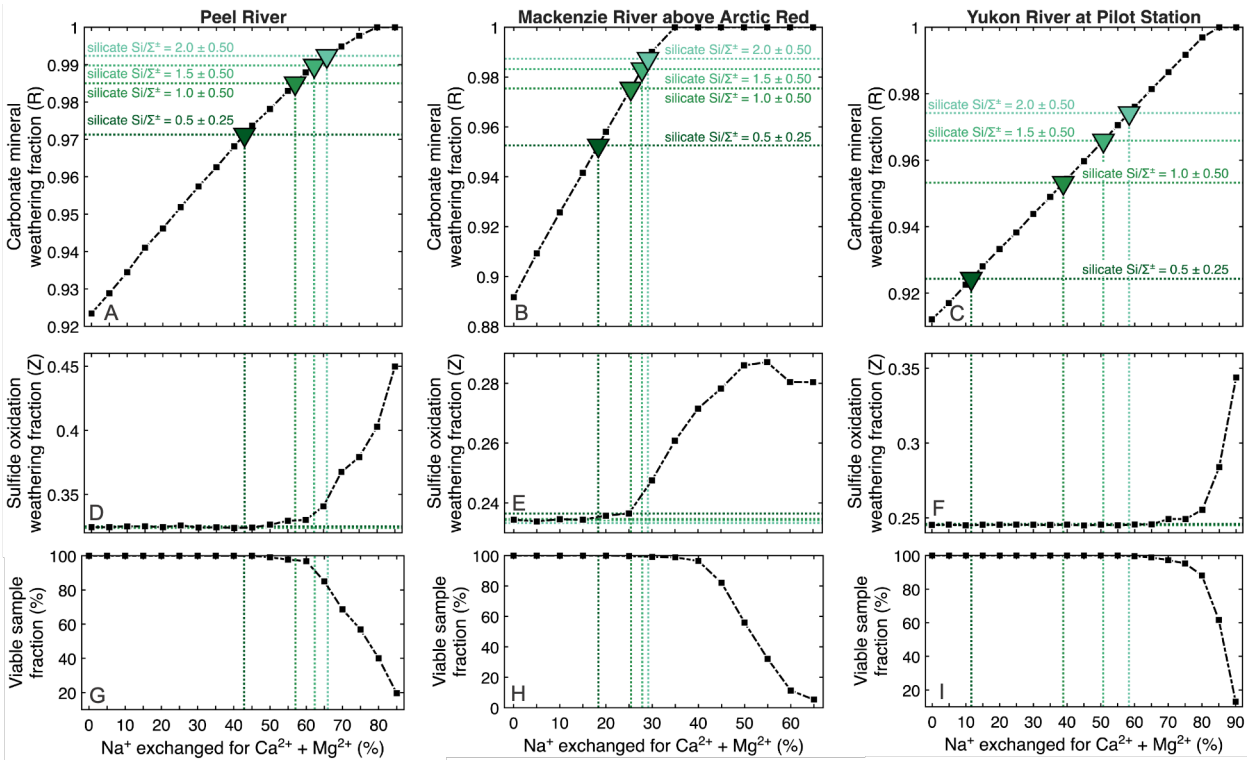


Fig. 6: The role of silicate $Si/\Sigma^{\pm}$ in inverting fluvial observations from the (**A, D, G**) Peel River, (**B, E, H**) Mackenzie River, and (**C, F, I**) Yukon River. The plotted black points indicate the mean inversion-constrained carbonate weathering fraction (R), sulfide oxidation weathering fraction (Z), and viable sample fraction when the specified fraction of observed Na^+ was manually converted into Ca^{2+} and Mg^{2+} prior to the inversion calculation (the inversions in these cases did not include Si or exchange end-members). Higher fractions of carbonate mineral weathering and sulfide oxidation weathering were recovered when higher fractions of fluvial Na^+ were exchanged for Ca^{2+} and Mg^{2+}. The horizontal green lines indicate the average carbonate weathering fraction and sulfide oxidation weathering fraction for four inversions including Si and exchange end-members where silicate $Si/\Sigma^{\pm}$ was equal to 0.5 ± 0.25, 1.0 ± 0.5, 1.5 ± 0.5, or 2.0 ± 0.5.

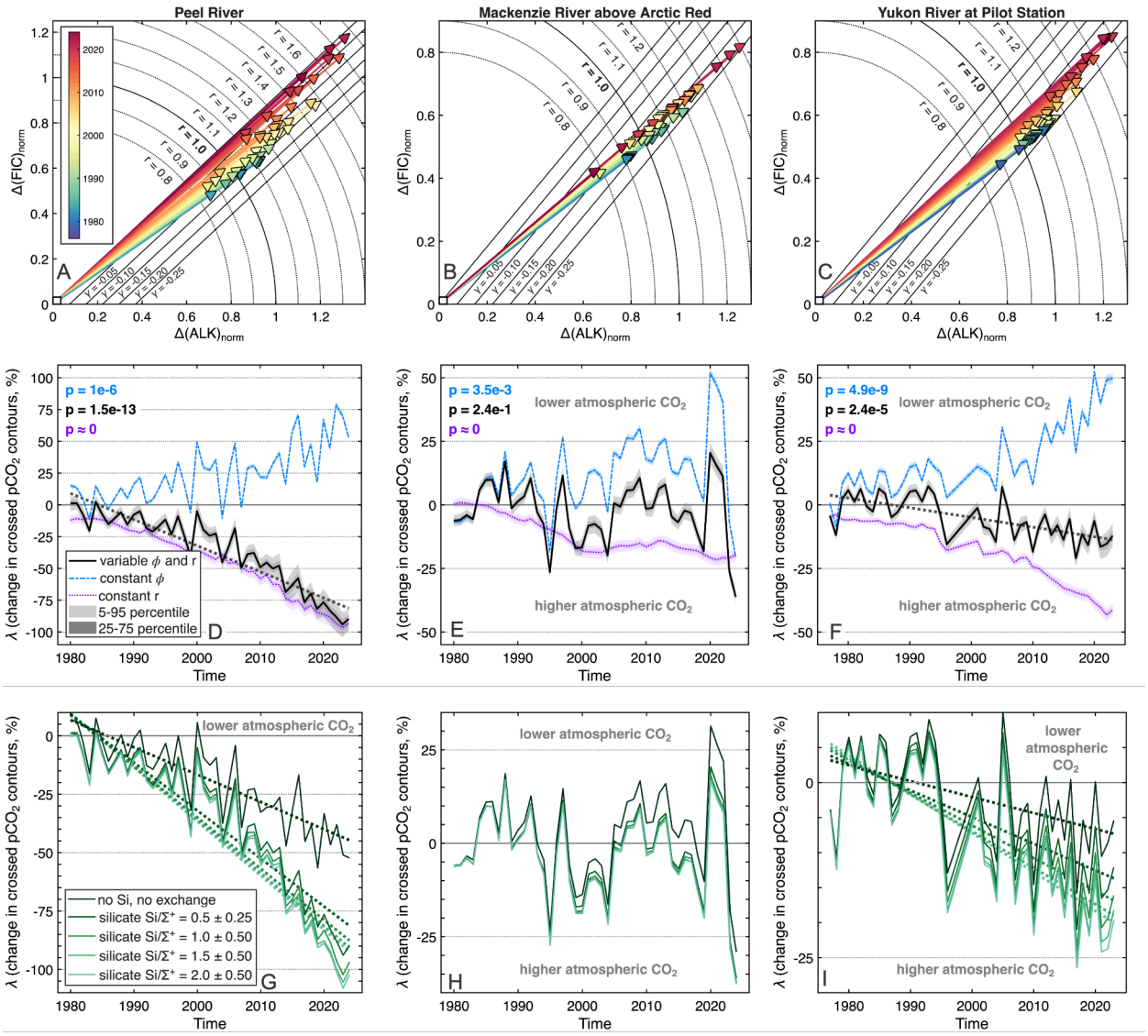


Fig. 7: Annual chemical weathering vectors and changes in the impact of weathering on pCO_2 for the Peel River, Mackenzie River, and Yukon River. (**A-C**) Annual weathering vectors with γ and r contours (see Fig. S16 for deconvolution of net weathering vectors into the contributions from carbonate weathering, silicate weathering, and sulfide oxidation). For the Peel River and the Yukon River, weathering vectors both lengthen and rotate to higher angles (lower Δ(ALK)/Δ(FIC) ratios) when moving toward the present. (**D-F**) λ values quantify the fractional change in crossed pCO_2 contours through time. Drawdown of CO_2 due to inorganic chemical weathering has declined significantly in the Peel River and Yukon River while remaining statistically invariant in the Mackenzie River. Calculations that ignore the changing magnitude of weathering (purple curves) or the changing Δ(ALK)/Δ(FIC) ratio of weathering (blue curves) reach statistically significant trends in opposite directions. Shading indicates the 5^{th}-95^{th} and 25^{th}-75^{th} percentiles of results. Results in (**A-F**) are for inversion scenarios where the silicate end-member has $Si/\Sigma^{\pm} = 0.5 \pm 0.25$. (**G-I**) The estimated trend in λ depends on the inversion silicate $Si/\Sigma^{\pm}$ distribution. However, changing the $Si/\Sigma^{\pm}$ ratio, or even fully removing Si and the exchange end-members from the inversion calculations, does not modify whether the trends are significant.

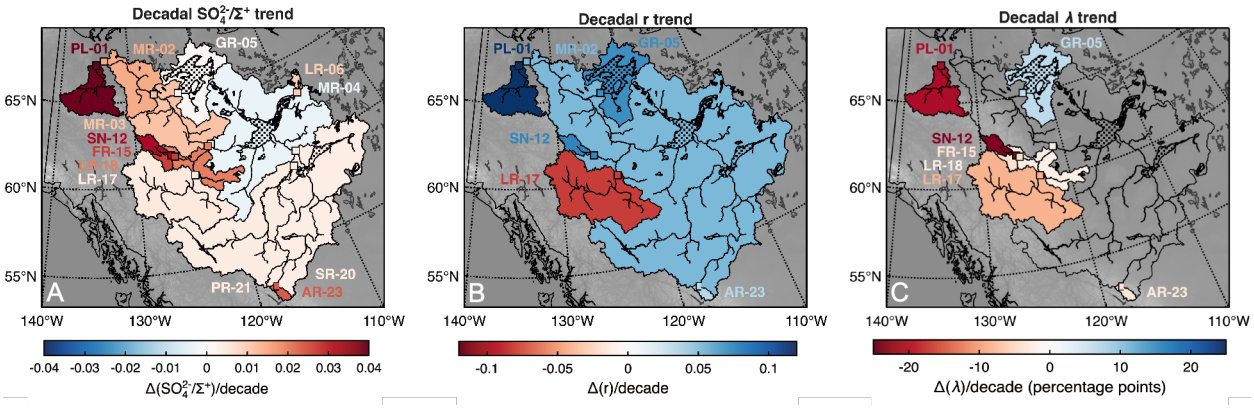


Fig. 8: Mackenzie River mainstem and subcatchments with significant trends in (**A**) SO_4^{2-}/Σ^+, (**B**) r, and (**C**) λ. Across sites, changes to the impact of weathering on pCO_2 due to increasing sulfide oxidation have been partially or fully nullified by increases in weathering magnitude. The Peel River (PL-01), the South Nahanni River (SN-12), the Flat River (FR-15), the Liard River (LR-17, LR-18), and the Athabasca River (AR-23) have all experienced a significant reduction in weathering-associated CO_2 drawdown. In contrast, CO_2 drawdown due to chemical weathering has increased in the Great Bear River catchment (GR-05). Plotted results are for inversion calculations with silicate $Si/\Sigma^{\pm} = 0.5 \pm 0.25$ (see Fig. S43 for results with silicate $Si/\Sigma^{\pm} = 1.0 \pm 0.5$). Plotted values are Theil-Sen slopes calculated from annual data medians, scaled to decades, when $p < 0.05$ for the Mann-Kendall test. Sampling points are indicated as squares, river networks and catchment boundaries are in black, and lakes are stippled. Maps are projected in EPSG:3413.

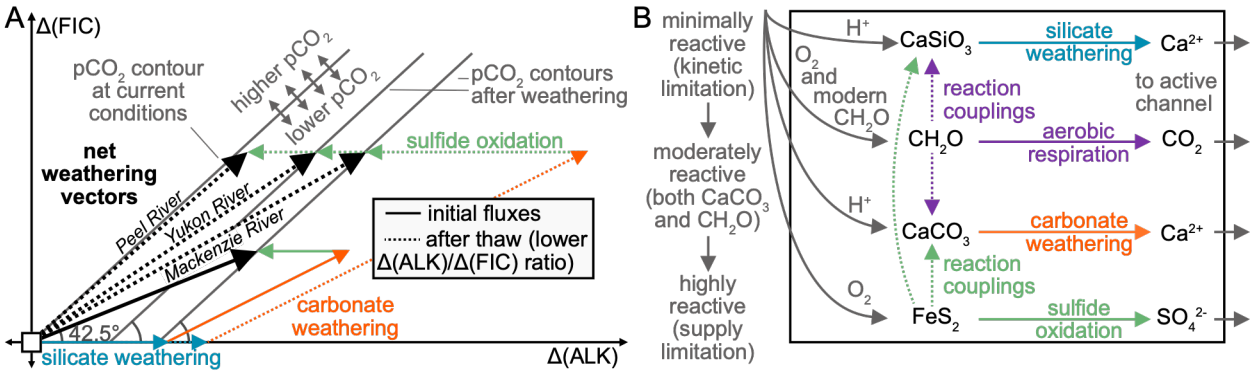


Fig. 9: Schematic of chemical weathering changes since 1975-1980. (**A**) Changes in the magnitude of silicate weathering, carbonate weathering, and sulfide oxidation have caused net weathering vectors to shift along the same pCO_2 contour (as in the Mackenzie River), towards a moderately higher pCO_2 contour (as in the Yukon River), or towards a much higher pCO_2 contour that approaches the initial pCO_2 contour without weathering (as in the Peel River). The lengths of the plotted arrows are for visual clarity only and are not scaled to observations. Oxidation of petrogenic organic carbon would be represented by an additional vector with $\Delta(FIC) > 0$ and $\Delta(ALK) = 0$. (**B**) Weathering reactions are enhanced through thaw-driven exposure of previously frozen sediment to acid (H^+) and oxidants (generally O_2). In addition, reaction couplings between sulfide oxidation or the oxidation of modern or petrogenic organic carbon with carbonate or silicate weathering may increase chemical weathering fluxes. Kinetically-limited reactions might also be enhanced through increases in temperature or the mean residence time of subsurface fluids.

Supplementary information: Contour-crossing calculations quantify decadal changes in the pCO_2 impacts of inorganic chemical weathering in the North American Arctic

Preston Cosslett Kemeny[a*]

[a] Department of Marine Chemistry and Geochemistry, Woods Hole Oceanographic Institution, Woods Hole, MA, USA

[*]**Corresponding author**: Preston Cosslett Kemeny
Woods Hole Oceanographic Institution, 266 Woods Hole Road, Woods Hole, MA 02543
(preston.kemeny@whoi.edu, preston.kemeny@gmail.com)

Supplementary tables

Table S1: Regression uncertainty for each dissolved element and site 3

Supplementary figures

Fig. S1: Ternary diagrams of Ca^{2+} – Mg^{2+} – Na^+ and SO_4^{2-} – Cl^- – HCO_3^- 4
Fig. S2: Mixing plots: $SO_4^{2-}/\Sigma^{\pm}$ vs. $Ca^{2+}/\Sigma^{\pm}$, Mg^{2+}/Na^+ vs. Ca^{2+}/Na^+, Na^+/Cl^- vs. Ca^{2+}/Cl^- 5
Fig. S3: Comparison of observations and regression results for the Peel River 6
Fig. S4: Comparison of observations and regression results for the Mackenzie River 7
Fig. S5: Comparison of observations and regression results for the Yukon River 8
Fig. S6: Flux comparison with Tank et al. (2016), Toohey et al. (2016), and Zolkos et al. (2018) ... 9
Fig. S7: Cross plot of annual and observed SO_4^{2-} and Σ^+ 10
Fig. S8: Mean and median inversion results for the Peel River 11
Fig. S9: Mean and median inversion results for the Mackenzie River 12
Fig. S10: Mean and median inversion results for the Yukon River 13
Fig. S11: Sulfide oxidation weathering fraction against carbonate mineral weathering fraction 14
Fig. S12: Change in carbonate weathering fraction as Ca^{2+} and Mg^{2+} are exchanged for Na^+ 15
Fig. S13: Change in sulfide oxidation fraction as Ca^{2+} and Mg^{2+} are exchanged for Na^+ 16
Fig. S14: Change in viable sample fraction as Ca^{2+} and Mg^{2+} are exchanged for Na^+ 17
Fig. S15: Summary of results for the Peel River, Mackenzie River, and Yukon River 18
Fig. S16: Carbonate weathering, silicate weathering, and sulfide oxidation Δ(ALK) and Δ(FIC) .. 19
Fig. S17: Annual discharge for all sites 20
Fig. S18: Annual Ca^{2+} flux for all sites 21
Fig. S19: Annual Mg^{2+} flux for all sites 22
Fig. S20: Annual Na^+ flux for all sites 23
Fig. S21: Annual SO_4^{2-} flux for all sites 24
Fig. S22: Annual Cl^- flux for all sites 25
Fig. S23: Annual Si flux for all sites 26
Fig. S24: Annual Ca^{2+}/Σ^+ flux ratio for all sites 27
Fig. S25: Annual Mg^{2+}/Σ^+ flux ratio for all sites 28
Fig. S26: Annual Na^+/Σ^+ flux ratio for all sites 29

Fig. S27: Annual SO_4^{2-}/Σ^+ flux ratio for all sites 30
Fig. S28: Annual Cl^-/Σ^+ flux ratio for all sites 31
Fig. S29: Annual Si/Σ^+ flux ratio for all sites 32
Fig. S30: Annual carbonate weathering flux for all sites 33
Fig. S31: Annual silicate weathering flux for all sites 34
Fig. S32: Annual sulfide oxidation weathering flux for all sites 35
Fig. S33: Carbonate and silicate weathering alkalinity from carbonate weathering (R) 36
Fig. S34: Carbonate and silicate weathering alkalinity offset by sulfide oxidation (Z) 37
Fig. S35: Annual discharge-weighted Δ(ALK) for all sites 38
Fig. S36: Annual discharge-weighted Δ(FIC) for all sites 39
Fig. S37: Annual ϕ for all sites 40
Fig. S38: Annual R for all sites 41
Fig. S39: Annual r for all sites 42
Fig. S40: Annual γ for all sites 43
Fig. S41: Annual λ for all sites 44
Fig. S42: Annual polar plots for all sites 45
Fig. S43: Mackenzie River subcatchment trends when silicate $Si/\Sigma^{\pm} = 1.0 \pm 0.5$ 46

Table S1: WRTDS regression performance by ion and site. Given values are the mean and one standard deviation of the distribution of the ratio between observed and reconstructed concentrations (also see Figs. S3 – S5). These standard deviations were used to estimate the uncertainty of the regression results for use in the MEANDIR inversions.

Site	Ca^{2+}	Mg^{2+}	Na^{+}	SO_4^{2-}	Cl^{-}	Si
YP-01	1.00 ± 0.11 (n = 291)	1.00 ± 0.14 (n = 292)	1.01 ± 0.13 (n = 293)	1.01 ± 0.21 (n = 258)	1.00 ± 0.24 (n = 256)	1.00 ± 0.15 (n = 292)
PL-01	1.01 ± 0.10 (n = 211)	1.01 ± 0.13 (n = 211)	1.01 ± 0.20 (n = 211)	1.02 ± 0.19 (n = 211)	1.00 ± 0.34 (n = 211)	1.01 ± 0.11 (n = 210)
MR-02	1.00 ± 0.09 (n = 368)	1.01 ± 0.11 (n = 358)	1.01 ± 0.13 (n = 367)	1.01 ± 0.18 (n = 351)	1.01 ± 0.20 (n = 351)	0.99 ± 0.12 (n = 361)
MR-03	1.00 ± 0.09 (n = 219)	1.00 ± 0.07 (n = 216)	1.01 ± 0.11 (n = 218)	1.01 ± 0.13 (n = 219)	1.02 ± 0.11 (n = 218)	0.99 ± 0.10 (n = 216)
MR-04	1.00 ± 0.04 (n = 155)	1.00 ± 0.06 (n = 155)	1.00 ± 0.06 (n = 155)	1.00 ± 0.10 (n = 154)	1.00 ± 0.08 (n = 155)	0.99 ± 0.13 (n = 156)
GR-05	1.00 ± 0.07 (n = 140)	1.00 ± 0.07 (n = 133)	1.00 ± 0.08 (n = 140)	1.00 ± 0.11 (n = 140)	1.00 ± 0.08 (n = 139)	1.00 ± 0.08 (n = 140)
LR-06	1.00 ± 0.36 (n = 137)	1.00 ± 0.13 (n = 129)	1.00 ± 0.37 (n = 138)	1.00 ± 0.30 (n = 133)	0.98 ± 0.52 (n = 137)	0.99 ± 0.43 (n = 131)
SN-12	1.00 ± 0.07 (n = 87)	0.99 ± 0.10 (n = 87)	1.00 ± 0.44 (n = 87)	1.00 ± 0.13 (n = 83)	0.99 ± 0.22 (n = 82)	1.00 ± 0.08 (n = 83)
FR-15	1.00 ± 0.09 (n = 157)	1.01 ± 0.11 (n = 156)	1.00 ± 0.26 (n = 154)	1.01 ± 0.15 (n = 240)	0.96 ± 0.72 (n = 157)	1.01 ± 0.10 (n = 160)
LR-17	1.00 ± 0.13 (n = 126)	1.00 ± 0.13 (n = 126)	0.99 ± 0.26 (n = 125)	1.00 ± 0.22 (n = 125)	0.98 ± 0.30 (n = 125)	1.00 ± 0.17 (n = 126)
LR-18	1.00 ± 0.10 (n = 292)	1.00 ± 0.11 (n = 287)	1.01 ± 0.24 (n = 293)	1.01 ± 0.14 (n = 290)	0.99 ± 0.53 (n = 292)	0.99 ± 0.11 (n = 292)
HR-19	1.00 ± 0.14 (n = 191)	1.00 ± 0.17 (n = 190)	0.99 ± 0.18 (n = 190)	0.99 ± 0.21 (n = 190)	0.99 ± 0.35 (n = 191)	0.99 ± 0.30 (n = 189)
SR-20	0.99 ± 0.10 (n = 328)	1.00 ± 0.10 (n = 319)	1.00 ± 0.18 (n = 323)	1.00 ± 0.17 (n = 324)	1.01 ± 0.24 (n = 322)	0.99 ± 0.14 (n = 323)
PR-21	1.00 ± 0.06 (n = 273)	1.00 ± 0.08 (n = 268)	0.99 ± 0.28 (n = 273)	1.00 ± 0.19 (n = 276)	0.98 ± 0.60 (n = 274)	1.00 ± 0.17 (n = 273)
AR-23	1.00 ± 0.05 (n = 407)	1.01 ± 0.07 (n = 404)	1.01 ± 0.12 (n = 406)	1.01 ± 0.11 (n = 407)	0.99 ± 0.37 (n = 404)	1.01 ± 0.11 (n = 407)

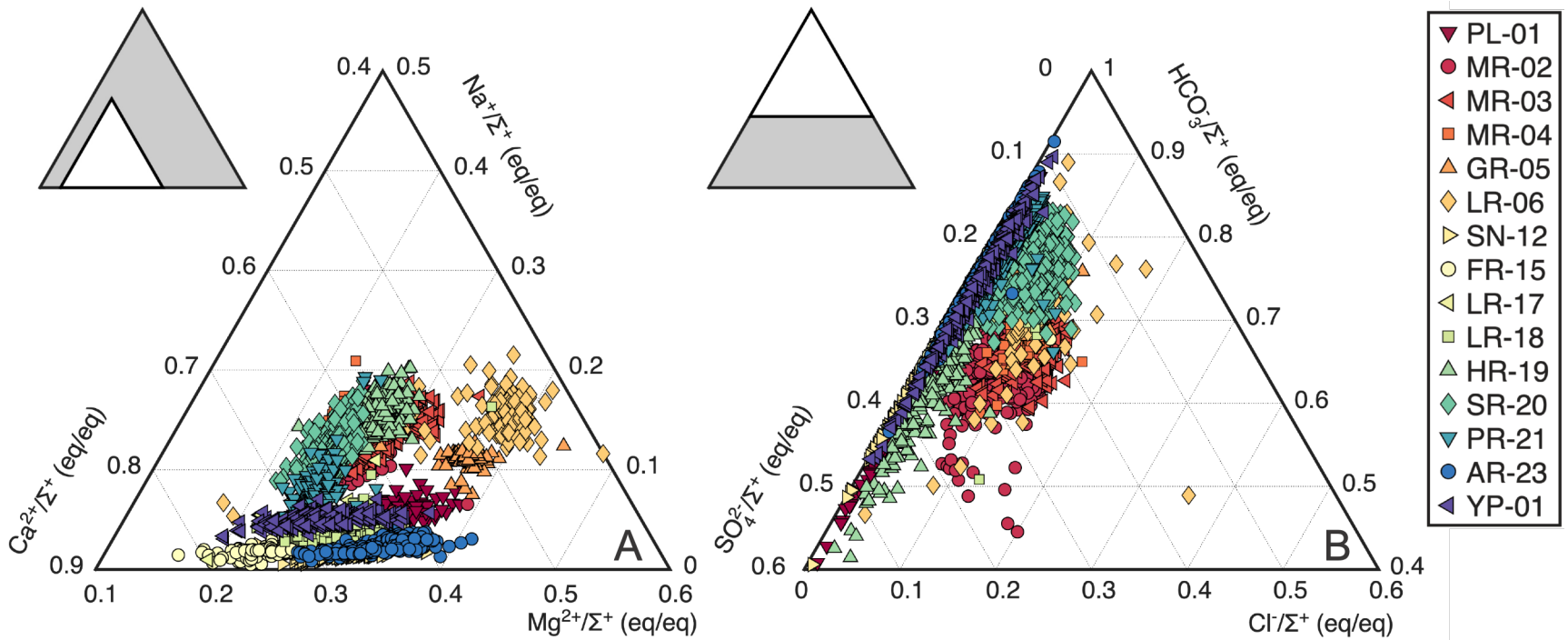


Fig. S1: Cation and anion ternary diagrams. (**A**) The Ca^{2+} – Mg^{2+} – Na^{+} ternary diagram indicates that Ca^{2+} dominates the cation budget of most samples, with a secondary contribution from Mg^{2+} and a tertiary role for Na^{+}. (**B**) The SO_4^{2-} – Cl^{-} – HCO_3^{-} ternary diagram indicates that HCO_3^{-} dominates the anion budget of most samples, with a secondary contribution from SO_4^{2-}. Despite the rising importance of SO_4^{2-} in many permafrost environments, HCO_3^{-} remains the primary anion in river water. The plotted areas are subspaces of the full ternaries, as indicated by the white triangles within grey triangles above each panel.

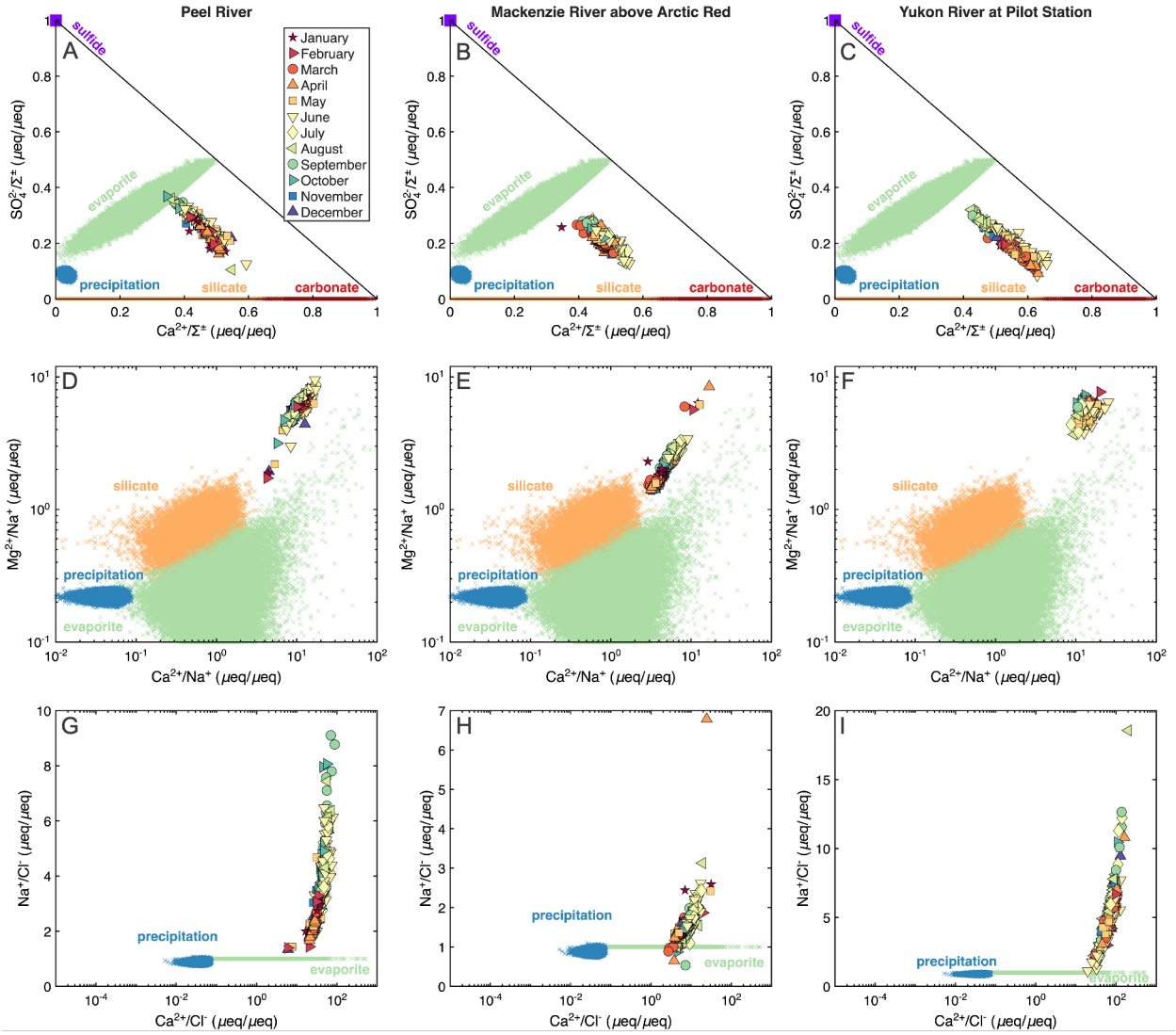


Fig. S2: Mixing plots with end-member chemical ratios. (**A-C**) $SO_4^{2-}/\Sigma^{\pm}$ against $Ca^{2+}/\Sigma^{\pm}$, where $\Sigma^{\pm} = Ca^{2+} + Mg^{2+} + Na^{+} + SO_4^{2-}$ in charge equivalents. (**D-F**) Mg^{2+}/Na^{+} against Ca^{2+}/Na^{+} helps to distinguish contributions from carbonate and silicate end-members while (**G-I**) Na^{+}/Cl^{-} against Ca^{2+}/Cl^{-} helps to distinguish contributions from the evaporite and precipitation end-members.

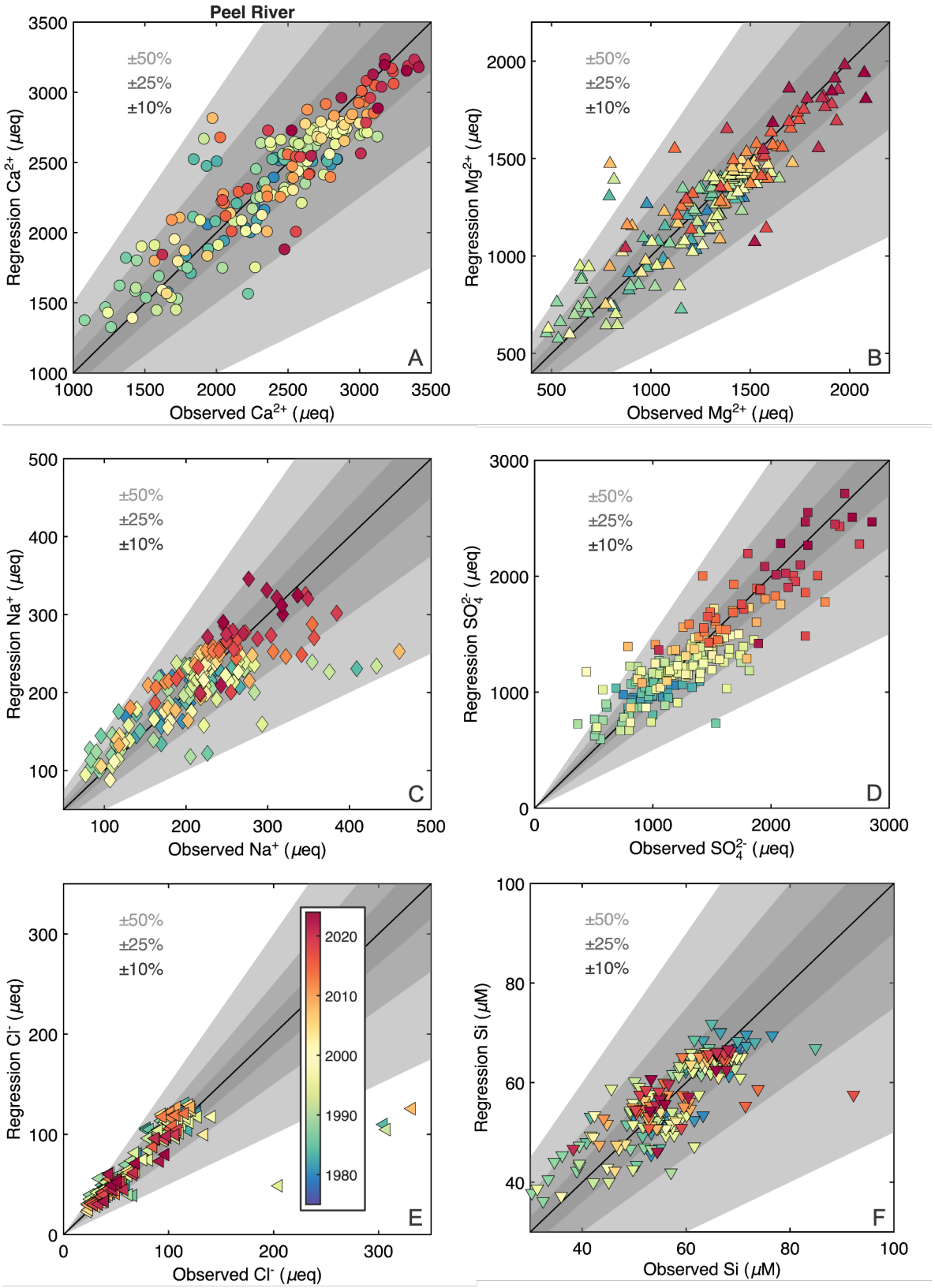


Fig. S3: Comparison of Peel River observations and regression results for (**A**) Ca^{2+}, (**B**) Mg^{2+}, (**C**) Na^{+}, (**D**) SO_4^{2-}, (**E**) Cl^{-}, and (**F**) Si with shading for ±10%, ±25%, and ±50%.

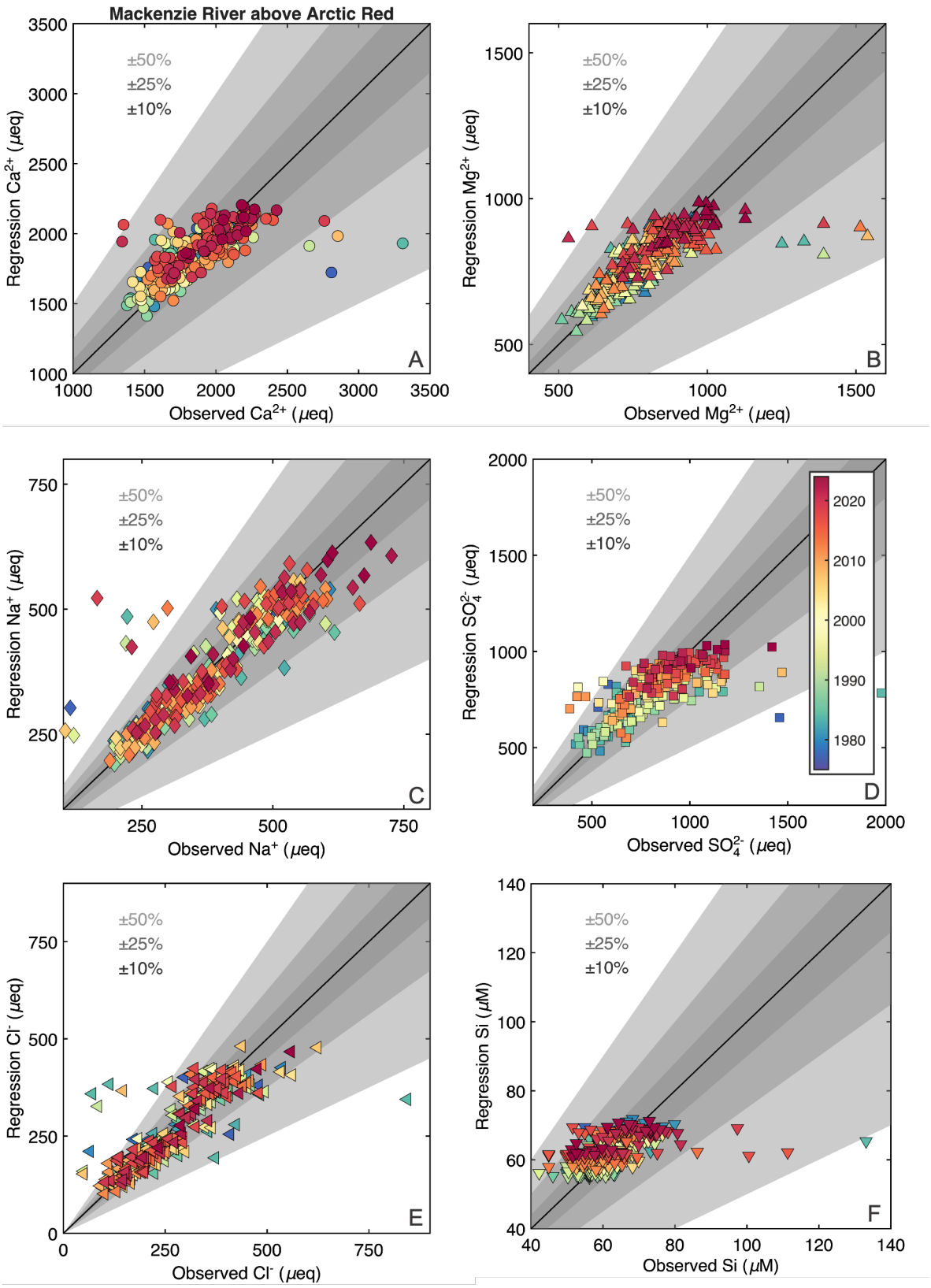


Fig. S4: Comparison of Mackenzie River observations and regression results for (**A**) Ca^{2+}, (**B**) Mg^{2+}, (**C**) Na^{+}, (**D**) SO_4^{2-}, (**E**) Cl^{-}, and (**F**) Si with shading for ±10%, ±25%, and ±50%.

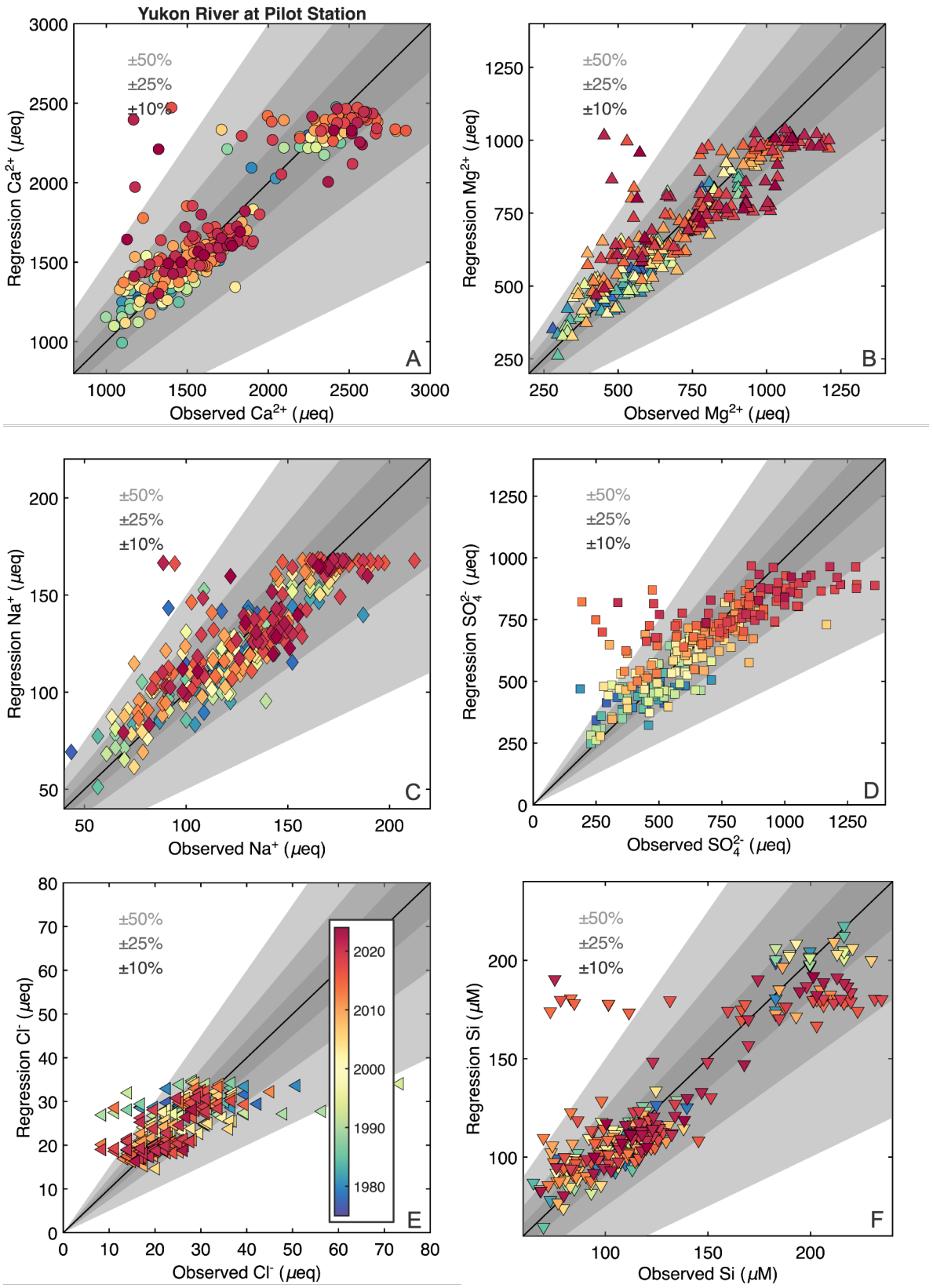


Fig. S5: Comparison of Yukon River observations and regression results for (**A**) Ca^{2+}, (**B**) Mg^{2+}, (**C**) Na^{+}, (**D**) SO_4^{2-}, (**E**) Cl^{-}, and (**F**) Si with shading for ±10%, ±25%, and ±50%.

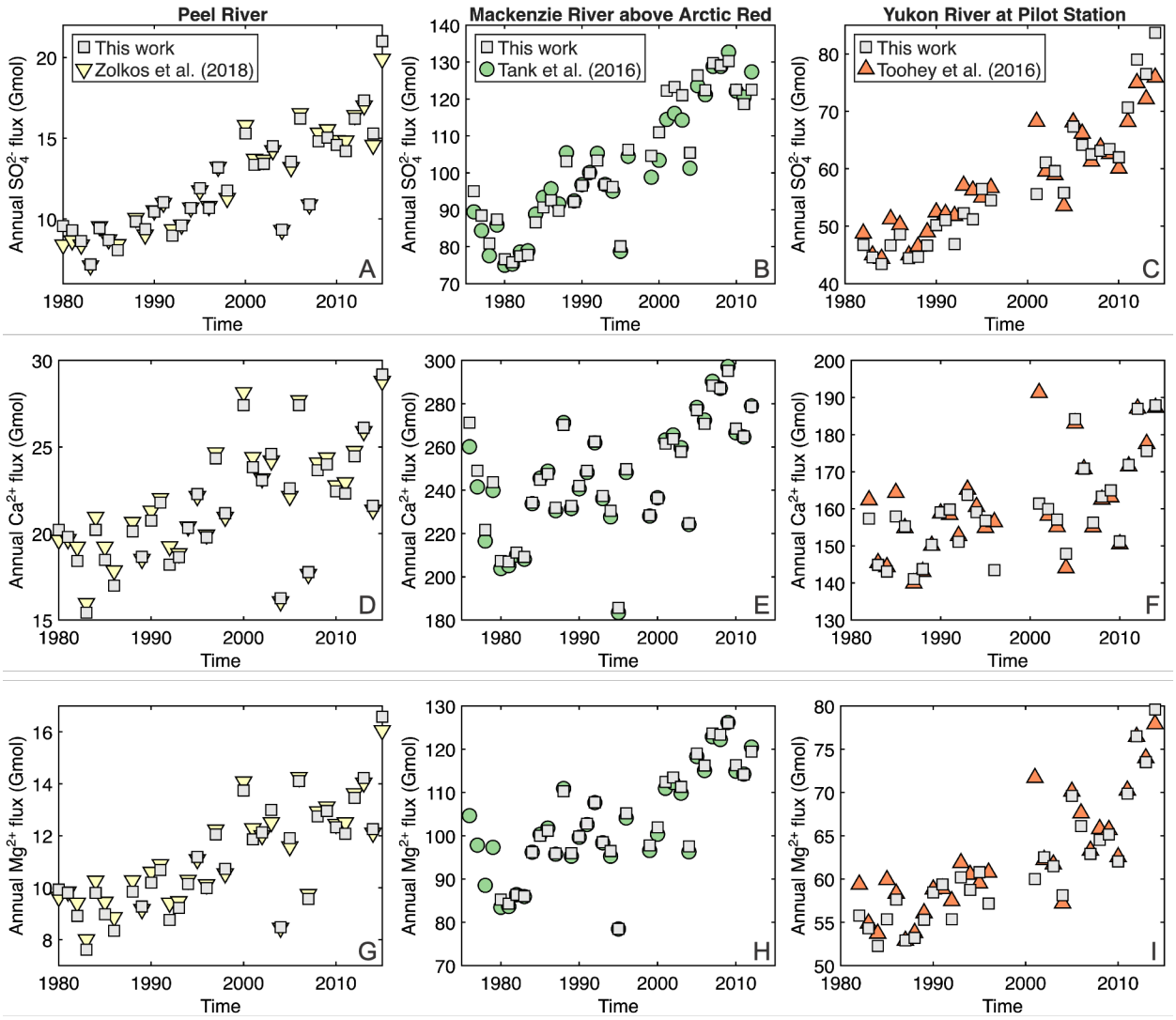


Fig. S6: Comparison of WRTDS-derived annual SO_4^{2-}, Ca^{2+}, and Mg^{2+} fluxes with prior estimates. The results of this work agree with previous flux calculations for (**A, D, G**) the Peel River (Zolkos et al., 2018), (**B, E, H**) the Mackenzie River (Tank et al., 2016), and (**C, F, I**) the Yukon River (Toohey et al., 2016). Plotted data for prior studies were digitized from plots in the original publications.

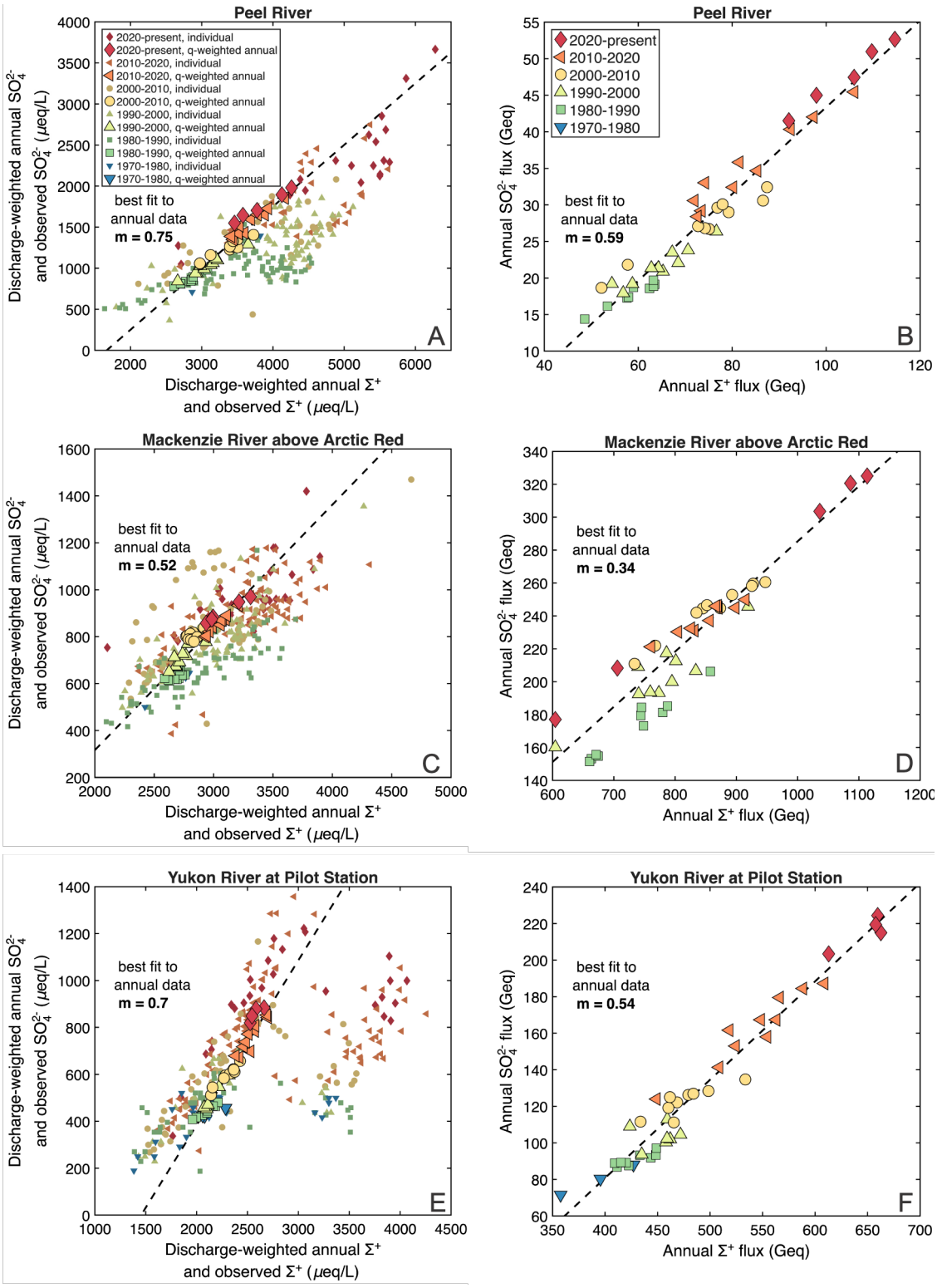


Fig. S7: SO_4^{2-} against Σ^+ (Ca^{2+} + Mg^{2+} + Na^+) for the (**A**, **B**) Peel River, (**C**, **D**) Mackenzie River, and (**E**, **F**) Yukon River. (**A**, **C**, **E**) Discharge-weighted regression results for each year (larger symbols) and individual sample observations (smaller symbols). All sites show SO_4^{2-} and Σ^+ concentrations increasing through time. (**B**, **D**, **F**) Annual flux data. Theil-Sen fits have slopes less than 1, indicating that increases in Σ^+ flux exceed increases in SO_4^{2-} flux.

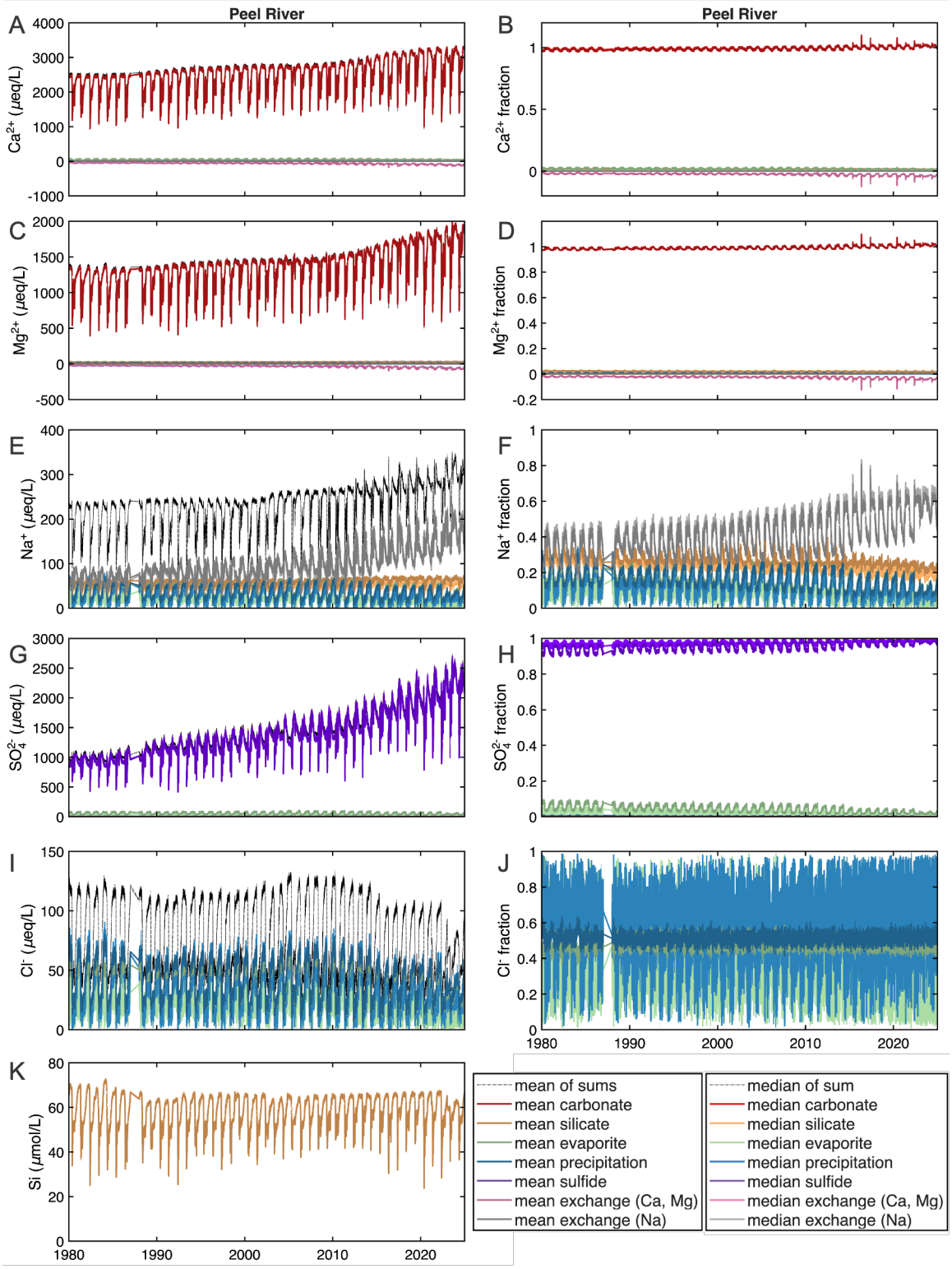


Fig. S8: Inversion results for the Peel River. Median (light colors) and mean (dark colors) daily results are plotted for both **(A, C, E, G, I, K)** absolute and **(B, D, F, H, J)** fractional contributions to the river dissolved Ca^{2+}, Mg^{2+}, Na^{+}, SO_4^{2-}, Cl^{-}, and Si budgets from carbonate weathering, silicate weathering, evaporite dissolution, meteoric precipitation, sulfide oxidation, and exchange end-members. Results are for an inversion with silicate $Si/\Sigma^{\pm} = 0.5 \pm 0.25$.

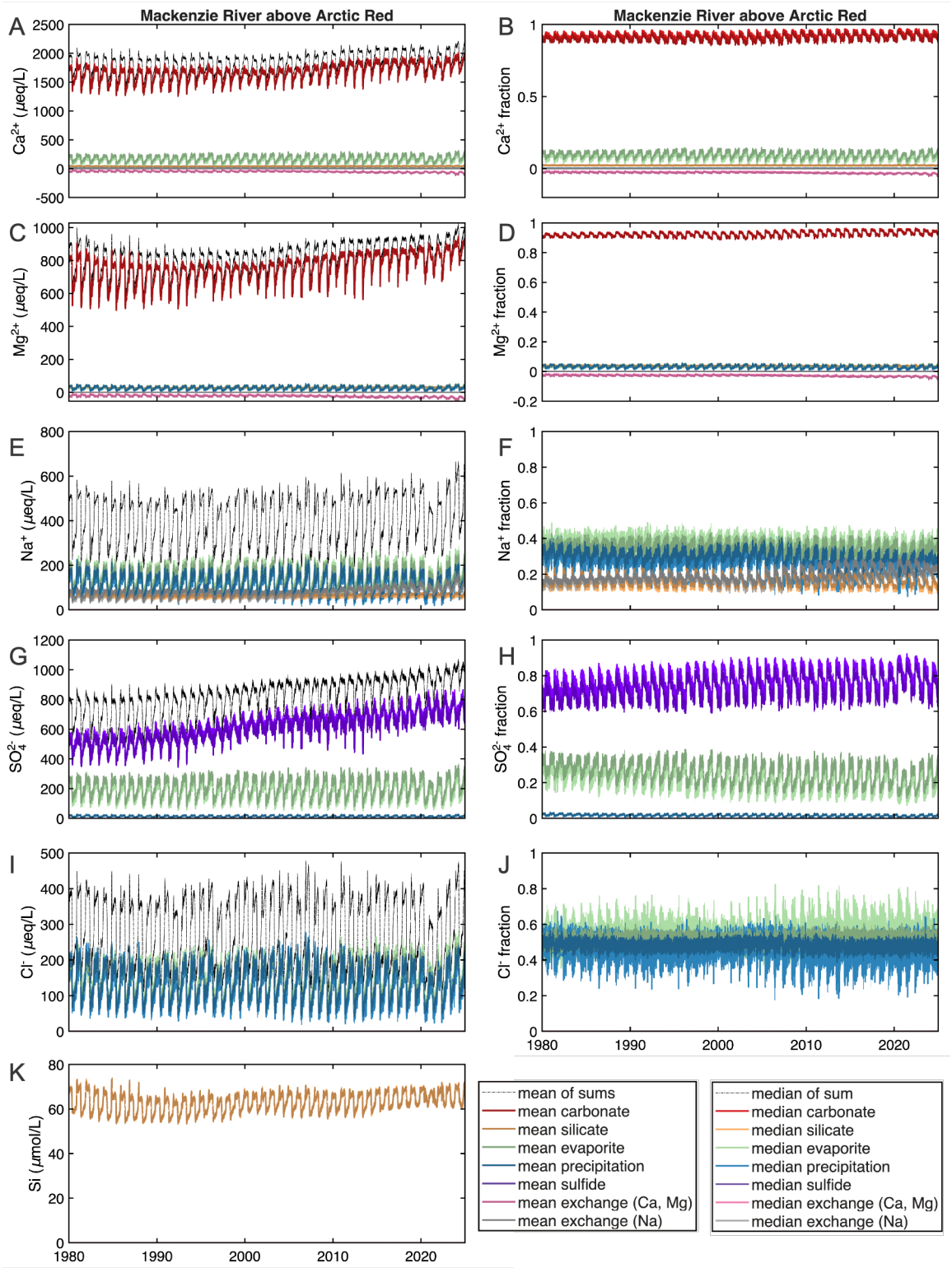


Fig. S9: Inversion results for the Mackenzie River. Median (light colors) and mean (dark colors) daily results are plotted for both **(A, C, E, G, I, K)** absolute and **(B, D, F, H, J)** fractional contributions to the river dissolved Ca^{2+}, Mg^{2+}, Na^{+}, SO_4^{2-}, Cl^{-}, and Si budgets from carbonate weathering, silicate weathering, evaporite dissolution, meteoric precipitation, sulfide oxidation, and exchange end-members. Results are for an inversion with silicate $Si/\Sigma^{\pm} = 0.5 \pm 0.25$.

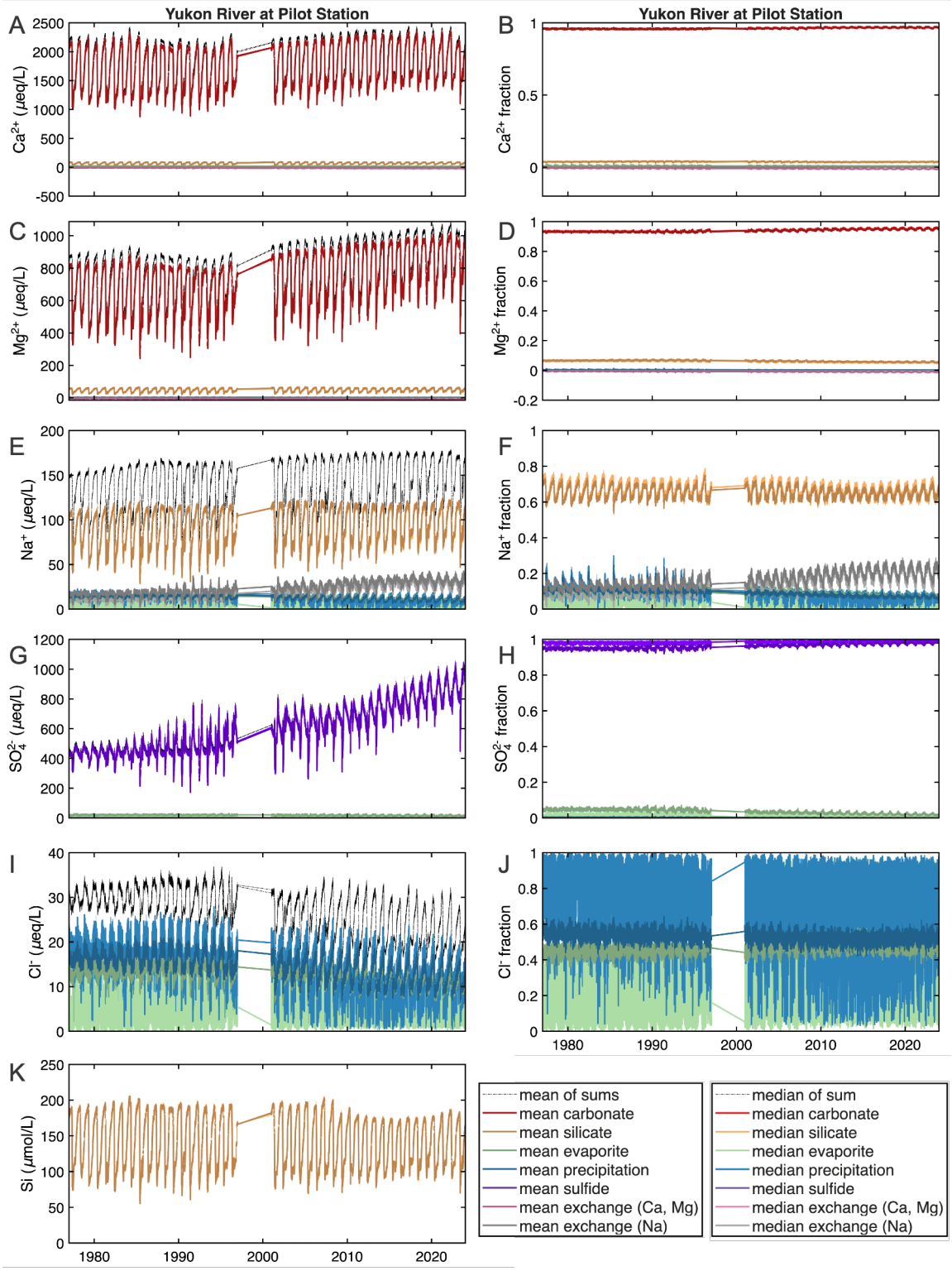


Fig. S10: Inversion results for the Yukon River. Median (light colors) and mean (dark colors) daily results are plotted for both **(A, C, E, G, I, K)** absolute and **(B, D, F, H, J)** fractional contributions to the river dissolved Ca^{2+}, Mg^{2+}, Na^{+}, SO_4^{2-}, Cl^{-}, and Si budgets from carbonate weathering, silicate weathering, evaporite dissolution, meteoric precipitation, sulfide oxidation, and exchange end-members. Results are for an inversion with silicate $Si/\Sigma^{\pm} = 0.5 \pm 0.25$.

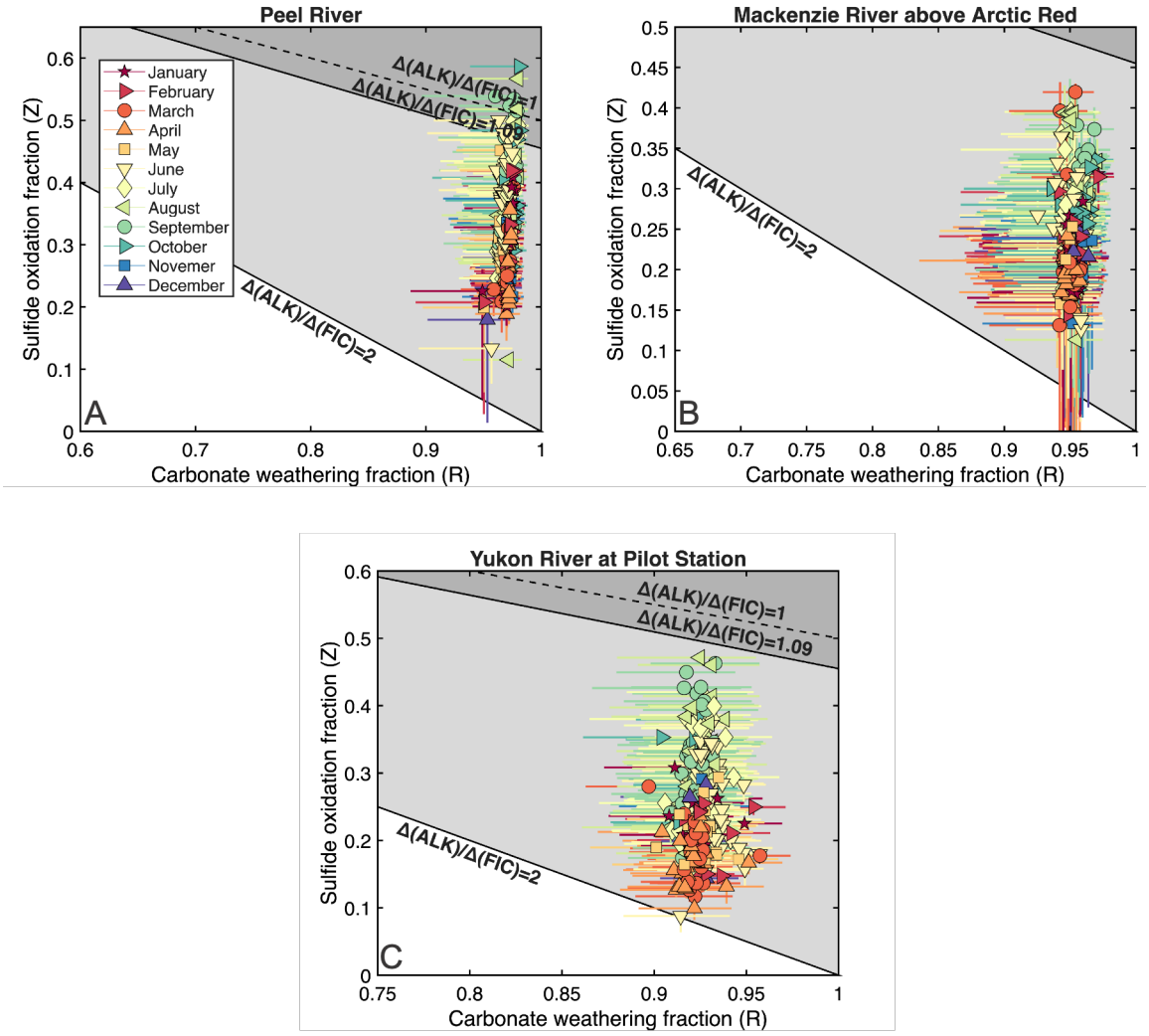


Fig. S11: MEANDIR inversion results for samples collected from the (**A**) Peel River, (**B**) Mackenzie River, and (**C**) Yukon River showing the fraction of carbonate and silicate weathering offset through sulfide oxidation (denoted as Z) against the carbonate fraction of carbonate and silicate weathering alkalinity (denoted as R) (Torres et al., 2016). Note that this R, representing the carbonate weathering fraction, is a distinct quantity from the variable R representing the magnitude of the chemical weathering vector. Points are distribution medians and error bars extend from the 5th to the 95th percentile of accepted simulation results for an inversion with silicate Si/Σ^{+} equal to 0.5 ± 0.25. Higher values of silicate Si/Σ^{+} would generally result in elevated values for the fraction of carbonate mineral weathering and lower weathering $\Delta(ALK)/\Delta(FIC)$ ratios. Most points reflect weathering systems with $\Delta(ALK)/\Delta(FIC) > 1.09$ and $\Delta(ALK)/\Delta(FIC) < 2$, corresponding to weathering that acts as a short-term sink and a long-term source of pCO_2.

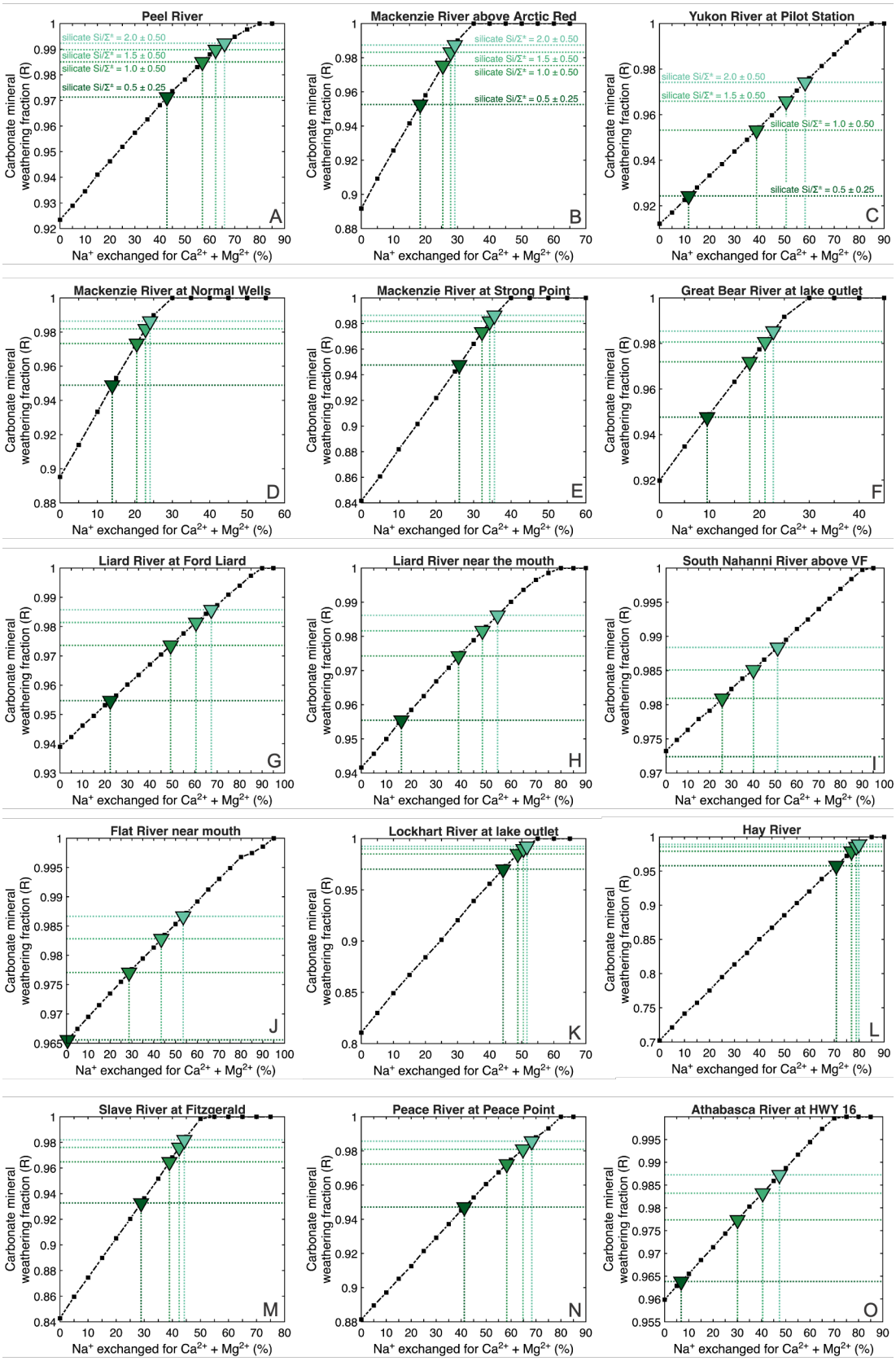


Fig. S12: Changes in carbonate weathering fraction as Na^+ is exchanged for Ca^{2+} and Mg^{2+}.

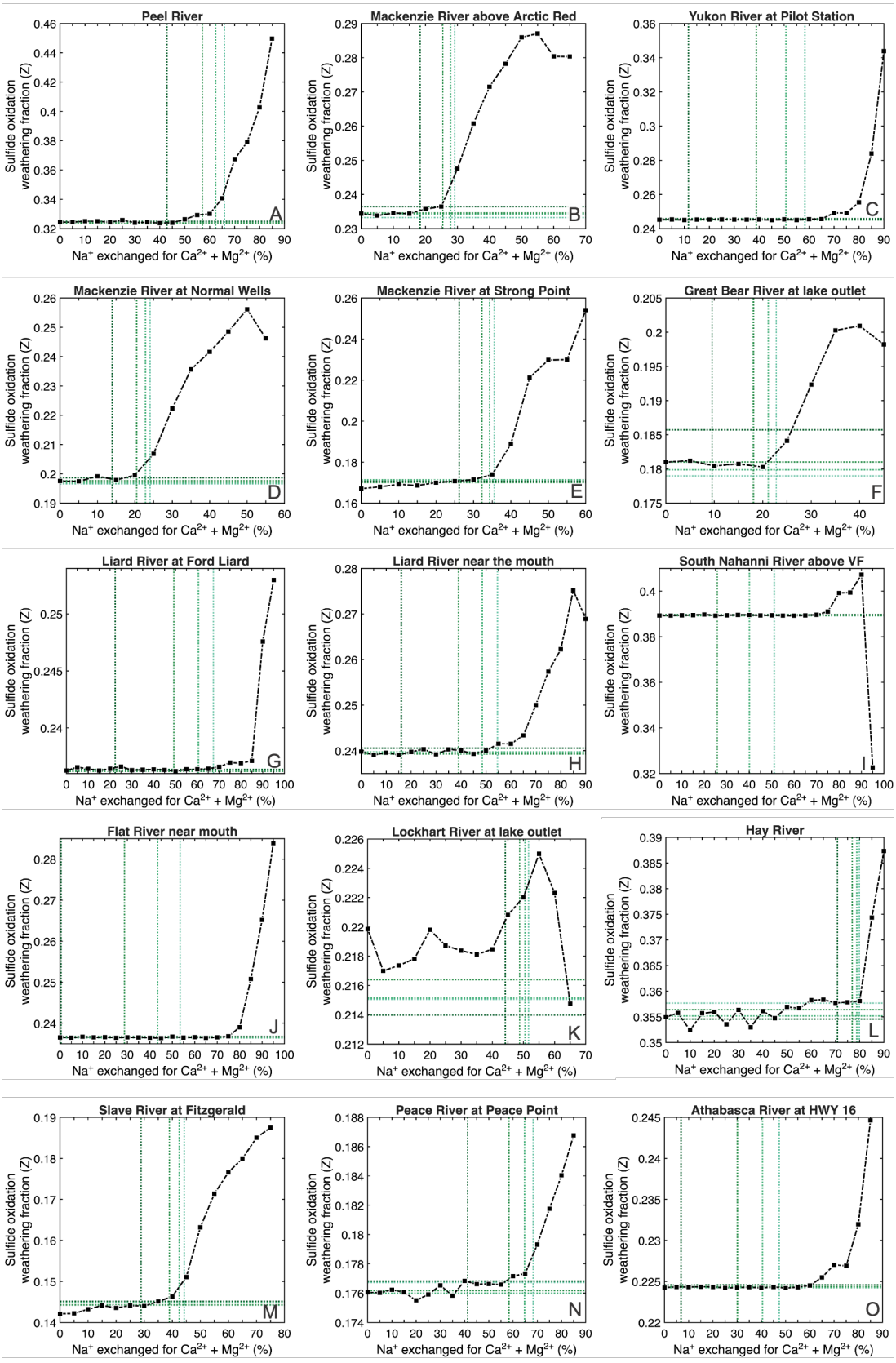


Fig. S13: Changes in sulfide oxidation fraction as Na^+ is exchanged for Ca^{2+} and Mg^{2+}.

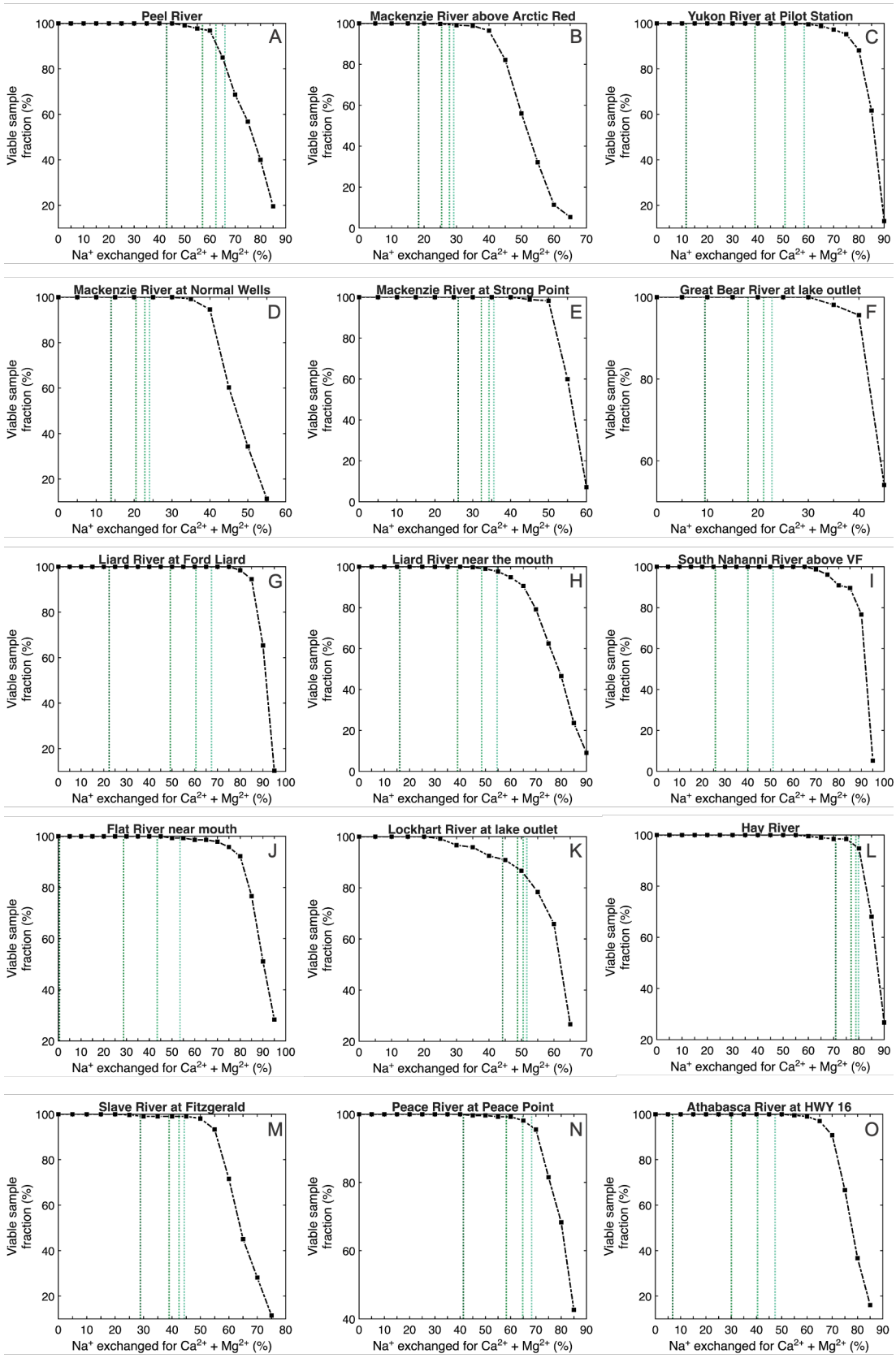


Fig. S14: Changes in viable sample fraction as Na^+ is exchanged for Ca^{2+} and Mg^{2+}.

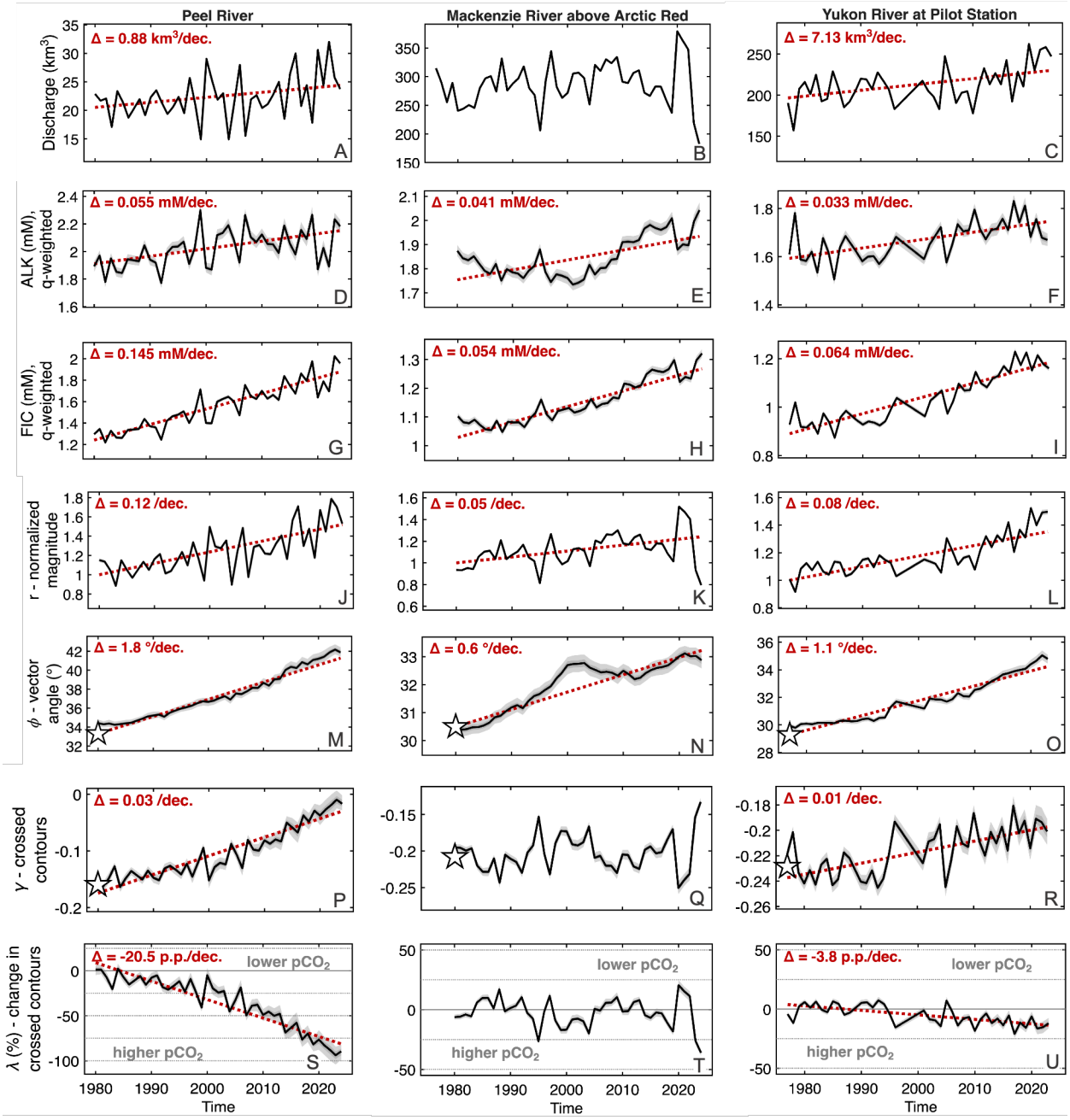


Fig. S15: Annual (**A-C**) discharge, (**D-F**) discharge-weighted Δ(ALK), (**G-I**) discharge-weighted Δ(FIC), (**J-L**) normalized weathering vector magnitude r, (**M-O**) weathering vector angle ϕ, (**P-R**) crossed pCO_2 contours γ, and **(S-U)** fractional change in crossed pCO_2 contours λ. Theil-Sen trends are plotted when significant ($p < 0.05$). Shading indicates the 5^{th}-95^{th} and 25^{th}-75^{th} percentiles of results. Results are for an inversion with silicate $Si/\Sigma^{\pm} = 0.5 \pm 0.25$.

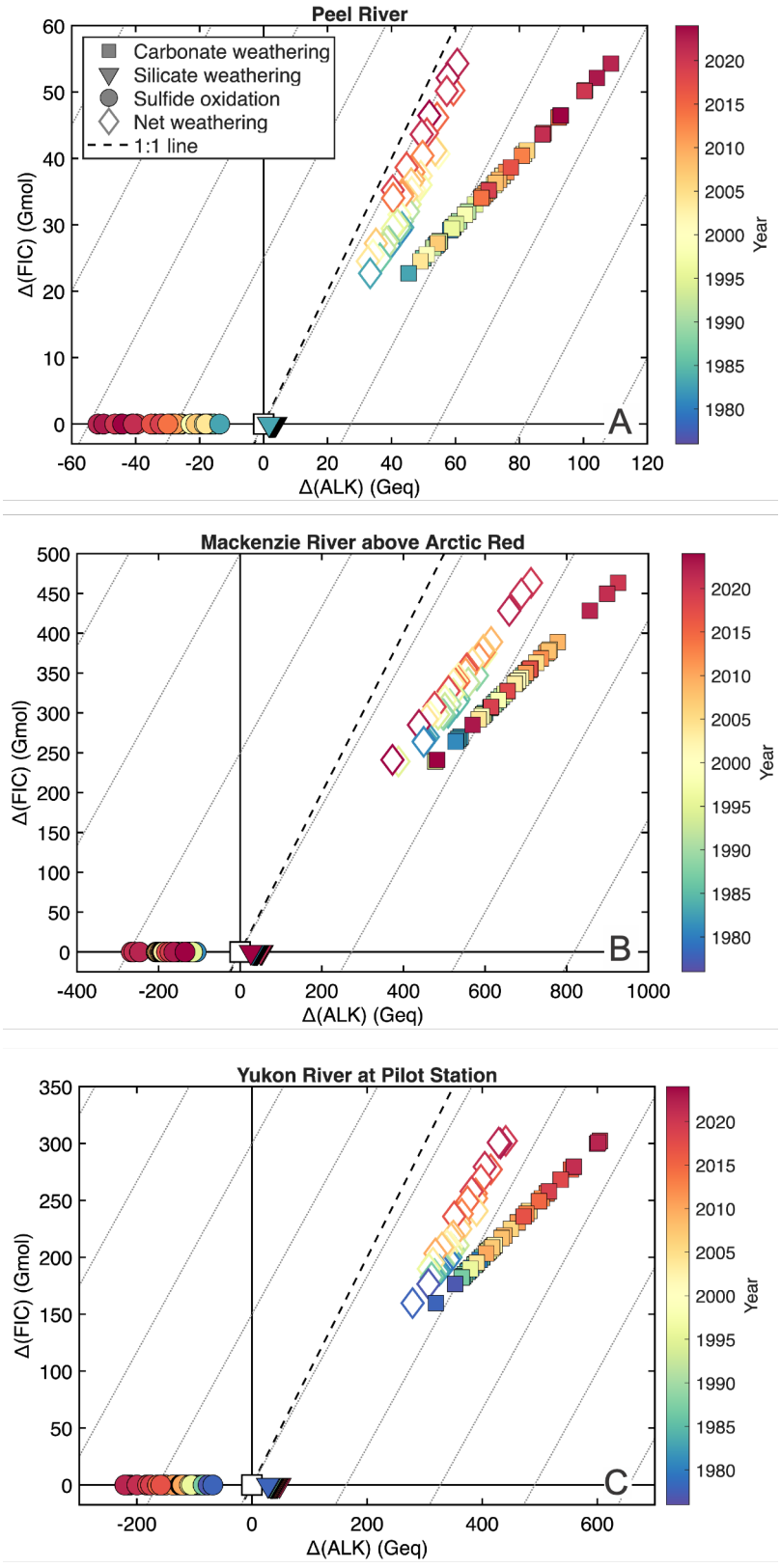


Fig. S16: Annual Δ(ALK) and Δ(FIC) fluxes due to carbonate weathering, silicate weathering, and sulfide oxidation (closed symbols) and the net weathering vector (open symbols).

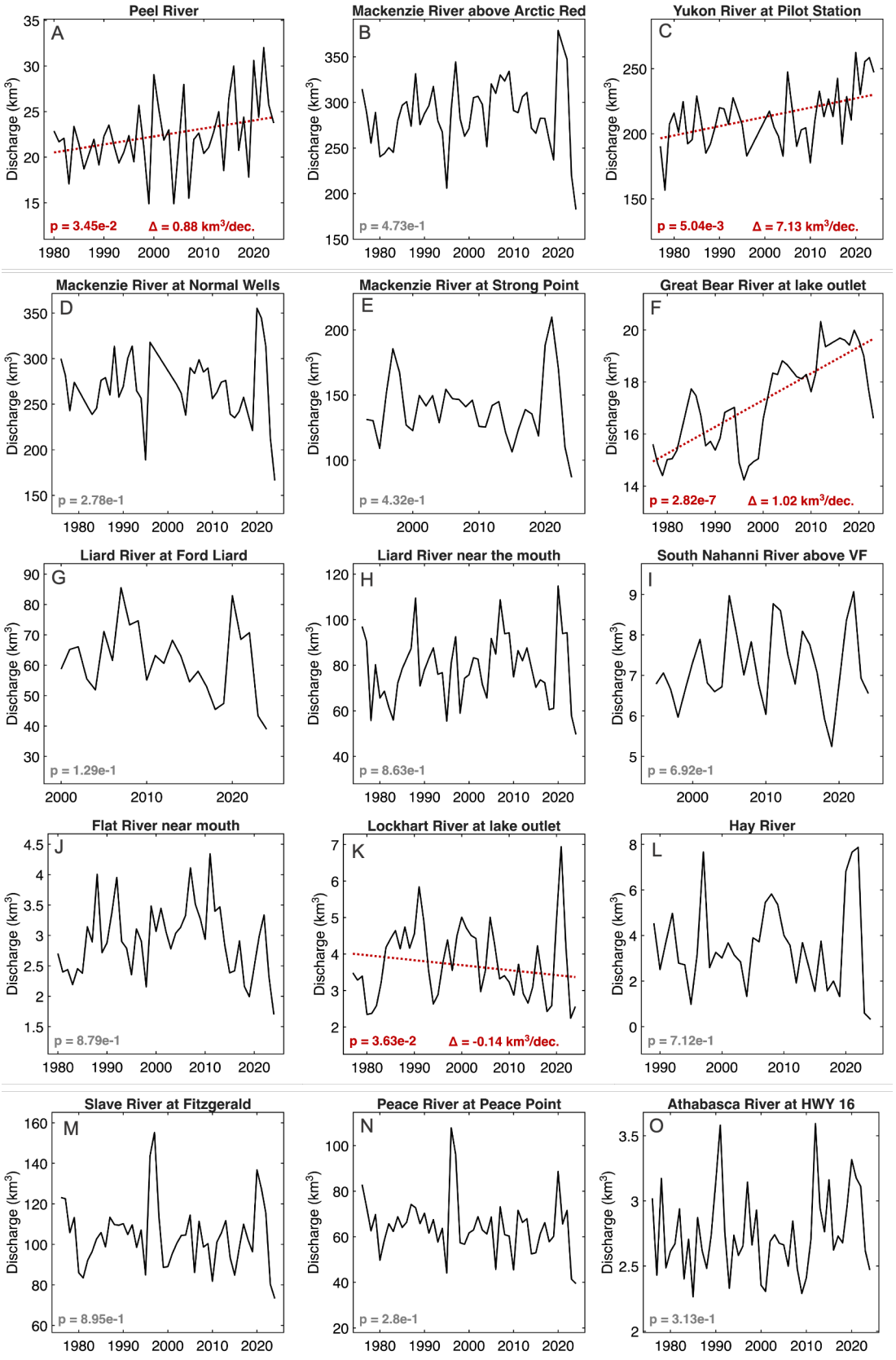


Fig. S17: Annual discharge for each site with Theil-Sen trends plotted when significant ($p < 0.05$).

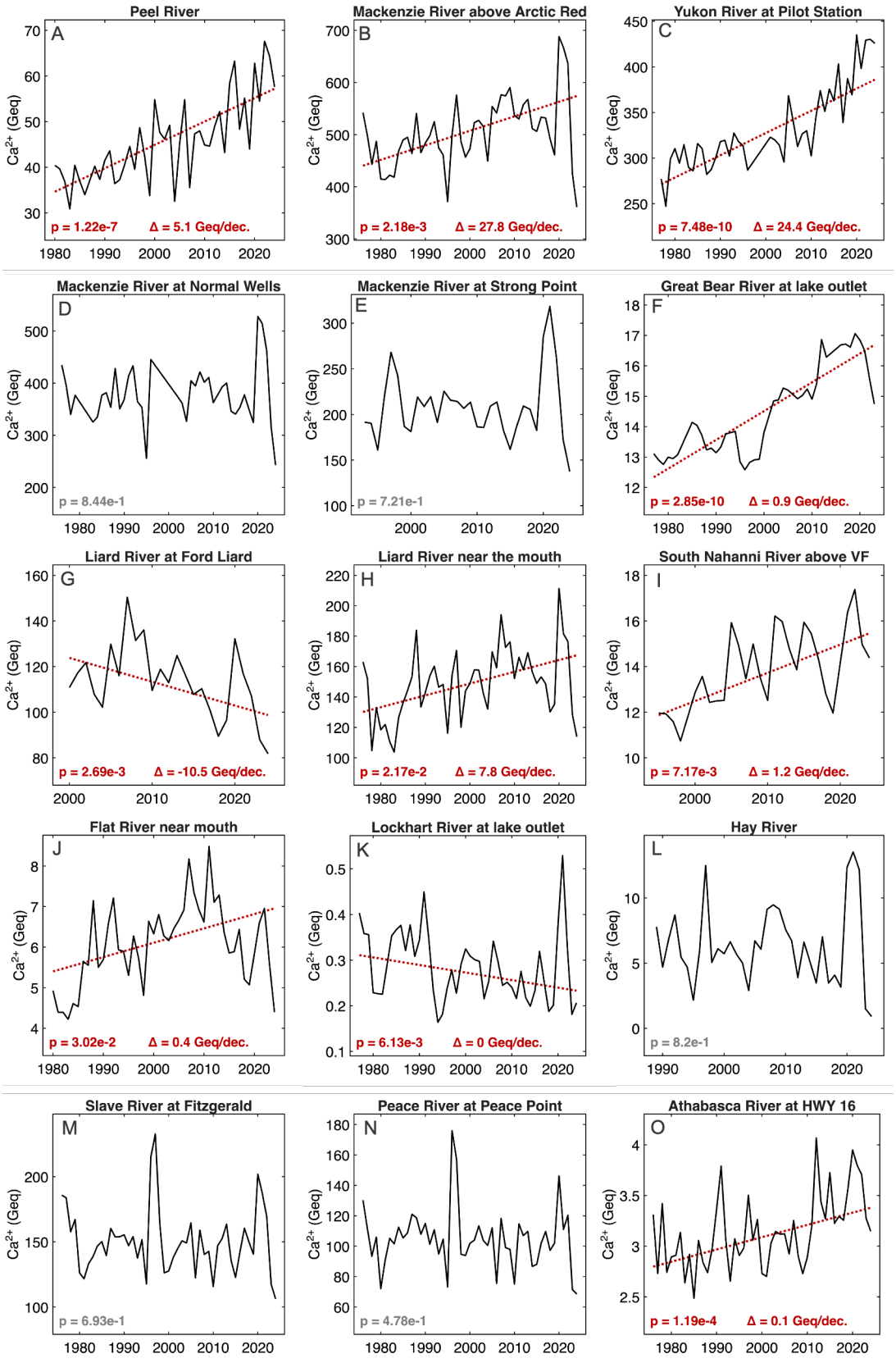


Fig. S18: Annual Ca^{2+} flux for each site with Theil-Sen trends plotted when significant ($p < 0.05$).

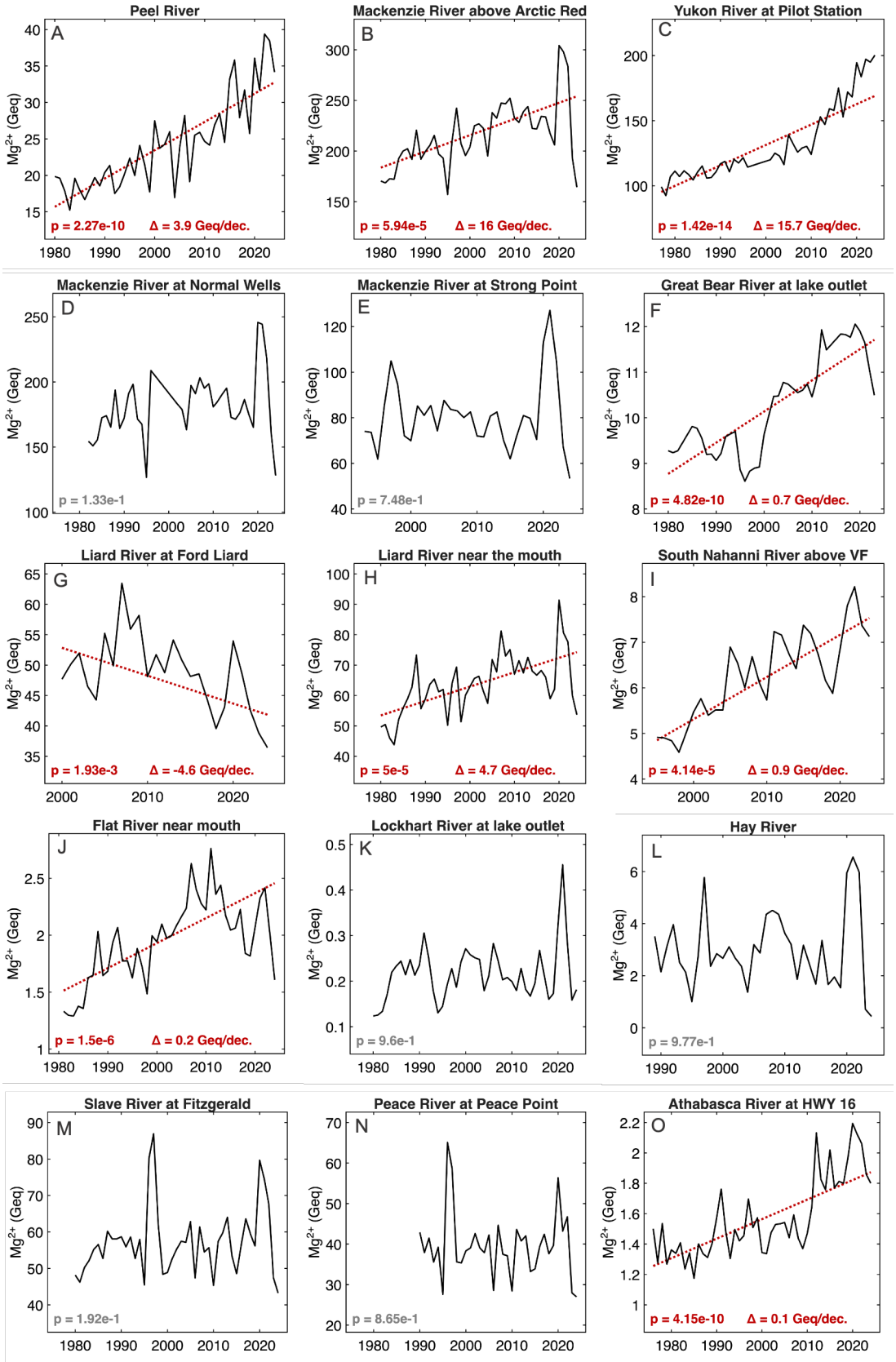


Fig. S19: Annual Mg^{2+} flux for each site with Theil-Sen trends plotted when significant ($p < 0.05$).

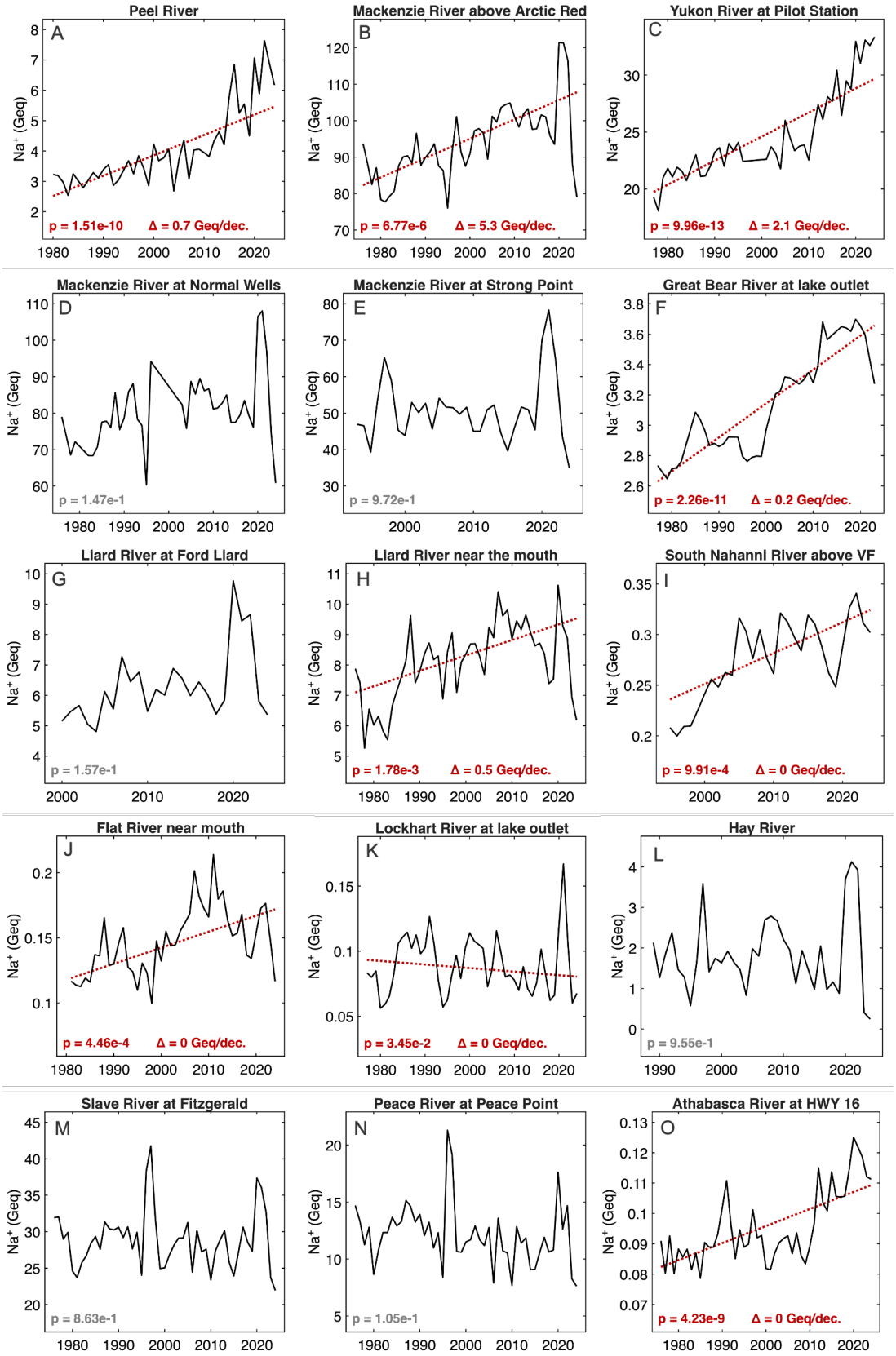


Fig. S20: Annual Na^+ flux for each site with Theil-Sen trends plotted when significant ($p < 0.05$).

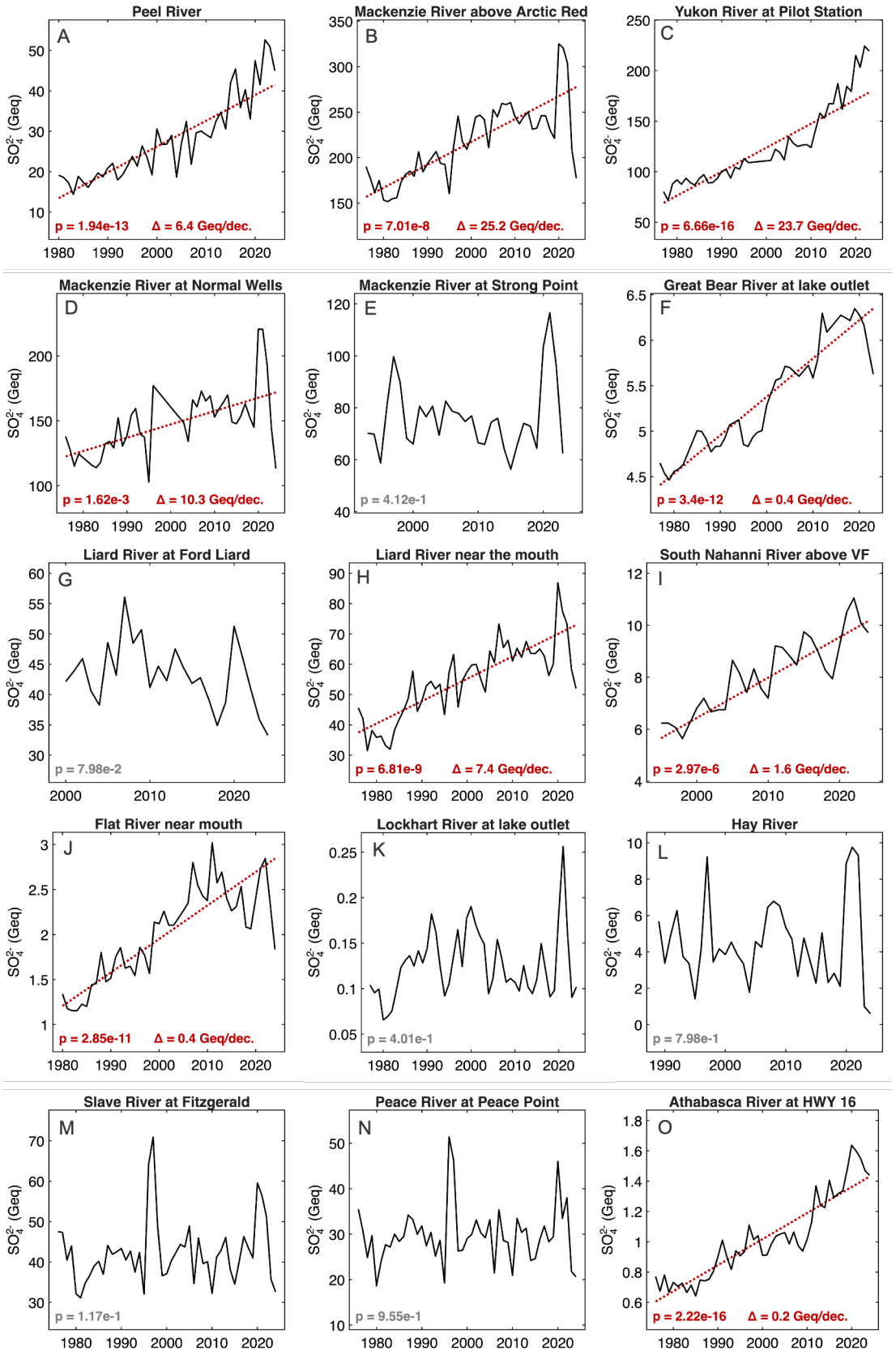


Fig. S21: Annual SO_4^{2-} flux for each site with Theil-Sen trends plotted when significant ($p < 0.05$).

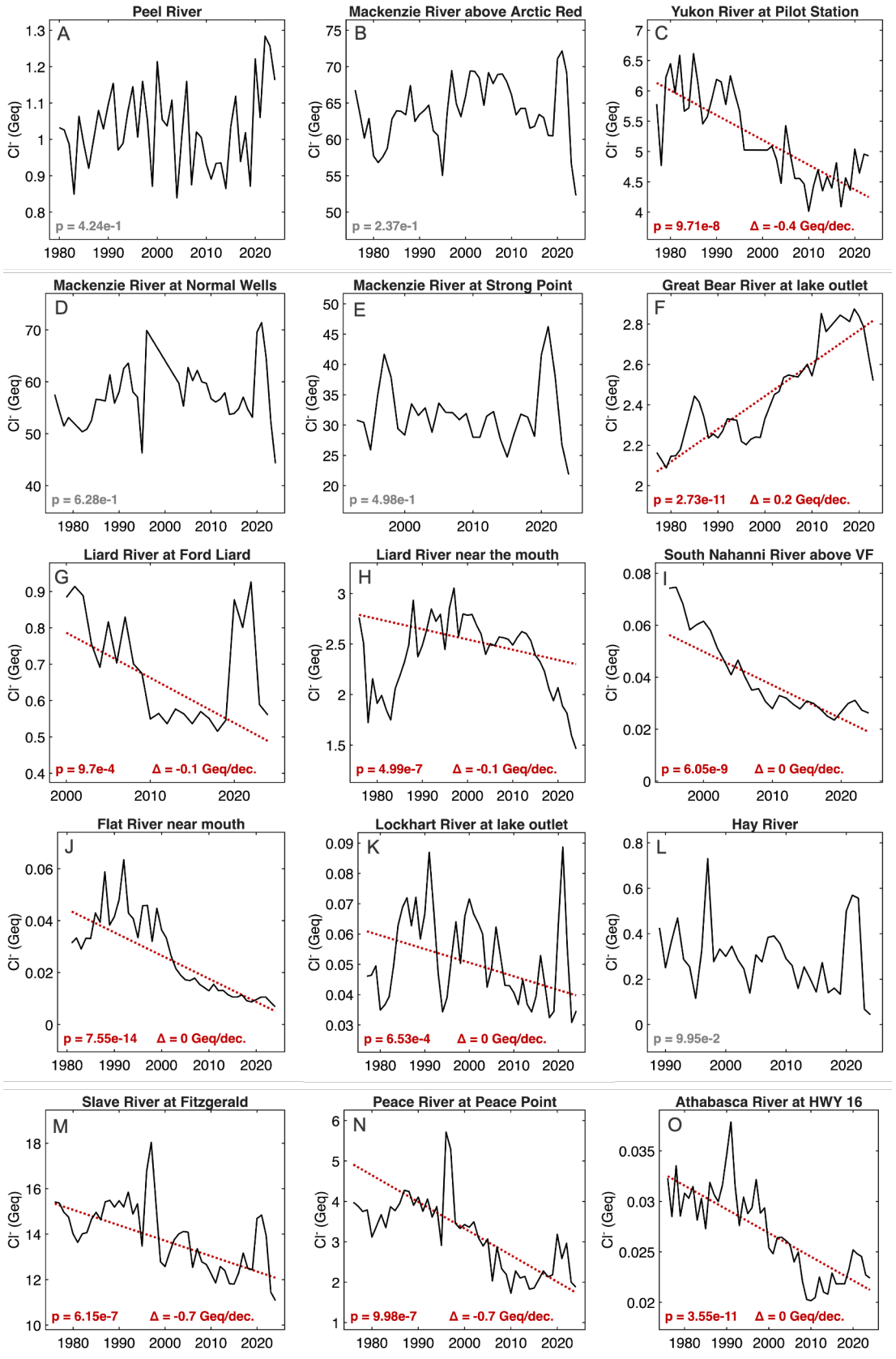


Fig. S22: Annual Cl^- flux for each site with Theil-Sen trends plotted when significant ($p < 0.05$).

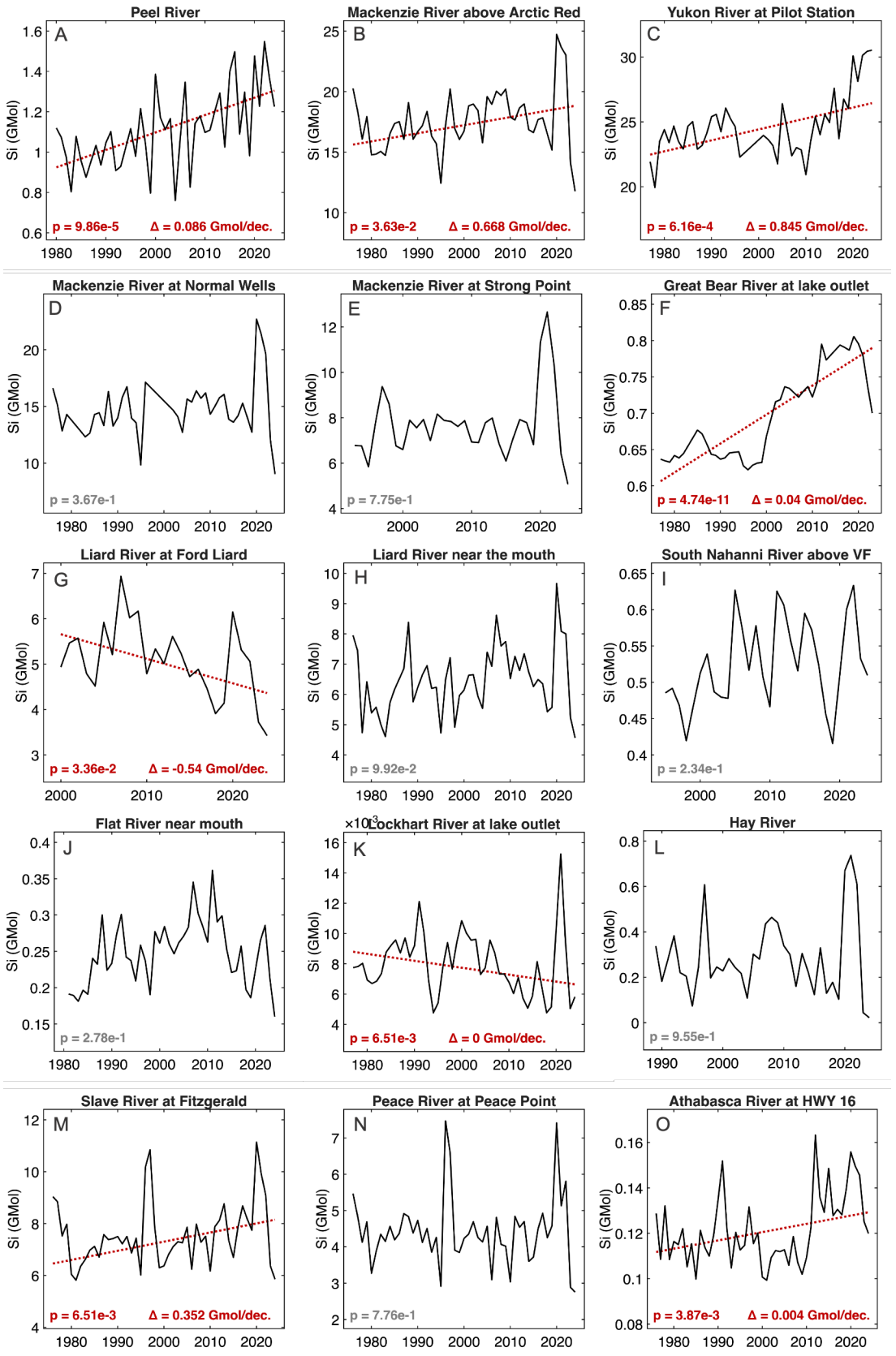


Fig. S23: Annual Si flux for each site with Theil-Sen trends plotted when significant ($p < 0.05$).

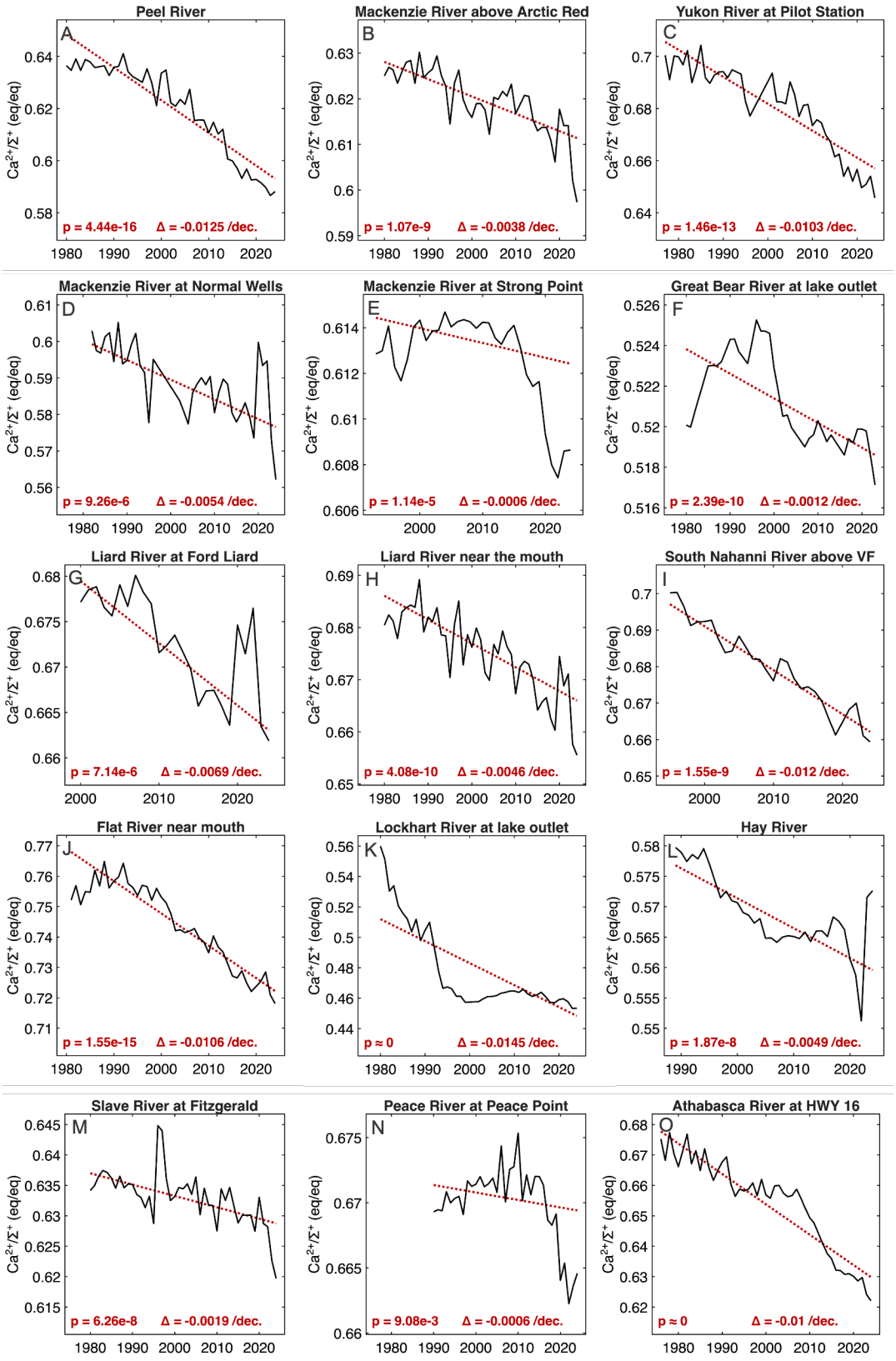


Fig. S24: Annual Ca^{2+}/Σ^{+} flux ratio for each site with Theil-Sen trends plotted when significant ($p < 0.05$).

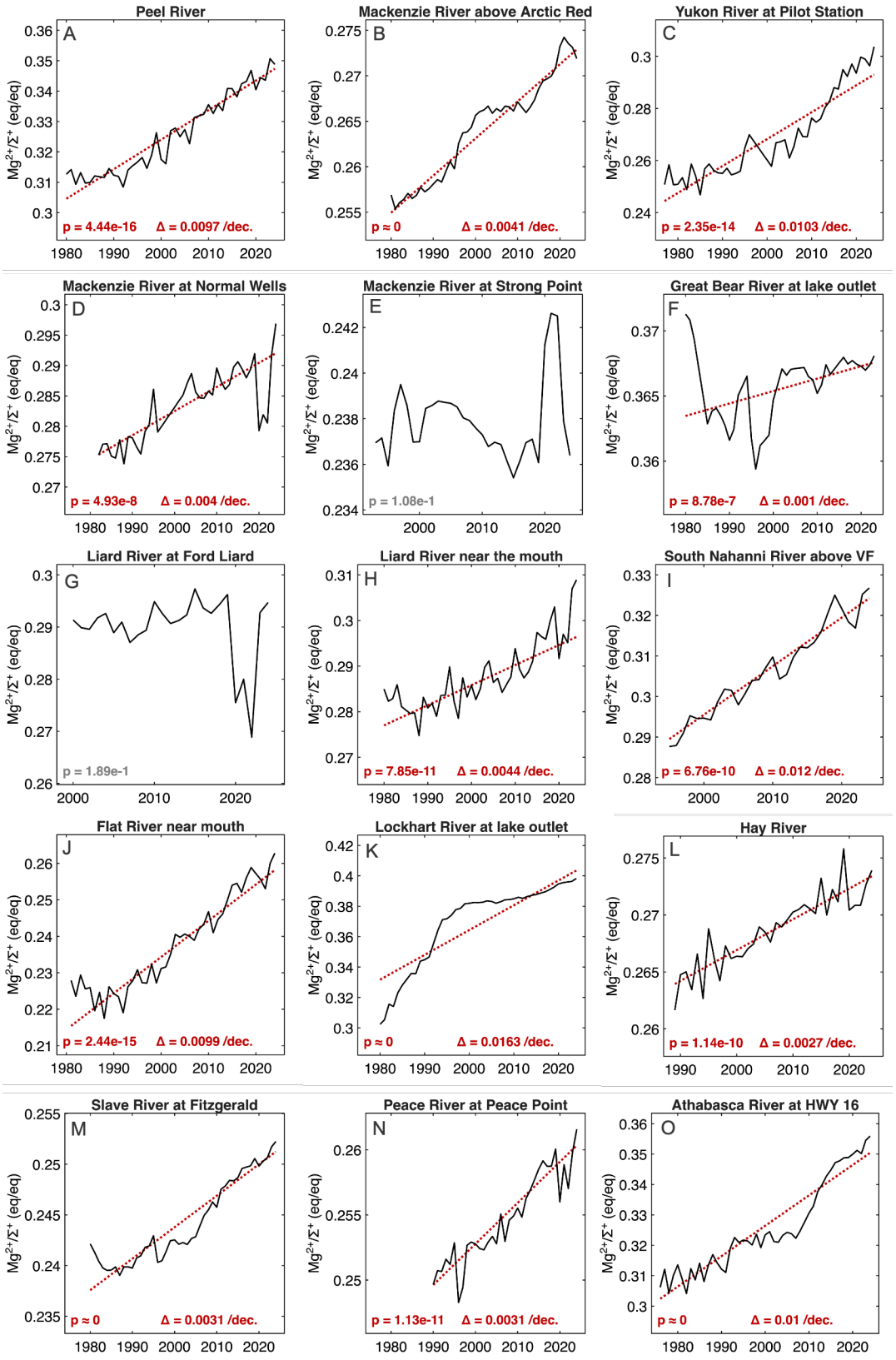


Fig. S25: Annual Mg^{2+}/Σ^{+} flux ratio for each site with Theil-Sen trends plotted when significant ($p < 0.05$).

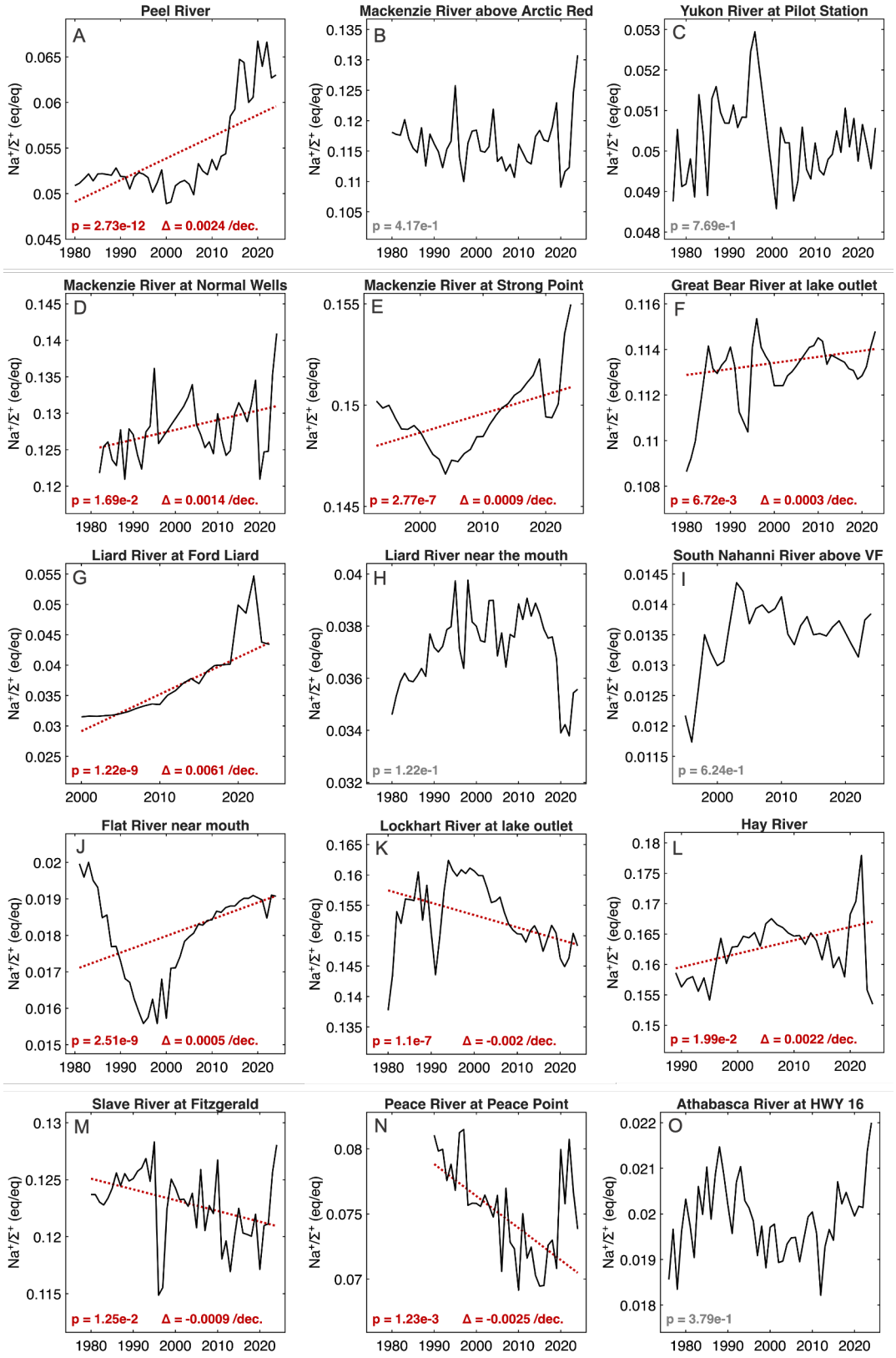


Fig. S26: Annual Na^+/Σ^+ flux ratio for each site with Theil-Sen trends plotted when significant ($p < 0.05$).

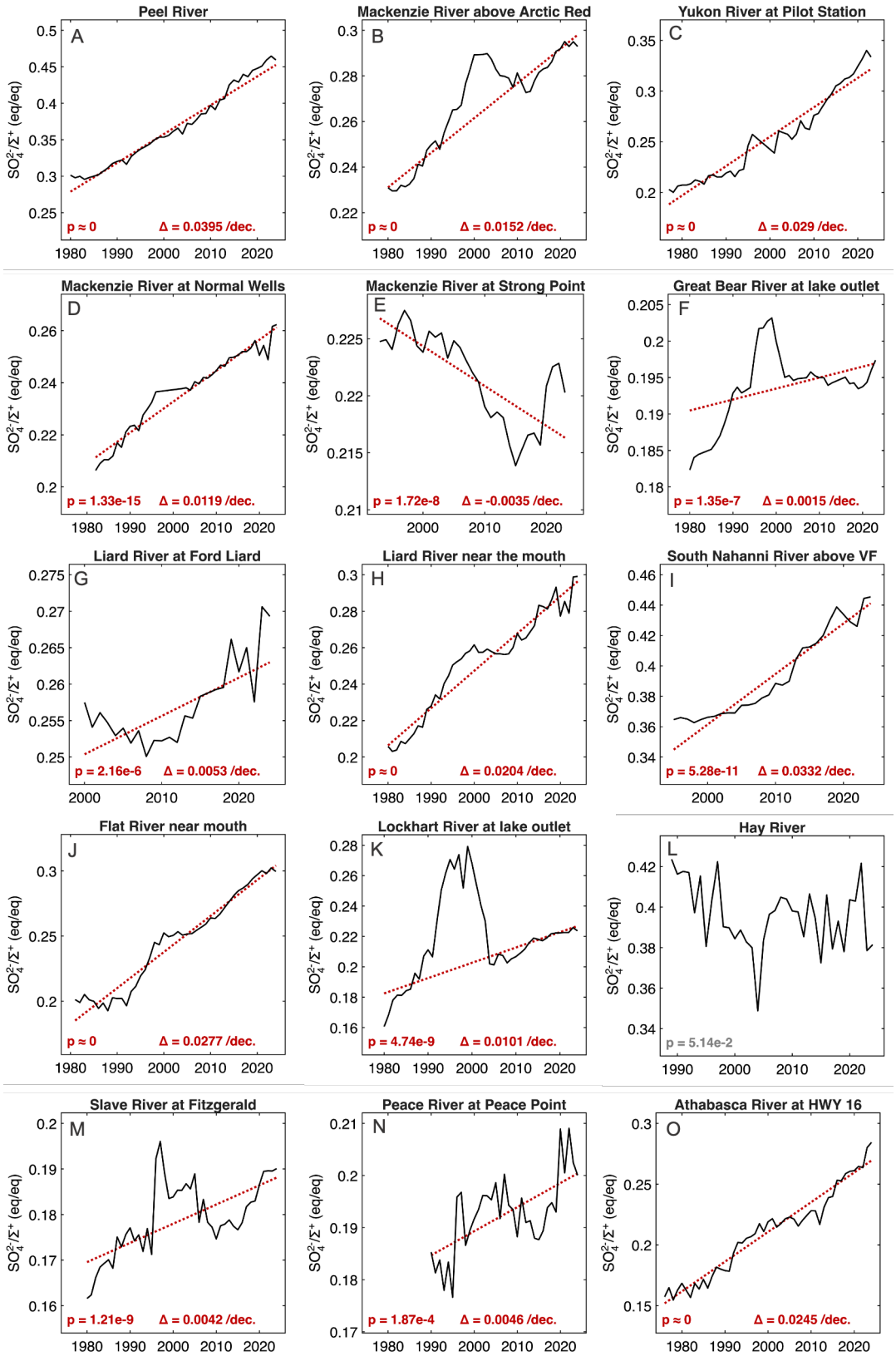


Fig. S27: Annual SO_4^{2-}/Σ^+ flux ratio for each site with Theil-Sen trends plotted when significant ($p < 0.05$).

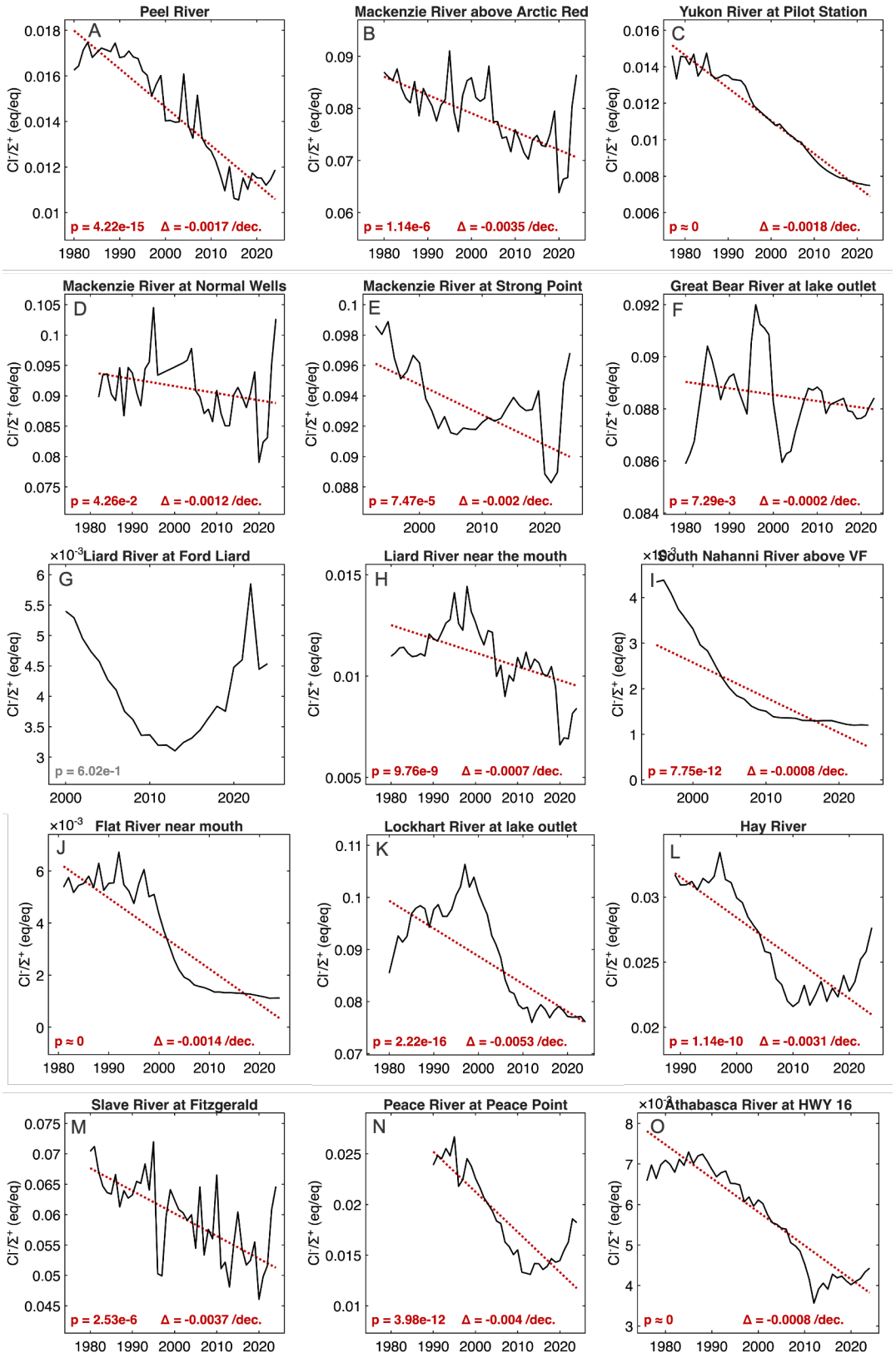


Fig. S28: Annual Cl^-/Σ^+ flux ratio for each site with Theil-Sen trends plotted when significant ($p < 0.05$).

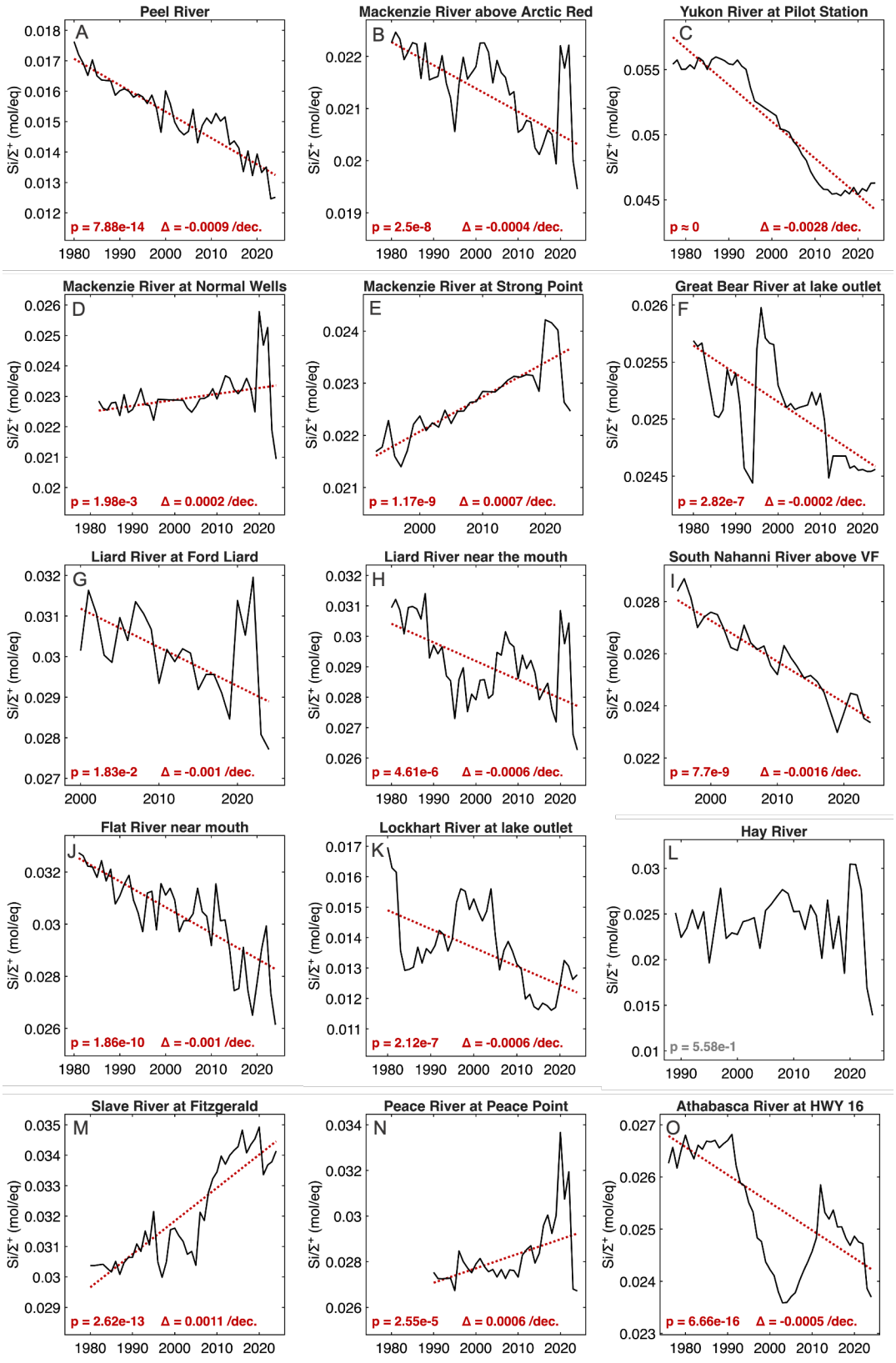


Fig. S29: Annual Si/Σ^+ flux ratio for each site with Theil-Sen trends plotted when significant ($p < 0.05$).

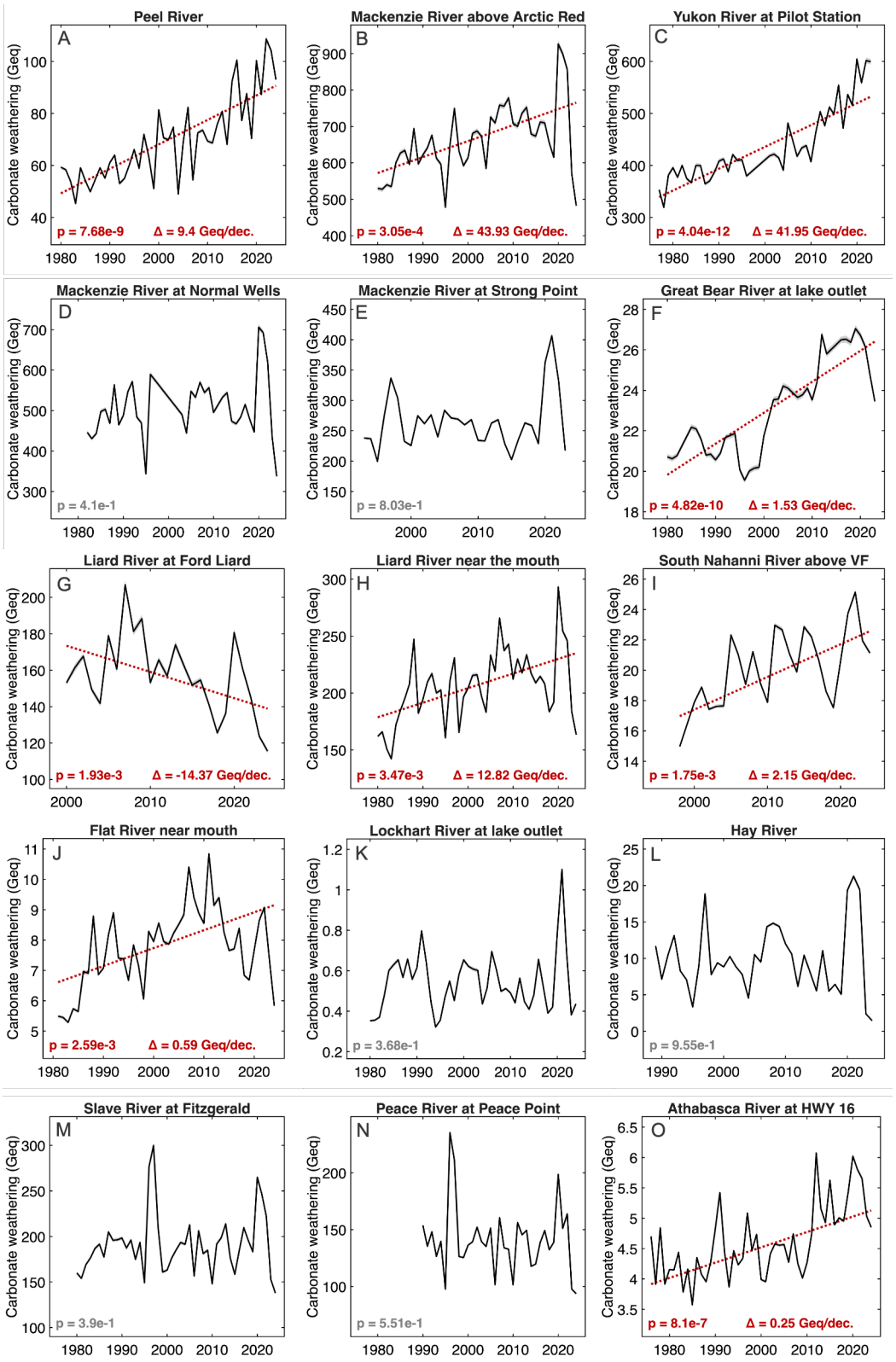


Fig. S30: Annual carbonate weathering flux for each site with Theil-Sen trends plotted when significant ($p < 0.05$). Shading indicates the 5^{th}-95^{th} and 25^{th}-75^{th} percentiles of calculated values. Results are for an inversion with silicate $Si/\Sigma^{\pm} = 0.5 \pm 0.25$.

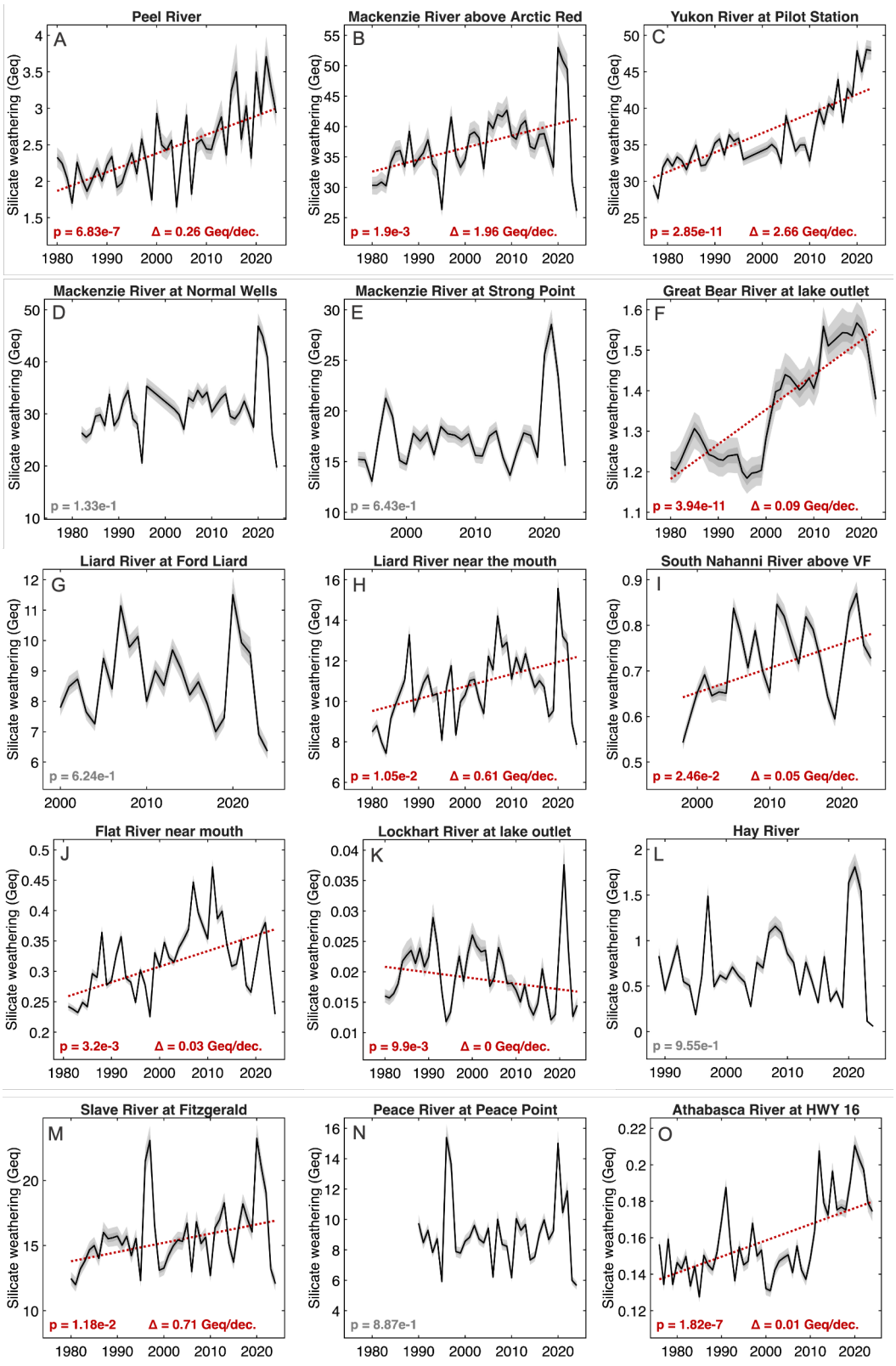


Fig. S31: Annual silicate weathering flux for each site with Theil-Sen trends plotted when significant ($p < 0.05$). Shading indicates the 5th-95th and 25th-75th percentiles of calculated values. Results are for an inversion with silicate $Si/\Sigma^{\pm} = 0.5 \pm 0.25$.

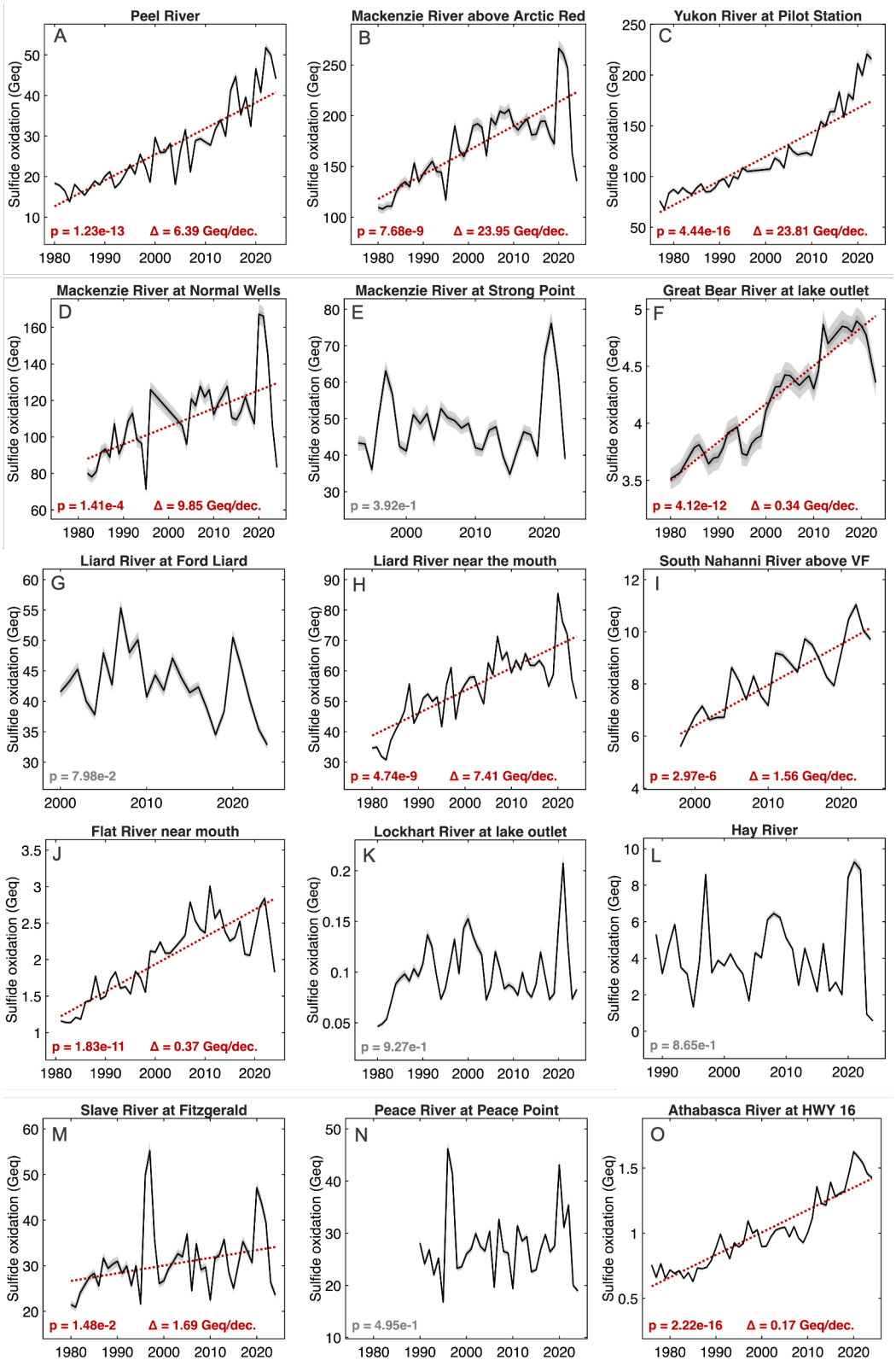


Fig. S32: Annual sulfide oxidation flux for each site with Theil-Sen trends plotted when significant ($p < 0.05$). Shading indicates the 5th-95th and 25th-75th percentiles of calculated values. Results are for an inversion with silicate $Si/\Sigma^{\pm} = 0.5 \pm 0.25$.

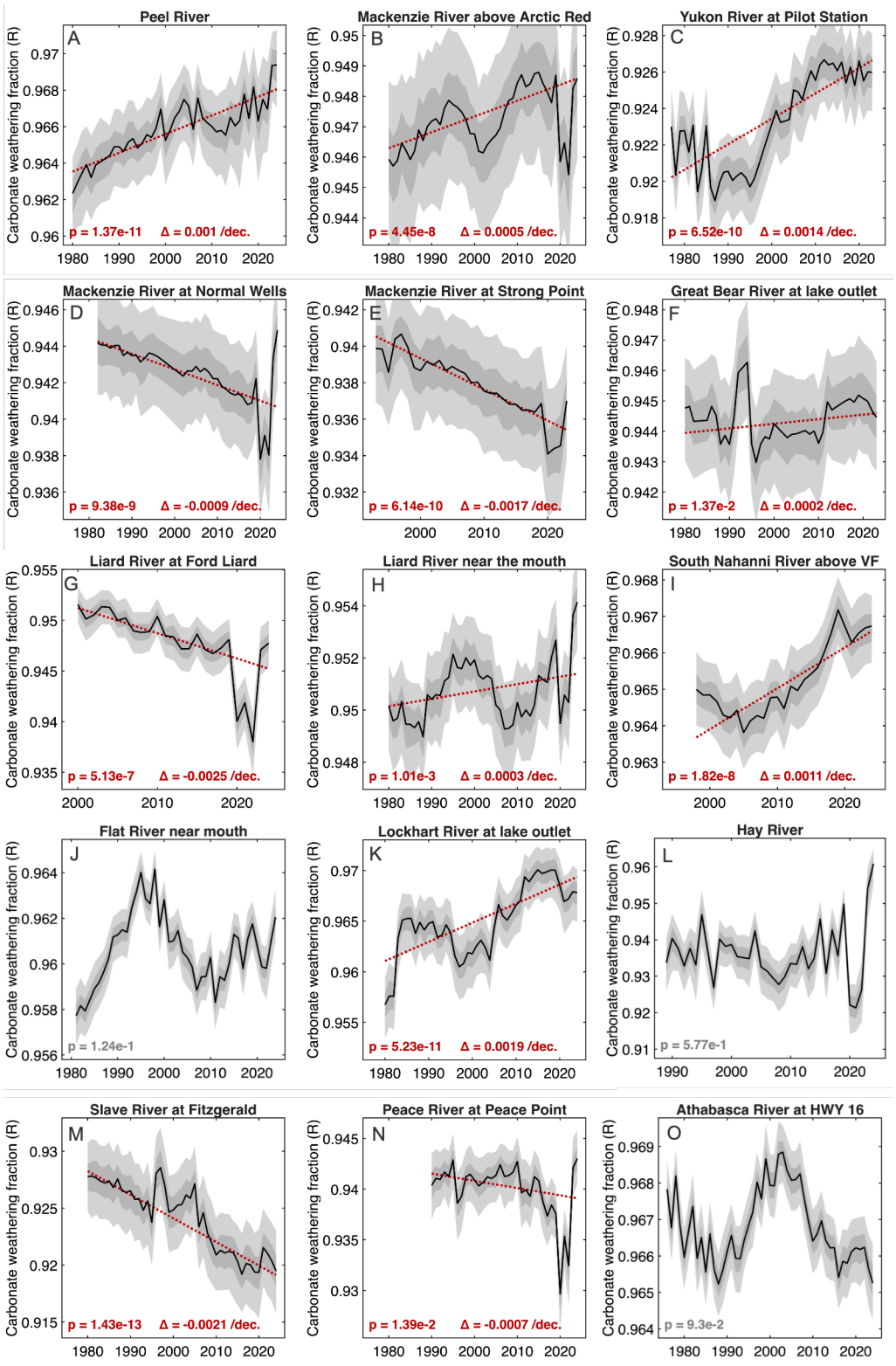


Fig. S33: Carbonate and silicate weathering alkalinity from carbonate weathering (R) for each site with Theil-Sen trends plotted when significant ($p < 0.05$). Shading indicates the 5th-95th and 25th-75th percentiles of calculated values. Note that this R is distinct from weathering vector magnitude. Results are for an inversion with silicate $Si/\Sigma^{\pm} = 0.5 \pm 0.25$.

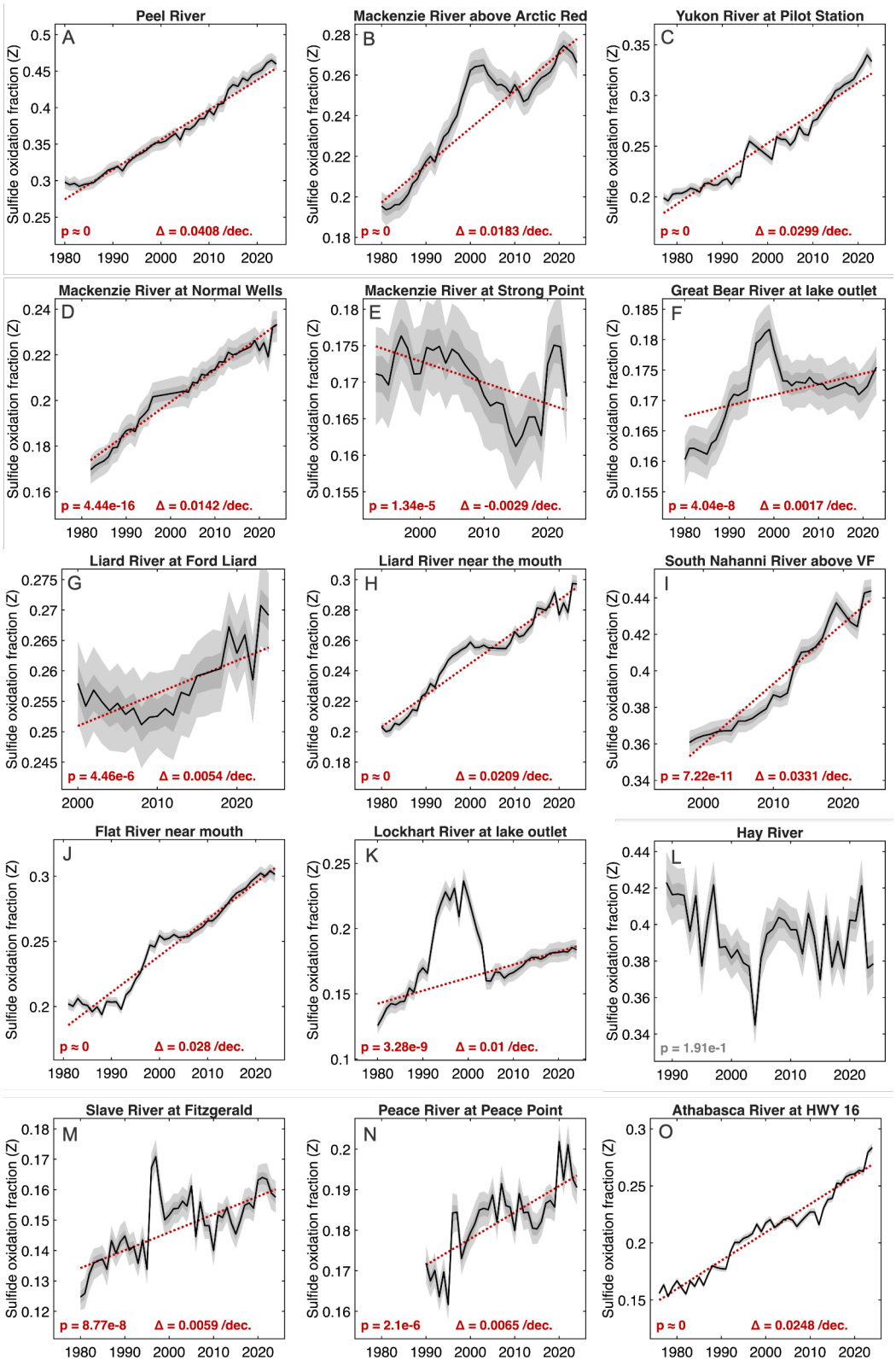


Fig. S34: Carbonate and silicate weathering alkalinity offset by sulfide oxidation (Z) for each site with Theil-Sen trends plotted when significant ($p < 0.05$). Shading indicates the 5th-95th and 25th-75th percentiles of calculated values. Results are for an inversion with silicate $Si/\Sigma^{\pm} = 0.5 \pm 0.25$.

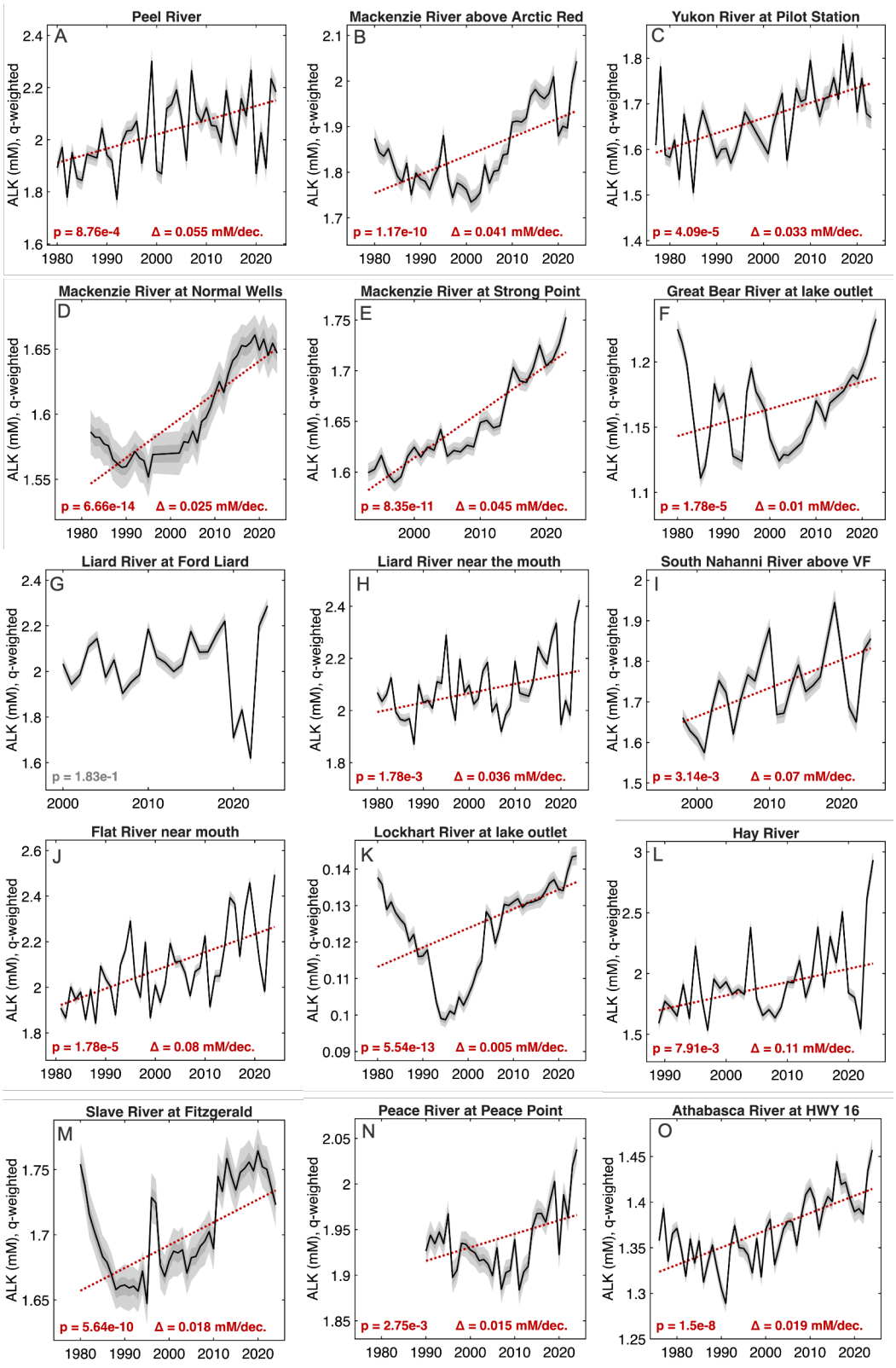


Fig. S35: Annual discharge-weighted Δ(ALK) with Theil-Sen trends plotted when significant ($p < 0.05$). Shading indicates the 5th-95th and 25th-75th percentiles of calculated values. Results are for an inversion with silicate $Si/\Sigma^{\pm} = 0.5 \pm 0.25$.

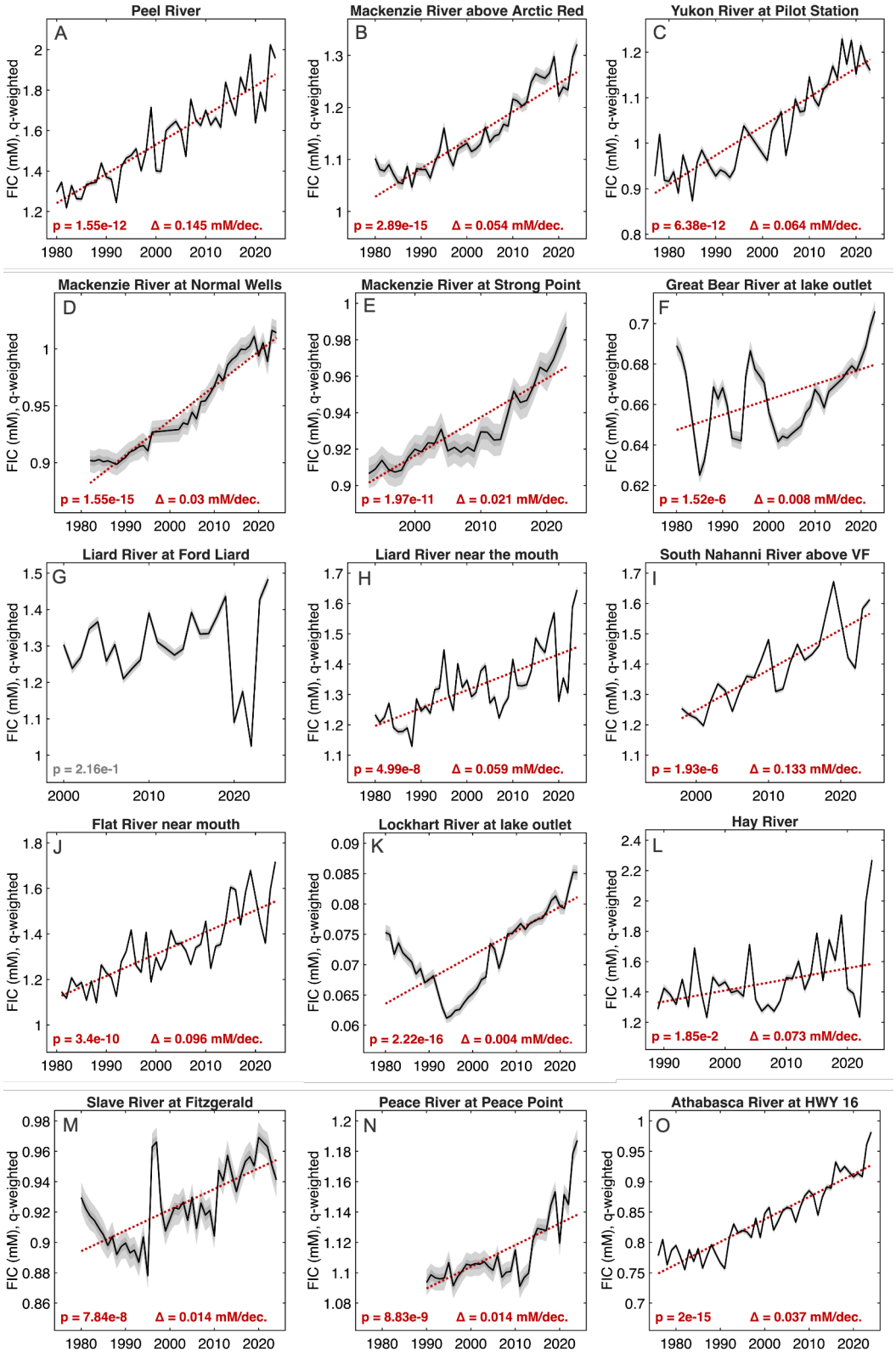


Fig. S36: Annual discharge-weighted Δ(FIC) for each site with Theil-Sen trends plotted when significant ($p < 0.05$). Shading indicates the 5th-95th and 25th-75th percentiles of calculated values. Results are for an inversion with silicate $Si/\Sigma^{\pm} = 0.5 \pm 0.25$.

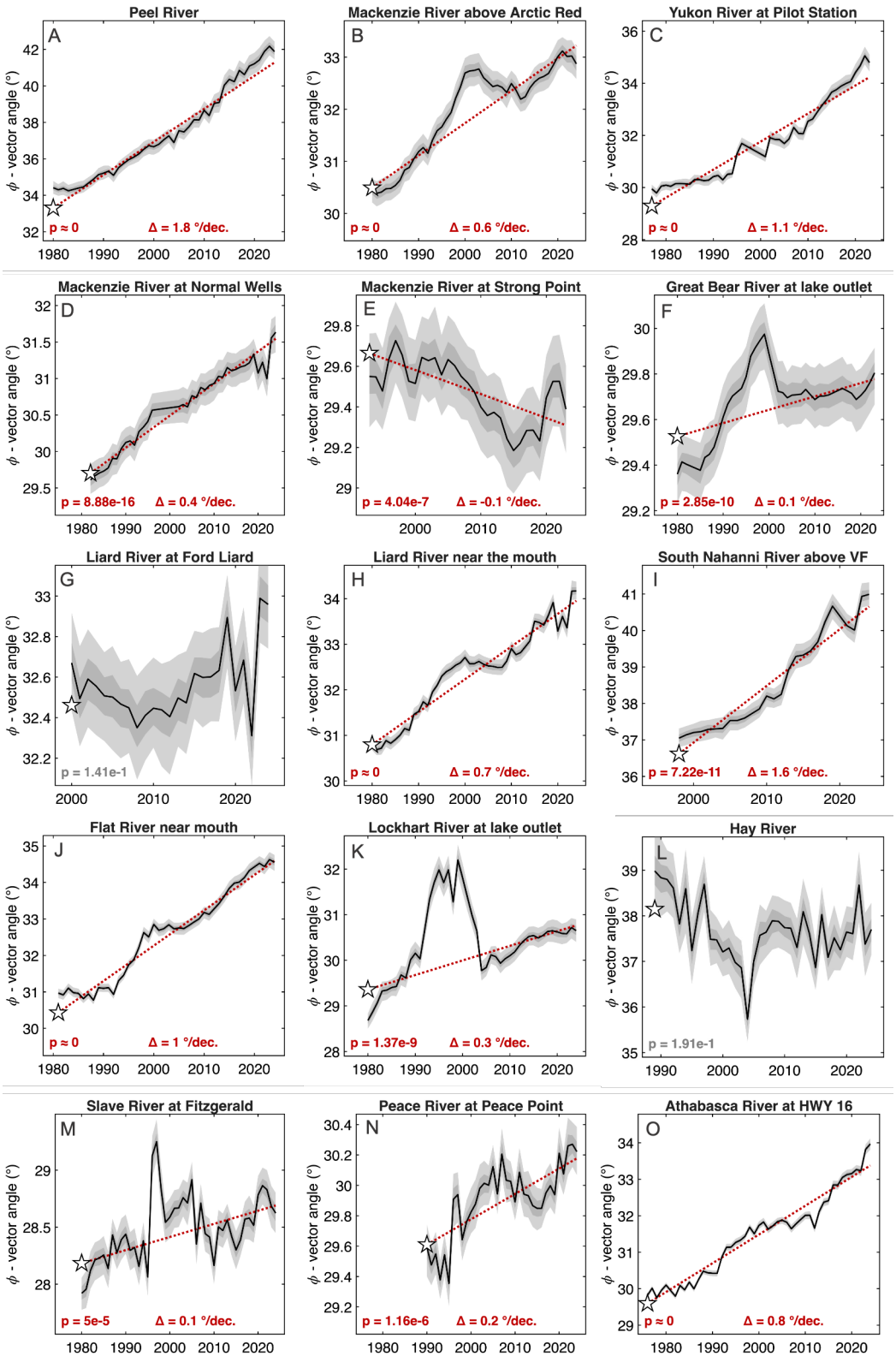


Fig. S37: Annual ϕ with Theil-Sen trends plotted when significant ($p < 0.05$). Plotted star indicates the reference state and shading indicates the 5th-95th and 25th-75th percentiles of calculated values. Results are for an inversion with silicate $Si/\Sigma^{\pm} = 0.5 \pm 0.25$.

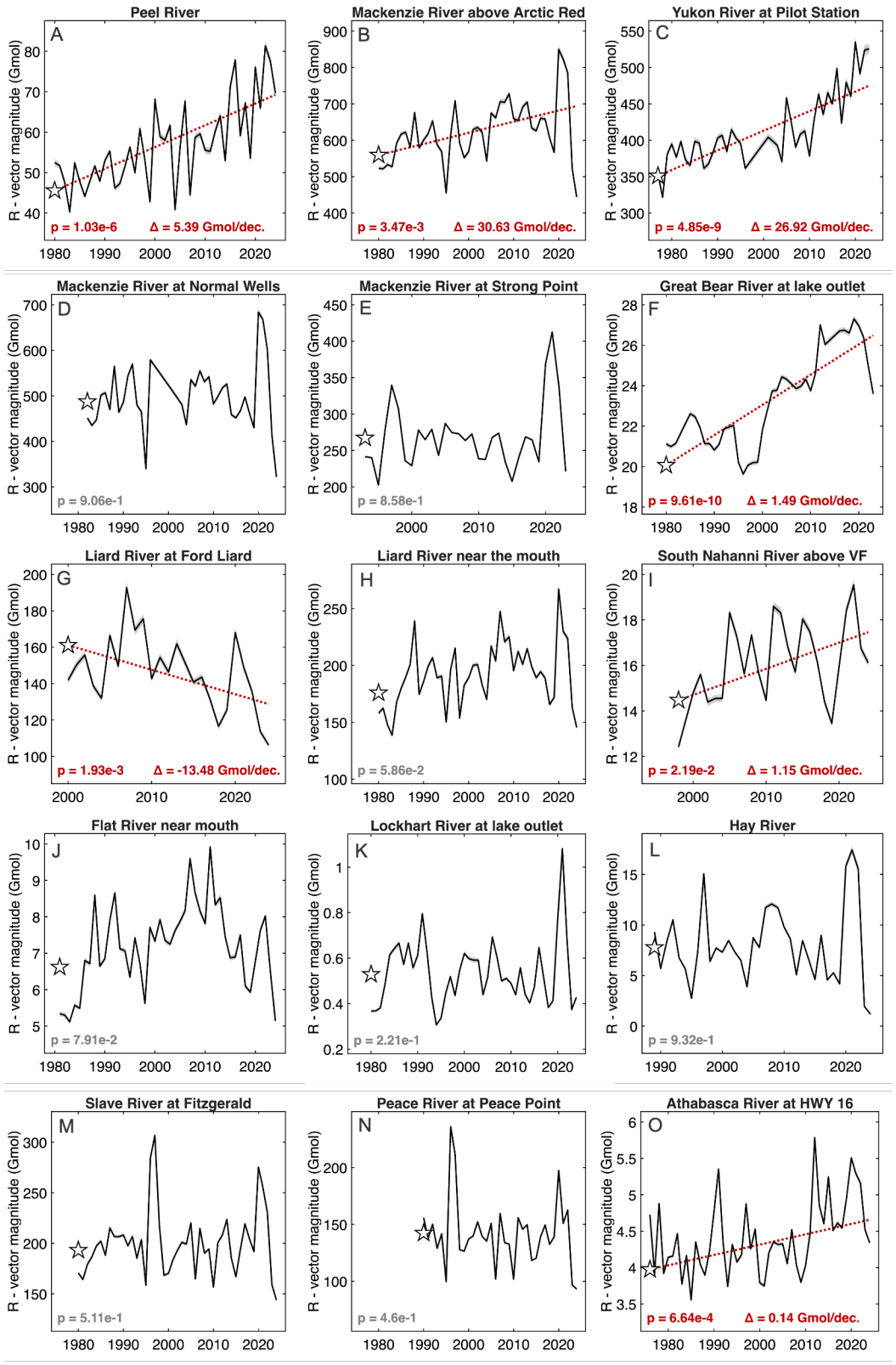


Fig. S38: Annual R with Theil-Sen trends plotted when significant ($p < 0.05$). Plotted star indicates the reference state and shading indicates the 5^{th}-95^{th} and 25^{th}-75^{th} percentiles of calculated values. Results are for an inversion with silicate $Si/\Sigma^{\pm} = 0.5 \pm 0.25$.

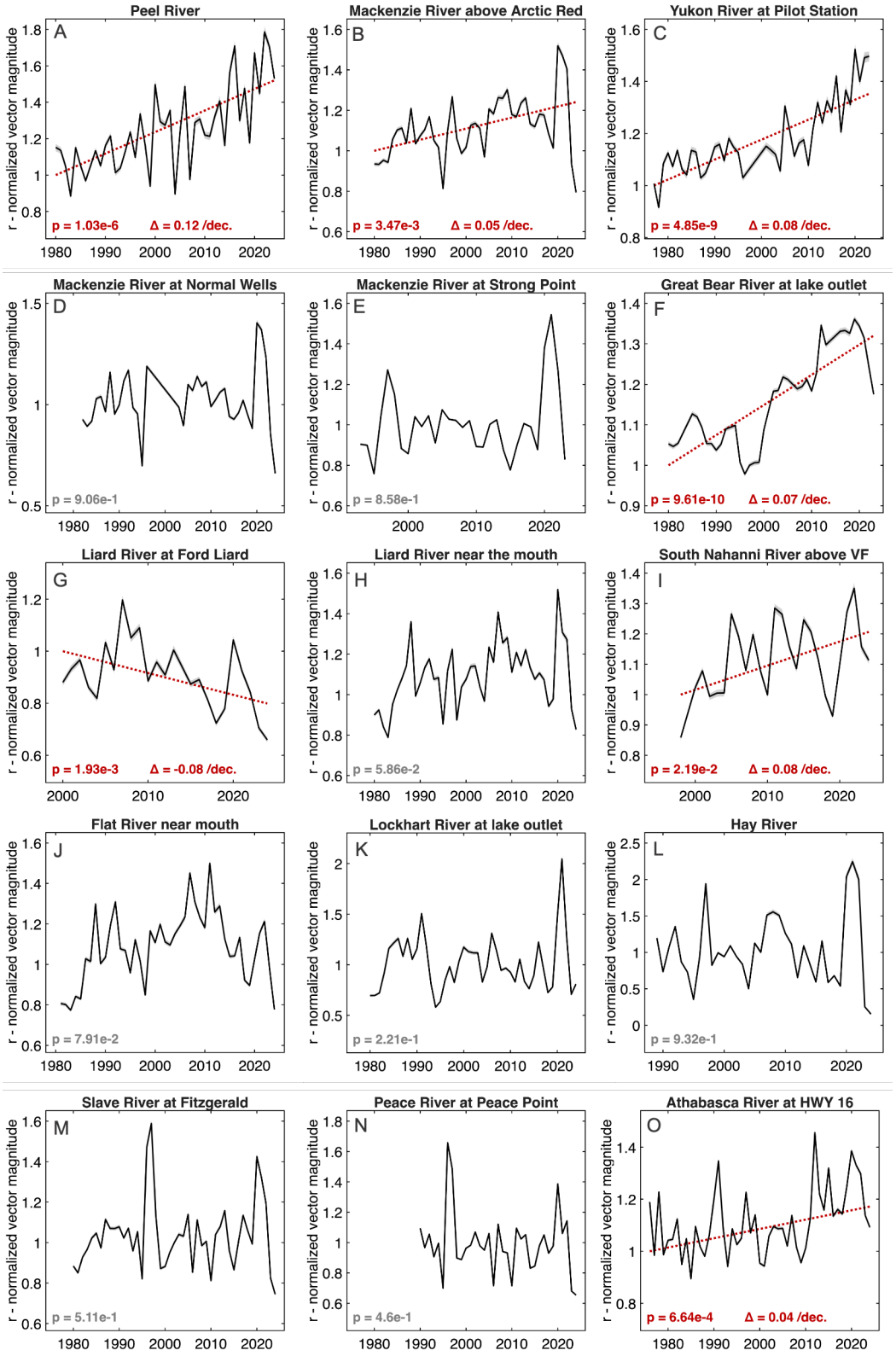


Fig. S39: Annual r with Theil-Sen trends plotted when significant ($p < 0.05$). Shading indicates the 5th-95th and 25th-75th percentiles of calculated values. Results are for an inversion with silicate $Si/\Sigma^{\pm} = 0.5 \pm 0.25$.

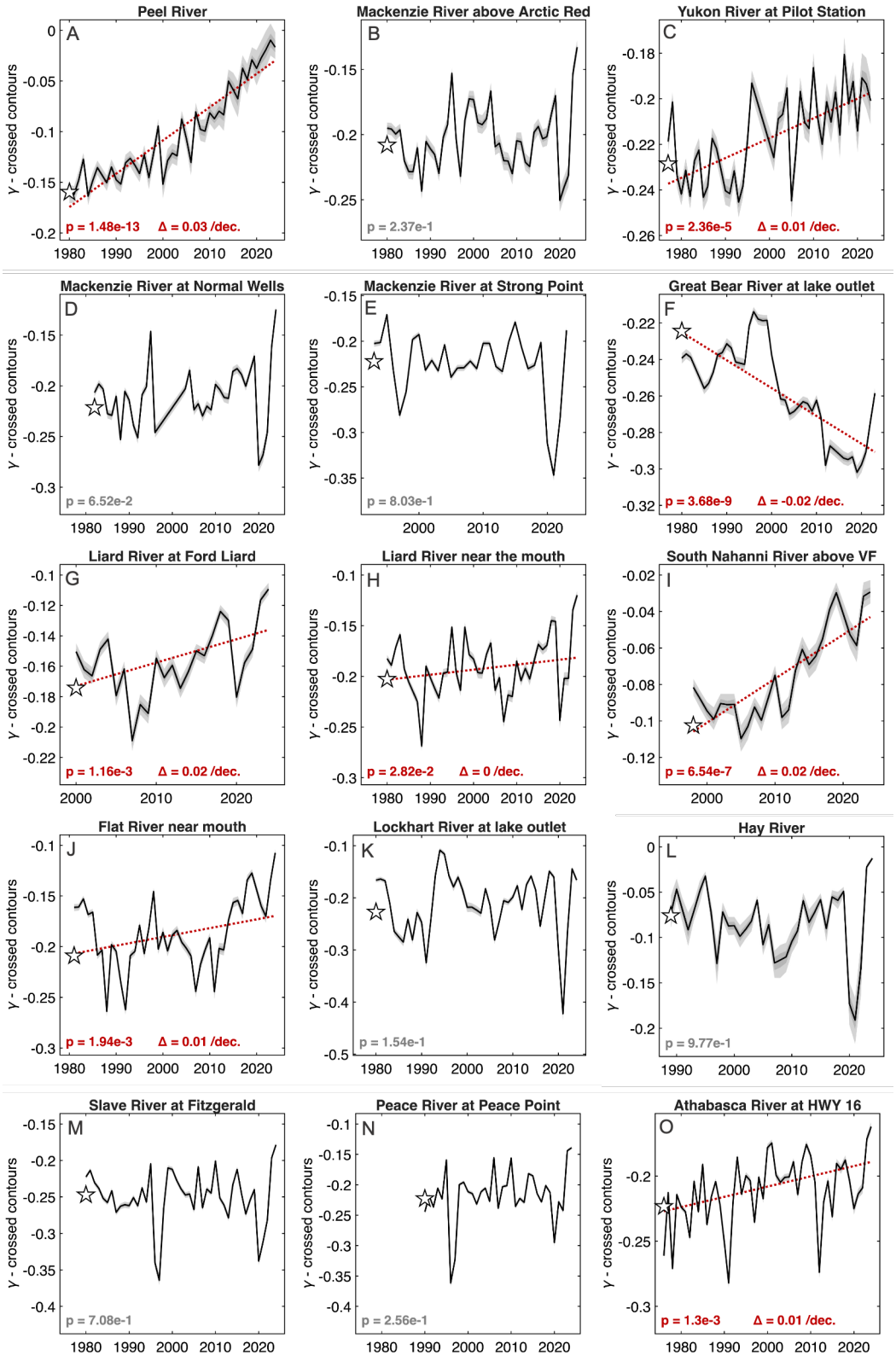


Fig. S40: Annual γ with Theil-Sen trends plotted when significant ($p < 0.05$). Plotted star indicates the reference state and shading indicates the 5th-95th and 25th-75th percentiles of calculated values. Results are for an inversion with silicate $Si/\Sigma^{\pm} = 0.5 \pm 0.25$.

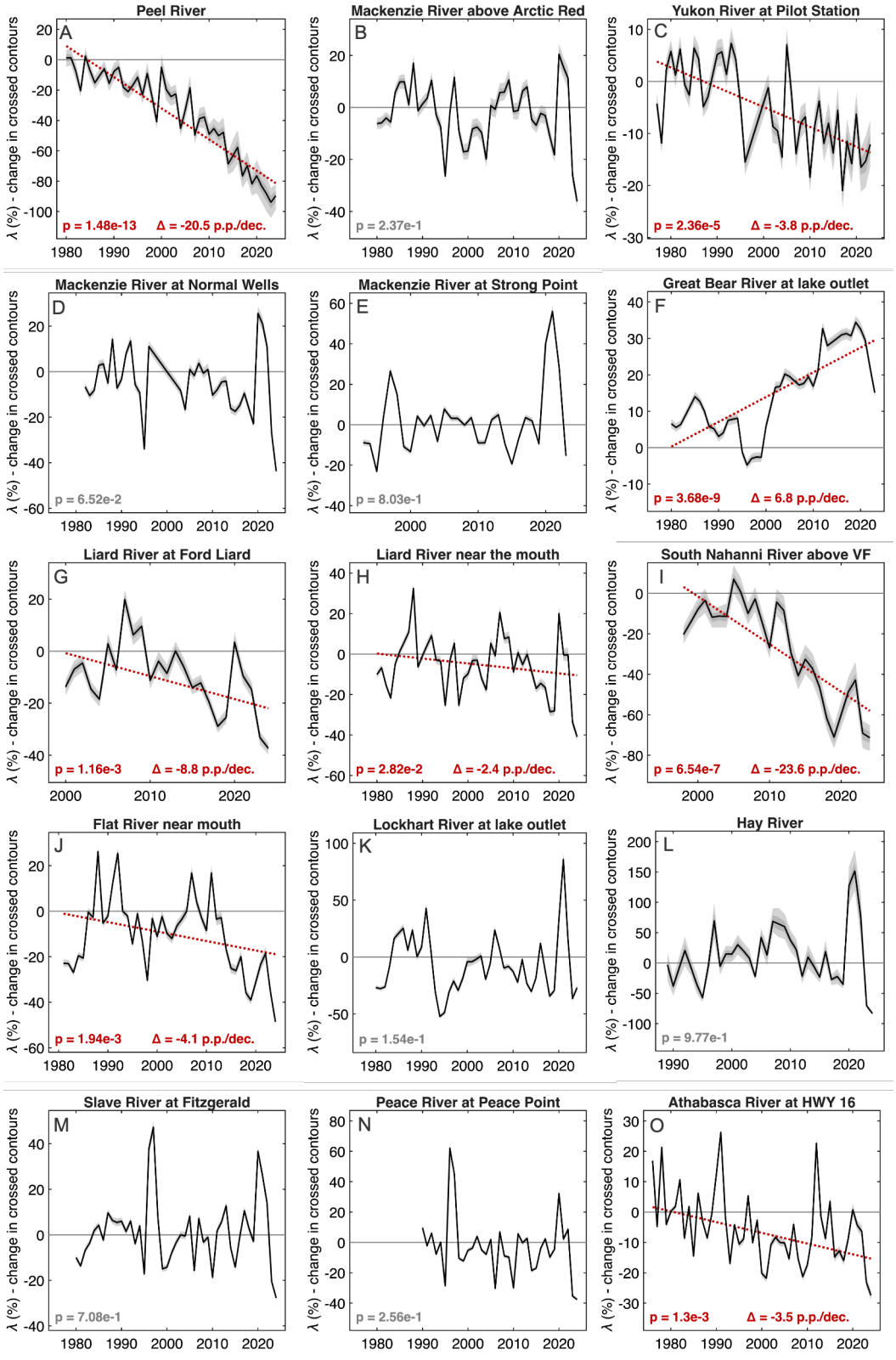


Fig. S41: Annual λ with Theil-Sen trends plotted when significant ($p < 0.05$). Shading indicates the 5th-95th and 25th-75th percentiles of calculated values. Results are for an inversion with silicate $Si/\Sigma^{\pm} = 0.5 \pm 0.25$.

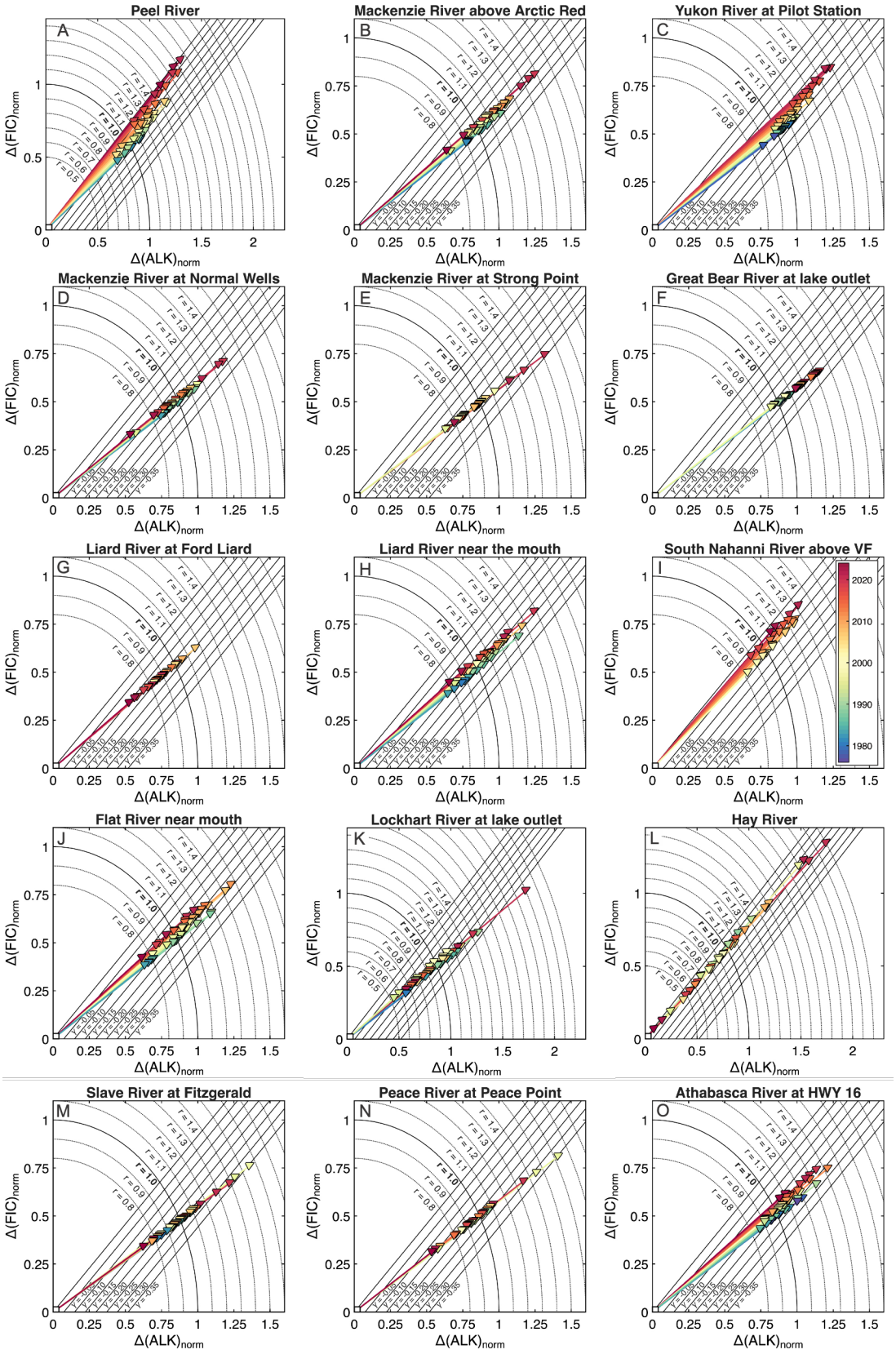


Fig. S42: Annual weathering vectors with labelled contours for γ and r. Results are for an inversion with silicate $Si/\Sigma^{\pm} = 0.5 \pm 0.25$.

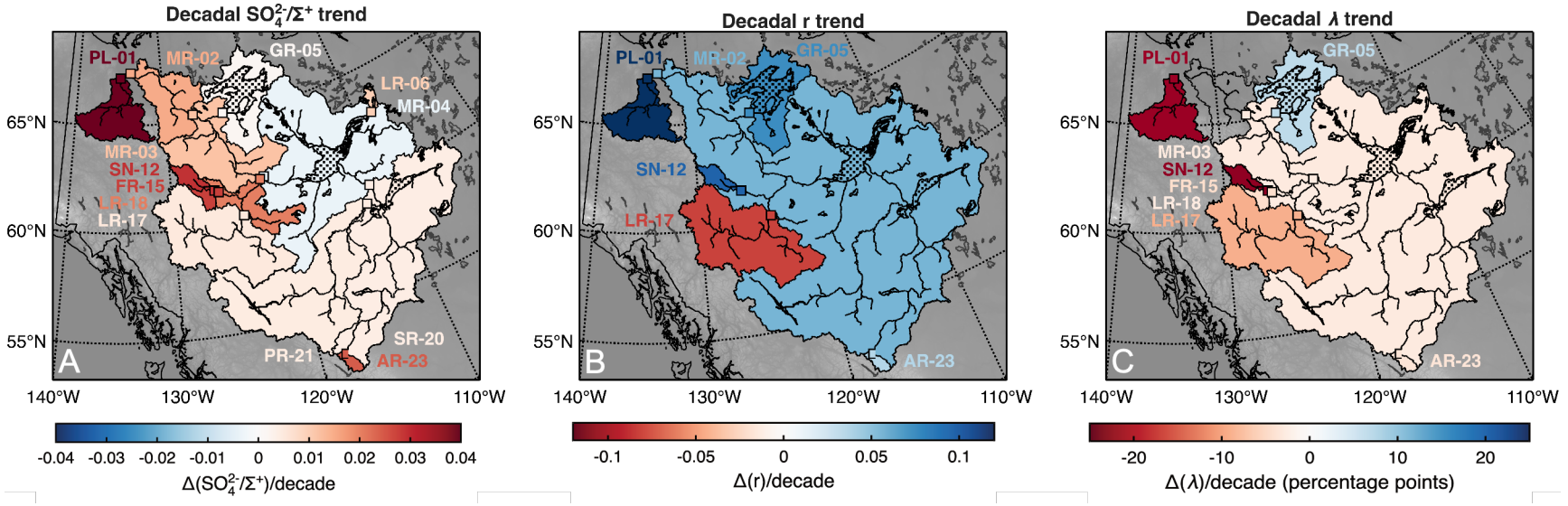


Fig. S43: Significant trends in Mackenzie River subcatchments ($p < 0.05$) for inversion results where the silicate end-member has $Si/\Sigma^{\pm} = 1.0 \pm 0.5$. Unlike Fig. 8, the Mackenzie River at Norman Wells (MR-03) is now found to have experienced significant change in λ.